

University of Wollongong - Research Online

Thesis Collection

Title: An inverse model of ultrasonic echolocation

Author: Janos Tsakiris

Year: 2005

Repository DOI:

Copyright Warning

You may print or download ONE copy of this document for the purpose of your own research or study. The University does not authorise you to copy, communicate or otherwise make available electronically to any other person any copyright material contained on this site.

You are reminded of the following: This work is copyright. Apart from any use permitted under the Copyright Act 1968, no part of this work may be reproduced by any process, nor may any other exclusive right be exercised, without the permission of the author. Copyright owners are entitled to take legal action against persons who infringe their copyright. A reproduction of material that is protected by copyright may be a copyright infringement. A court may impose penalties and award damages in relation to offences and infringements relating to copyright material.

Higher penalties may apply, and higher damages may be awarded, for offences and infringements involving the conversion of material into digital or electronic form.

Unless otherwise indicated, the views expressed in this thesis are those of the author and do not necessarily represent the views of the University of Wollongong.

Research Online is the open access repository for the University of Wollongong. For further information contact the UOW Library: research-pubs@uow.edu.au

University of Wollongong Thesis Collections

University of Wollongong Thesis Collection

University of Wollongong

Year 2005

An inverse model of ultrasonic echolocation

Janos Tsakiris
University of Wollongong

Tsakiris, Janos, An inverse model of ultrasonic echolocation, PhD thesis, School of Information Technology and Computer Science, University of Wollongong, 2005.
<http://ro.uow.edu.au/theses/291>

This paper is posted at Research Online.
<http://ro.uow.edu.au/theses/291>

NOTE

This online version of the thesis may have different page formatting and pagination from the paper copy held in the University of Wollongong Library.

UNIVERSITY OF WOLLONGONG

COPYRIGHT WARNING

You may print or download ONE copy of this document for the purpose of your own research or study. The University does not authorise you to copy, communicate or otherwise make available electronically to any other person any copyright material contained on this site. You are reminded of the following:

Copyright owners are entitled to take legal action against persons who infringe their copyright. A reproduction of material that is protected by copyright may be a copyright infringement. A court may impose penalties and award damages in relation to offences and infringements relating to copyright material. Higher penalties may apply, and higher damages may be awarded, for offences and infringements involving the conversion of material into digital or electronic form.

AN INVERSE MODEL OF ULTRASONIC ECHOLOCATION

A thesis submitted in fulfilment of the requirements
for the award of the degree

DOCTOR OF PHILOSOPHY

from

UNIVERSITY OF WOLLONGONG

by

Janos Tsakiris

B. Sc. (Hons), University of Adelaide

School of Information Technology and Computer Science

2005

Certification

I, Janos Tsakiris, declare that this thesis, submitted in fulfilment of the requirements for the award of the degree of Doctor of Philosophy, in the School of Information Technology and Computer Science, University of Wollongong, is wholly my own work unless otherwise referenced or acknowledged. The document has not been submitted for qualification to any other academic institution.

Janos Tsakiris

May 30th, 2005

Abstract

Object recognition systems based on ultrasonic sensing have significant drawbacks in generality, resolution and speed. The objective of our research was the development of more efficient technique(s) for ultrasonic based object recognition through the investigation of models of acoustic backscatter, with particular emphasis on the work of Albert Freedman. The “image pulse” model developed by Freedman calculates the echoes generated from convex objects in an underwater environment after insonification with a narrowband transient signal. The primary prediction of this model is that echoes are generated at those points along a scattering body where there are step discontinuities in the derivatives, with respect to range, of the solid angle subtended at the transducer by the scatterer, the amplitudes of the echoes being a linear combination of the magnitudes of said discontinuities.

We extended this model for use in an air environment using non-coincident transmitters and receivers and conducted experiments to measure the amplitudes of the echoes from a range of radially symmetric convex objects, at distances up to 1.4m, after insonification with a Polaroid transducer. These amplitudes were compared to those predicted by the model, with the results for the cones highlighting the limitations of the theory at modelling the echoes from the geometrical shadow boundaries of objects. The results for the spherical objects were significantly better however, with an average error of less than 5%, suggesting that the model should be reasonably accurate at calculating the echoes from convex objects with smoothly varying surfaces.

The extended forward model was then inverted to produce an inverse model that would calculate the geometrical parameters of a radially symmetric scattering body from an analysis of the echoes received after insonification of these bodies with ultrasonic pulses at two discrete frequencies. A quantitative verification of this inverse model with various scattering bodies proved elusive, with a low correlation between experiment and theory, due to matrix instability and difficulties in obtaining data of sufficient accuracy. However, qualitative trends in the data indicate that the model is essentially correct, though very sensitive to measurement precision and media characteristics, and there is good reason to believe that further work under more

controlled laboratory conditions and/or a different medium would verify the model's validity quantitatively.

Finally, the inverse model was tested to see whether it could find a practical application despite its quantitative limitations. In many industries, quality control involves distinguishing between those items that are physically damaged and those that are not, a task that the inverse model may be able to address. Using glass bulbs as the test subjects, some with simulated physical damage and some without, we tested the ability of the inverse model to distinguish between these two classes of objects. In all cases, the model clearly separated the items with simulated damage from those without.

The inverse model should be of interest to workers in the field of industrial quality control because of its potential to lead to the development of real-time inspection systems for production lines that could perform with a higher efficiency than the visual inspection procedures currently being employed.

Table of Contents

List of Figures and Tables	viii
Publications from this Thesis	x
Acknowledgements	xi
1. Introduction	1-1
1.1 Autonomous Robotics – An Overview	1-1
1.2 Acoustic Sensing	1-4
1.3 Modelling Acoustic Propagation	1-5
1.4 Research Outline	1-6
1-5 Summary of Results	1-8
2. Freedman’s Forward Model	2-1
2.1 Background	2-1
2.2 Derivation of Freedman’s Model	2-2
2.2.1 Basic Assumptions	2-2
2.2.2 Definitions	2-4
2.2.3 Kirchoff’s Approximation	2-6
2.2.4 Solid Angle	2-7
2.2.5 Extension from a strip of width dr to a Solid Object	2-8
2.3 Physical Interpretation of Freedman’s Model	2-12
2.3.1 Interpretation of the Components of the Equation	2-12
2.3.2 Example: The Sphere	2-14
2.4 Feasibility of Freedman’s Model	2-17
3. Extensions to Freedman’s Model	3-1
3.1 Signal Attenuation Due to Air	3-1
3.2 Breakdown of the $\mathbf{r}_m^{-2} \approx \mathbf{r}_g^{-2}$ assumption	3-3
3.3 Polar Directivity of the Transducer	3-4
3.4 Directivity of the Receiver	3-6

3.5 Non-coincident Transmitter and Receiver	3-8
3.6 Extraction of the Real Component	3-10
4. Experimental Design	4-1
4.1 Noise Minimisation	4-5
A. Environment	4-6
B. Transducer	4-7
C. Chirp Capture Card	4-9
4.2 Echo Analysis	4-10
5. Results and Analysis	5-1
5.1 Experimental Results	5-2
A. Spheres	5-2
B. Regular Cones	5-4
C. Truncated Cones	5-7
5.2 Analysis	5-9
5.3 Conclusions	5-16
6. Development of the Inverse Model	6-1
6.1 Time Independent Inverse Model	6-1
6.2 Time Dependent Inverse Model	6-10
6.3 Mathematical Validity of the Inversion	6-13
6.4 Visualising the Scattering Object	6-14
7. Geometric Analysis of Scattering Bodies	7-1
7.1 Exponentially Shaped Scatterer	7-1
7.2 Paraboloid A	7-8
7.3 Spheroid-Paraboloid	7-12
7.4 Paraboloid B	7-18
7.5 Ellipsoid	7-22
7.6 Fourth Order Shaped Object	7-27

8. Experimental Design, Results and Analysis	8-1
8.1 Experimental Results	8-3
A. Determining $K(f)$	8-3
B. Selecting an appropriate time index t	8-5
C. Results	8-10
D. Fitting a sinusoidal function to the echo data	8-18
8.2 Error Analysis	8-23
8.3 Practical Application of the Inverse Model	8-32
 9. Conclusions	 9-1
9.1 Contributions of this thesis	9-1
9.2 Future Directions	9-3
 A. Appendix	 A-1
A.1 Bibliography	A-1
A.2 Glossary of Terms	A-3
A.3 Derivation of Equation 6.3	A-5
A.4 Data for selected figures.	A-8
A.5 Mathematica™ Code Segments	A-11
A. Noise Subtraction and Interpolation Example	A-11
B. Inverse Model Example (Original Method)	A-14
C. Inverse Model Example (Revised Method)	A-18
A.6 “An Analysis of Freedman’s ‘image pulse’ model in air”	A-25

List of Figures and Tables

FIG. 2.1. Directivity pattern of a 1.9 cm radius transducer at 50kHz	2-8
FIG. 2.2. Echoes from a sphere as predicted by Freedman's model	2-15
FIG. 3.1. Maximum amplitude of the echo versus separation of the microphone from the centre of the transducer	3-8
FIG. 3.2. Alignment of the scatterer to ensure equal path lengths for the transmitted and reflected waves	3-9
FIG. 4.1. Experimental set-up used for chirp transmission and echo reception	4-2
FIG. 4.2. Echo from the large truncated cone at a range of 800mm for a non-coincident transmitter and receiver	4-3
FIG. 4.3. Echo from the large truncated cone at a range of 800mm for a coincident transmitter and receiver	4-3
FIG. 4.4. Echoes from medium truncated cone at a range of 600mm for a non-coincident transmitter and receiver	4-4
FIG. 4.5. Variation in measured amplitude with time of the echo from a target	4-8
FIG. 5.1. Measured and predicted amplitudes of echoes from spheres of diameter d when the transmitter and receiver aren't coincident	5-3
FIG. 5.2. Measured and predicted amplitudes of echoes from spheres of diameter d when the transmitter and receiver are coincident	5-4
FIG. 5.3. Measured and predicted amplitudes of echoes from the bases of regular cones of base diameter d when the transmitter and receiver aren't coincident	5-6
FIG. 5.4. Measured and predicted amplitudes of echoes from the bases of regular cones of base diameter d when the transmitter and receiver are coincident	5-7
FIG. 5.5. Measured and predicted amplitudes of echoes from the faces of truncated cones of truncated face diameter d when the transmitter and receiver aren't coincident	5-8
FIG. 5.6. Measured and predicted amplitudes of echoes from the faces of truncated cones of truncated face diameter d when the transmitter and receiver are coincident	5-9
FIG. 7.1. Representation of an aluminium object with the geometry governed by Eq. (7.1)	7-3
FIG. 7.2. Plot of cross-sectional area (square cm) with respect to range (cm) for the object in Fig. 7.1	7-3
FIG. 7.3. Derivative of the cross-sectional area with respect to range (cm) of the object in Fig. 7.1	7-4
FIG. 7.4. 2 nd order derivative of cross-sectional area with respect to range (cm) of object in Fig. 7.1	7-5
FIG. 7.5. Representation of an aluminium object with the geometry governed by Eq. (7.9)	7-9
FIG. 7.6. Plot of cross-sectional area (square cm) with respect to range (cm) for the object in Fig. 7.5	7-10
FIG. 7.7. Representation of an aluminium object with the geometry governed by Eq. (7.16)	7-13
FIG. 7.8. Plot of cross-sectional area (square cm) with respect to range (cm) for the object in Fig. 7.7	7-14
FIG. 7.9. Derivative of the cross-sectional area with respect to range (cm) of the object in Fig. 7.7	7-15
FIG. 7.10. Representation of an aluminium object with the geometry governed by Eq. (7.26)	7-19
FIG. 7.11. Plot of cross-sectional area (square cm) with respect to range (cm) for object in Fig. 7.10	7-20
FIG. 7.12. Representation of the aluminium object with the geometry governed by Eq. (7.33)	7-23
FIG. 7.13. Plot of cross-sectional area (square cm) with respect to range (cm) for object in Fig. 7.12	7-24
FIG. 7.14. Derivative of cross-sectional area (square cm) with respect to range for object in Fig. 7.12	7-25
FIG. 7.15. Representation of an aluminium object with the geometry governed by Eq. (7.41)	7-28
FIG. 7.16. Plot of cross-sectional area (square cm) with respect to range (cm) for object in Fig. 7.15	7-29
FIG. 7.17. Derivative of cross-sectional area (square cm) with respect to range for object in Fig. 7.15	7-30
FIG. 7.18. 2 nd order derivative of cross-sectional area with respect to range (cm) for object in Fig. 7.15	7-31
FIG. 8.1. Variation of the ratio function with angle across 10 wavelengths	8-8
FIG. 8.2. Variation of the ratio function with angle across a single wavelength	8-9
FIG. 8.3. Comparison of Calculated (broken line) with Predicted (solid line) values for $D(1)$	8-11
FIG. 8.4. Comparison of Calculated (broken line) with $-1 \times$ Predicted (solid line) values for $D(1)$	8-12
FIG. 8.5. Comparison of Calculated (broken line) with $-(1/3) \times$ Predicted (solid line) values for $D(1)$	8-12
FIG. 8.6. Comparison of Calculated (broken line) with the Predicted (solid line) values for $D(2)$	8-14
FIG. 8.7. Comparison of Calculated (broken line) with the $(1/10^4) \times$ Predicted (solid) values for $D(2)$	8-14

FIG. 8.8. 40kHz echo from the spheroid-paraboloid	8-16
FIG. 8.9. 60kHz echo from the spheroid-paraboloid	8-16
FIG. 8.10. Original echo data (top) and it's subset taken from the monotonic region (below)	8-18
FIG. 8.11. Superposition of Eq. (8.14) over the sampled data (solid points) to verify correlation	8-19
FIG. 8.12. Condition number of the inverse matrix as a function of time	8-21
FIG. 8.13. Comparison of Calculated (broken line) with Predicted (solid line) values for $D(I)$	8-22
FIG. 8.14. Comparison of Calculated (broken line) with Predicted (solid line) values for $D(I)$ with associated errors	8-27
FIG. 8.15. Comparison of Calculated (broken line, which is too close to zero to be visible) with Predicted (solid line) values for $D(2)$ with associated error bars	8-27
FIG. 8.16. 100W Clear Bayonet Cap Light Bulb with a 1cm square area mound of Blu-Tak™ attached to the glass	8-33
FIG. 8.17. Comparison of the Predicted relative values for $D(I)$ for both the untouched bulbs (top) and the modified bulbs (bottom)	8-34
Table 7.1. Discontinuities on the exponentially shaped object	7-8
Table 7.2. Discontinuities on the first parabolic object	7-12
Table 7.3. Discontinuities on the spheroid-paraboloid	7-18
Table 7.4. Discontinuities on the second parabolic object	7-22
Table 7.5. Discontinuities on the ellipsoid	7-27
Table 7.6. Discontinuities on the 4 th order object	7-33
Table A.4.1. Data For Fig. 5.1	A-8
Table A.4.2. Data For Fig. 5.2	A-8
Table A.4.3. Data For Fig. 5.3	A-8
Table A.4.4. Data For Fig. 5.4	A-9
Table A.4.5. Data For Fig. 5.5	A-9
Table A.4.6. Data For Fig. 5.6	A-9
Table A.4.7. Data For Fig. 8.3	A-10
Table A.4.7. Data For Fig. 8.6	A-10
Table A.4.7. Data For Fig. 8.13	A-10
Table A.4.7. Data For Fig. 8.17	A-10

Publications from this Thesis

J. Tsakiris and P. J. McKerrow, "A Model of Ultrasonic Echolocation," in Proceedings of the 1996 National Conference of the Australian Acoustical Society (1996).

P. J. McKerrow, D. Crook and J. Tsakiris, "Modelling Ultrasonic Sensing for Mobile Robots," in Proceedings of the Sixth International Symposium on Robotics and Manufacturing (1997), pp. 497-502.

J. Tsakiris and P. J. McKerrow, "An Analysis of Freedman's 'image pulse' model in air," J. Acoust. Soc. Am. **108** (4), 1602-1613 (2000).*

J. Tsakiris and P. J. McKerrow, "An Inversion of Freedman's 'image pulse' model in air" (Submitted to J. Acoust. Soc. Am., June 2005).

* Copy in Appendix A.6.

Acknowledgements

I may not have reached this point in my studies were it not for the support and inspiration offered to me by numerous individuals in the years since I first decided to pursue research as a career. I cannot honour all those who supported me prior to the commencement of my PhD research but I will make mention of Messrs. Wallace and Ronaldo, my high school physics teachers. They inspired me with their enthusiasm for the subject and without them I doubt I would have seriously considered research as a viable career path.

During my time as a doctoral student there were several who provided invaluable support to me. First and foremost, I must thank my supervisor Associate Professor Phillip McKerrow. Phil's experience, guidance and positive outlook were of paramount importance in ensuring that I was able to remain on track during those times when research related problems appeared to be overwhelming.

I'd also like to thank Janice Sendt, the Acoustics Studies Manager at Thales Underwater Systems Pty. Ltd., for her assistance during the early stages of my research in aiding my understanding of the fundamentals of acoustic theory. Her extensive experience in this area proved most helpful. Also Ben Stanley, a colleague who provided invaluable technical support and developed the software that was critical in the capture and analysis of the data central to my research. Ben, having a background in physics, also provided valuable insights into matters related to acoustics, for which I'm grateful.

Dave Crook, whose research preceded mine, provided assistance early on and Dr Neil Harper, working on a project not dissimilar to my own, was also of assistance. I'd also like to thank Dr Danny Ratner who's philosophical musings on the state of the world were a welcome diversion and my close friends Hery Ralainony and Dina Pierro who's assistance during difficult times will never be forgotten. Last, but by no means least, I'd like to thank my parents and brother for providing moral and financial support over the years. Without their encouragement and guidance, I may not have managed.

1 Introduction

1.1 Autonomous Robotics – An Overview

Robotics is a broad field which offers tantalising possibilities for the automation of the simplest tasks currently undertaken by human labour (in the short term) and the liberation of society from all manual labour (in the long term). It is a discipline which is a conglomerate of several older, more established disciplines such as electrical and electronic engineering and mechanical engineering as well as newer ones such as artificial intelligence and acoustic & visual sensing. However, it is a field which has lived up to only some of the promises that it has offered since its inception at the start of the computer age after the Second World War. Progress in these individual fields within robotics have not advanced at the same rate across the board, with developments on the engineering side far outstripping that of artificial intelligence and sensing.

Advances in mechanical and electrical engineering have seen the construction of robots with exceptional mechanical precision and flexibility. The most clichéd, but still arguably the best, example of these, are those that can be seen in the automotive industry where automation plays a large role on the assembly line for car manufacturing. With pinpoint precision and flexibility that extends to multiple degrees of freedom, these machines are very successful in doing the job that they were designed to do - a simple, repetitive mechanical task with no variation in its motion from one cycle to the next. But the field of robotics offers the possibilities of much more than the production of automatons that are deaf, dumb and blind. In order for robots to increase their scope of applicability, they have to be able to sense their surroundings, plan how to get around these surroundings and then move about these surroundings. Such robots are known as *autonomous mobile* robots.

As stated above, the areas that are the bottleneck for progress in robotics are those of artificial intelligence and sensing. Artificial intelligence covers many aspects of robot behaviour including path planning, obstacle avoidance and object interaction. The methods employed to teach robots how to do these range from conventional programming methodologies to neural networks to genetic programming. As we've already pointed out, progress in this field has been slower than expected. This is undeniably due to the fact that in many respects we still don't quite know what it is that constitutes 'intelligence'. Even psychologists are in disagreement on this issue as evidenced by the many different variants of the Intelligence Quotient (IQ) test. A more comprehensive understanding of how the human mind (and thus intelligence) works may be required before we can reasonably be expected to develop software that mimics the decision making process on a level approaching the human brain. This however, is probably some time off.

What is of interest to us however, is the other major stumbling block of robotics, the ability of a robot to sense its environment. There are two major threads of research in this area, those of vision based sensing and those of acoustic based sensing. Vision based sensing has dominated in recent years and involves analysing two dimensional images of an environment, captured from a camera, to identify and attempt to classify objects within the field of view. This is usually achieved by identifying the edges of objects in an image and building up a best-estimate wire-frame outline of these objects. From this, the types of objects, their sizes and locations can hopefully be identified.

Alternately, partial success has been achieved with neural networks that are trained to identify particular objects in an image, although difficulty in identifying exactly *what* it is that a neural network has learnt to identify has caused confusion in some instances. One famous example of this involved an attempt to train a neural

network to identify tanks hidden behind a forested area. Although it appeared at first that the neural network was successful at distinguishing photos of those trees that concealed tanks from those that did not, it later turned out that the photos of tanks concealed behind trees were taken on a cloudy day whilst those of trees without tanks behind them were photographed on a sunny day. In fact, the neural network had simply learned to distinguish sunny days from cloudy ones. This story, although perhaps apocryphal, nevertheless nicely illustrates the problem inherent in neural network based recognition systems, we cannot always be sure *what* the network is learning.

The other major thread of research for mobile robot sensing employs acoustics, or more specifically ultrasonics. Ultrasonic sensing has been used for mobile robot navigation for some time, an early example being that of the Meldog guide dog robot¹ which used an array of acoustic sensors to localise the position of objects/obstacles. We feel that vision based approaches can be supplemented with data obtained by acoustic sensing methods. Acoustic sensing has far more potential than is commonly perceived. From the world of nature we know that bats can successfully navigate caves in pitch black darkness using acoustic echoes alone² with a degree of accuracy far surpassing anything robot navigation is currently capable of. However, for far too long acoustic sensing for robots has been associated with simple range finding or methods derived from it, such as the arc model (to be discussed shortly) and as such has been often overlooked in favour of vision. However, it's been shown that high precision sensing with acoustic pulses is possible. Kuc and Kleeman³ have demonstrated that objects up to 8m away from a transmitter/receiver configuration and separated by as little as 10mm can be localised and classified with a precision of 1mm and 0.1 degrees in still air. Thus acoustics offer the possibility of highly innovative techniques for sensing the

environment and identifying specific objects within it and it is from this viewpoint that we approach the topic.

1.2 Acoustic Sensing

The application of acoustics for sensing is almost always done in the ultrasonic region of the acoustic spectrum. This is because the higher the frequencies used, the more accurately range can be determined. The audible range is up to 20kHz and ultrasonic frequencies are anything beyond that, although in practice most ultrasonic work tends to take place above 40 kHz. A practical benefit of using ultrasonic pulses is by virtue of them being beyond the range of human hearing, they are quiet and thus suitable for use in urbane environments. Far more accurate range readings can be obtained at these frequencies as well, but they require a detailed analysis of the reflected wave, rather than a simple time of flight measurement.

The most popular approaches for ultrasonic object recognition for mobile robotics are based on the arc model and impulse response model, although other approaches abound⁴. The arc model⁴ involves taking several range readings to an object as the sensor moves past it. One draws arcs with a locus at the position of the transmitter and a radius of curvature equal to the range reading obtained. By drawing lines that intersect the tangents to these arcs we obtain an estimate of the object shape. The problem with this method is the poor resolution of the images that result, as even the simplest objects such as a circular bin will end up reconstructed as a polygon. The other drawback is the speed, or lack thereof, of the method since the sensor has to move around the object before any image can be built up.

An alternative is the impulse response method⁵ whereby a broadband ultrasonic pulse irradiates the object and fourier analysis is performed on the received echo. Since different objects will interfere with different frequencies by different amounts, the fourier components of the returned echo will differ from one object to another. These echoes can then be used to form a database of recognizable signals. Although a much faster method than the former, it can obviously only be used for object recognition with those objects that it has previously encountered and hence has limited applicability.

1.3 Modelling Acoustic Propagation

The aim of the research presented here is to take a step back and examine the physics of scattering in an attempt to find the basic geometric characteristics that produce the echoes observed. This will lead to the development of an inverse model that will enable the determination of the physical characteristics of the object from a measurement of its echo. It is envisaged that such a model could enable the development of sensing systems that would complement current ultrasonic sensing technology.

Models for calculating the returned echo from an object of arbitrary shape irradiated by an acoustic wave fall roughly into two categories which we could call analytical models and numerical models. The former essentially provide us with an equation that relates the geometry of the object to the echo received. Because the echo and the geometry are linked via the equation, it has the potential to be mathematically inverted which would enable us to determine object geometry from the echo. In practice though, for many of these models a wide range of objects can give rise to the same echo, the many-solutions problem, making inversion useless.

Numerical models, on the other hand, approach the problem by calculating the entire ultrasonic wave field at small discrete time steps from the moment of initial transmission until the moment the echo is received. Because the entire field is recalculated for each time interval, accurate echoes can be calculated for even relatively complex shapes. The drawback of these models is the time required for the echo calculation, from minutes to hours with current processing speeds, but more importantly they lack inversion potential because mathematical inversion only provides the wave-field for the previous time step and at this stage you've already encountered the many-solutions problem. Consequently, analytical models offered the best hope for our objectives, the model of choice being that developed of A. Freedman in the late 1950's.

Thus to sum up, our aim is to develop, test and apply models of acoustic scattering off rigid bodies to the task of object identification.

1.4 Research Outline

In Chapter 2, we will examine the foundations of Albert Freedman's model of acoustic echo formation as well as providing an abridged derivation of the model itself, with a focus on the basic assumptions that are central to the model. We'll also provide a qualitative or physical understanding of the processes modelled by his equation and look at how feasible it will be to use it as a model for our needs.

The chapter that follows will outline the extensions that we've made to Freedman's model, specifically the impact of signal attenuation due to air, the breakdown of one of the assumptions of range equivalency (see later), the polar directivity of the transmitter, the directivity of the receiver and the non-coincidence of

the transmitter and receiver. This will provide us with an extended model that, theoretically, should have validity in air with non-ideal transmitters and receivers.

In Chapter 4 we examine the experimental setup and the methodology that we employed to test this extended model as well as discussing the various noise sources that must be contended with, including environmental noise, interference from the transducer itself and electronic noise in the chirp capture card.

In Chapter 5 we look at the results of the experiments conducted using simple geometric shapes to test the validity of this model. In particular, we examine the results for spheres, cones and truncated cones at various ranges to see how well the correlation between measured echoes and the predicted ones turns out to be. We also provide an analysis of why certain shapes perform better in these tests than others.

Chapter 6 sees the development of an inverse model of acoustic backscatter. In particular, we examine two possible approaches to the development of this model – one based on a time *dependent* method and another based on a time *independent* method. As both approaches have potential strengths and weakness, we examine why we eventually reject one of these models in favour of the other. Finally, we examine how an inverse model can be theoretically be used to visualise a scattering body.

In Chapter 7 we choose a set of geometric objects that conform to the limitations of the inverse model, including an exponentially shaped body, paraboloids, an ellipsoid and others, and examine their geometries. In particular, an analysis of the location, order and amplitude of any discontinuities along their irradiated surface.

Chapter 8 sees an examination of experiments conducted with the objects analysed in Chapter 7 to test the validity of the inverse model, as well as an analysis of the level of uncertainty in the predictions of the inverse model. Also discussed is the

ability of the inverse model to be put to practical use, using as an example experiments conducted to simulate the identification of manufacturing faults in glass bulbs.

In the final chapter we summarise our results and examine areas where the implementation of the inverse model may be beneficial, both within and without the field of autonomous mobile robotics.

1.5 Summary of Results

Freedman's forward model, when extended to air, is fairly accurate in calculating the echoes from the closest points on spheres, with a higher than 96% correlation between experiment and theory under certain conditions, and may potentially be used for modelling the echoes from the faces of truncated cones, provided these faces have a small enough cross-sectional area. Its limitations are that it cannot be used for modelling the echoes from the geometrical shadow boundaries of objects, such as the base of a cone.

The inverse model that was developed from the forward model could not be quantitatively verified due to the coupling of an ill conditioned matrix with data of insufficient accuracy that produced estimates with little correlation with the measured data. However there is good reason to believe that future work under exceptionally rigorous laboratory conditions, or within a different medium (eg. water), may verify the model's quantitative validity.

Finally, despite the quantitative limitations of the model, it's general qualitative agreement between theory and measurement was shown to have a potential practical application by being able to distinguish between those glass bulbs that had a simulated defect and those that did not.

2 Freedman's Forward Model

2.1 Background

By the mid-twentieth century, the bulk of acoustic and electromagnetic scattering theory had confined itself to the continuous wave case, which, whilst an easier system to model mathematically, is limited in the scope of its applicability. These models⁶ all follow the basic tenet that by assuming an incident wave of infinite length (ie. continuous wave) incident upon a rigid body, field solutions can be found which satisfy the boundary conditions at the transmitter and the scatterer. From this, the steady state field amplitude (ie. amplitude as time approaches infinity) of the scattered wave can be determined at any point outside the scatterer. However, this will invariably be a sinusoidal wave of constant amplitude, which provides no information on the shape of the scattering body. A more comprehensive examination of the wave mechanics would need to take into account transient waves, or pulses, but precious little work had been done in the way of transient wave theory by this stage.

Albert Freedman, aware of this deficiency in our theoretical understanding and spurred on by advances in the fields of EM wave propagation, oil prospecting, non-destructive testing and medical imaging, developed a theory of acoustic echo formation that focussed on transient waves. He went on to test this model using a range of geometrically simple objects suspended in water and his theoretical and experiment work formed the basis for his 1961 doctoral dissertation "The Formation of Acoustic Echoes in Fluids"⁷. As we will show, although Freedman's model didn't stand up too well to experimental verification, due mostly to deficiencies in his experiment apparatus rather than the theory, it provides an intuitive understanding of the mechanisms behind

the scattering of acoustic transients. It's for this reason that it was chosen as a suitable theory to base an inverse model upon.

2.2 Derivation of Freedman's Model

2.2.1 Basic Assumptions

The original derivation of the model is a rather long and detailed affair and it would be redundant to reproduce it here. However, it's advantageous to provide an abridged derivation here because at several points throughout the derivation, Freedman makes assumptions and approximations that simplify the model to an extent. Whilst these may have seemed justified at the time, our extension of this model required us to re-examine the validity of these assumptions and approximations and so an understanding of how and why they were made is necessary for a thorough understanding of the model.

Firstly, we are concerned only with the scattering of waves off *single* bodies since a multi-body system, with its multiple reflections from different angles, would only serve to complicate the dynamics. Secondly, we'll assume that our system involves a reflector which is static (ie. not in motion). This eliminates the need for the model to compensate for Doppler shift, variable distances and the fluid dynamics of a body in transit through a fluid. Since wave scattering can occur in three ways, (1) scattering from an external surface, (2) scattering from an *internal* surface and (3) resonance phenomena, the model will assume that the first mechanism dominates and (2) & (3) are negligible. The physical assumptions that this translates to are twofold. Firstly, to prevent internal reflections we need to assume that the object is rigid. More generally,

we need to prevent *multiple* reflections, internal reflections being but one example, so a further assumption is made that the object is convex. To prevent resonance phenomena, we assume that the amplitudes of the acoustic waves are too small to cause any motion in the body itself.

Several further assumptions serve to simplify our system. One is that the wavelength used is much smaller than the dimensions and radius of curvature of the scattering body, allowing us to use the Kirchoff approximation, an important approximation to be elaborated upon later. The assumption also serves to reduce the impact of creeping waves and other surface waves, which, if unchecked, would contribute to the echo from the scattering body. Freedman surmised however that the contributions from creeping waves would be negligible and thus would not need to be accounted for in the model. We will show later that this assumption was flawed.

We'll also assume that the scatterer has a smooth surface, thereby ensuring *specular*, as opposed to *diffuse*, reflection, which is necessary to maintain to a coherent wavefront. We'll use the generally accepted Rayleigh criterion of $\lambda/4$, where λ = the wavelength of the acoustic wave, as the upper limit for specular reflection. Thus, any surface features larger than this are deemed to produce diffuse reflection. Another assumption is that the transmitter and receiver are coincident points as opposed to extended objects, an assumption intended to simplify the modelling of the wavefront's transmission and reception. We'll also assume that the voltage at the transducer's terminals is directly proportional to the acoustic pressure at the transducer's faces, an assumption that extends to both the transmitter and receiver. This assumption of a linear relationship is necessary because non-linearities would adversely affect our results. The fluid medium that encompasses the transmitter, receiver and scattering body is assumed to be non-dissipative (ie. doesn't absorb the energy of the acoustic wave) as well as both

homogeneous and isotropic (ie. having the same physical properties at all points and in all directions respectively).

Finally, we'll assume that the scattering body is in the Fraunhofer region (ie. far field) of the transmitter and receiver, since this will allow us to model the reduction in wave intensity with distance using the inverse square law (ie. $Intensity \propto 1/distance^2$). To ensure that the transmitter and receiver are indeed in the far field, the physical extent of the source must be small compared to the distance travelled by the wave, a factor of 3 to 10 generally being considered acceptable⁸. This translates to ensuring that the diameter of the transducer is small compared to the distance to the scatterer *and* that the size of the scatterer is small compared to the distance to the receiver.

2.2.2 Definitions

The assumptions having been made, the terms were defined,

$PF_1(\psi, \phi)$ = Sensitivity of the transmitter (transducer) in direction (ψ, ϕ) , where

P = pressure produced per unit volt at unit distance in direction $\psi = \phi = 0$.

$HF_2(\psi, \phi)$ = Sensitivity of the receiver (microphone) in direction (ψ, ϕ) , where

H = voltage produced per unit pressure at unit distance in direction $\psi = \phi = 0$.

The transmitter and receiver are defined as being at the origin of this polar coordinate system. It's not shown above, but transmitters and receivers also have a directional sensitivity to frequency. This will be taken into account when we add a directivity function to our derived equation in the next chapter.

For a point in the far field, the pressure p at time t_i of the transmitted wave at distance r in the direction (ψ, ϕ) is given by,

$$p = VPF_1(\psi, \phi) \frac{\exp(j[\omega t_i - kr])}{r} \quad (2.1)$$

where, V = voltage applied to the transducer,

ω = angular frequency of the wave ($= 2\pi f$),

t_i = instant of incidence upon the target,

k = wave number ($= 2\pi/\lambda$),

j = imaginary number,

and r = range to the target.

The scattering surface can be defined as $\phi = F_3(r, \psi)$ and thus *at the scatterer*,

$$F_1(\psi, \phi) = F_1(\psi, F_3(r, \psi)) = F_p(r, \psi)$$

$$\& \quad F_2(\psi, \phi) = F_2(\psi, F_3(r, \psi)) = F_H(r, \psi)$$

Hence, the pressure p_i at time t_i of the wave incident upon an element of area ds of the scatterer surface at distance r in the direction (ψ, ϕ) is given by,

$$p_i = VPF_p(r, \psi) \frac{\exp(j[\omega t_i - kr])}{r} \quad (2.2)$$

2.2.3 Kirchhoff's Approximation

At this stage, the Kirchhoff approximation is introduced which makes the assumption that each element ds on the scattering body will scatter incoming radiation over a solid angle of 2π (ie. into half space). At first glance, this may seem to violate the law of angle of incidence equalling angle of reflection. On a qualitative level though, this approximation can be understood by appreciating that ds is of negligible size (ie. a point) and a point reflector is incapable of reflecting incoming radiation in any preferred direction. This assumption having been made, Kirchhoff's approximation goes on to state that the scattering surface is composed of an infinite number of these elemental areas, each of which reflects incoming radiation into half space.

By using the above approximation, as well as its prerequisite that $r \gg \lambda$, and analysing boundary conditions, Freedman extended Eq. (2.2) above into the following form,

$$\Delta p_s = -j \frac{VP}{\lambda} \exp(j[\omega t - 2kr]) \frac{F_p(r, \psi) \cos \varphi}{r^2} ds \quad (2.3)$$

where, Δp_s = pressure at the receiver due to scattering off ds ,

φ = angle of incidence of the incoming radiation at ds .

The equation above only models the contribution from a single element, so the next steps were the inclusion of the contributions from all elements along a strip at a distance r to $r + dr$, by integrating over the strip at that distance and then the integration of the resulting equation for all r along the length of the scatterer. The linear

relationship between acoustic pressure and receiver voltage was also factored in. The equation he derived was,

$$E = -j \frac{VPH}{\lambda} \exp(j\omega t) \int_0^{\infty} \frac{dW_w(r)}{dr} \exp(-j2kr) dr \quad (2.4)$$

where, E = voltage at the receiver due to the scattered echo from the object.

$W_w(r)$ = *directivity weighted* solid angle subtended at the receiver by all parts of the scattering body within the range r .

2.2.4 Solid Angle

The concept of the solid angle $W(r)$ subtended at the receiver by part of the scatterer is best understood by visualising a plane slicing through the scattering body at range r , the area of intersection of the plane with the scatterer being denoted by $A(r)$. To conceptualise the solid angle in this manner we assume that the scatterer is far from the receiver, so that the locus of equidistant points from the receiver to the intersection at range r can be approximated as a plane rather than a sphere.

Provided this range r is not in the shadow region of the scatterer (ie. a region *out* of the direct line of sight of the transmitter), the solid angle $W(r)$ for a convex object is simply given by,

$$W(r) = \frac{A(r)}{r^2} \quad (2.5)$$

It provides a measure of how much of the space surrounding the transmitter/receiver is occupied by the scattering body at that range, a theoretical total enclosure of the transmitter taking the maximum value of 4π . Eq. (2.4) however, makes mention of the *directivity weighted* solid angle $W_w(r)$. This is an acknowledgment that real world transmitters/receivers are not simply coincident points in space, but have two-dimensional extent and as such cannot emit or receive with the same sensitivity in all directions, the reasons for which will be elaborated upon at a later stage. Fig. 2.1 shows a typical example of the directivity of a plane piston transducer⁸, the characteristic lobe pattern is a by-product of its two-dimensional structure.



FIG. 2.1. Directivity pattern of a 1.9 cm radius transducer at 50kHz.

Thus a weighting is superposed on $W(r)$ to account for the variation in the transmitter and receiver directivities and this is denoted as $W_w(r)$, although we'll show later that treating the transmitter and receiver as plane pistons rather than points eliminates the need to artificially weight the solid angle.

2.2.5 Extension from a strip of width dr to a Solid Object

The next stage of the derivation is the extension of the model to incorporate the contributions from all strips along the scattering body within the irradiated region. We'll define r_1 as the distance from the transmitter to the nearest part of the scattering body

and r_f as the distance to the farthest part of the scatterer *that remains within line of sight of the transmitter*. $W_w(r)$ will remain zero up to a distance of r_1 , as the virtual plane has yet to intersect with the scatterer up to this point and will continue to increase in size until distance r_f , after which it remains at this maximum value for all $r \rightarrow \infty$. If the wavefront encounters a planar region on the scattering body between r_1 and r_f , say r_g , then $W_w(r)$ will have a finite, discontinuous increase in its magnitude at this range. An example of such a scattering body would be a truncated cone, where $W_w(r_g)$ at the truncated front face would be a discontinuous function.

Since we need to be able to integrate over all points that may include discontinuities, we'll need to split up the surface into regions proceeding and regions beyond the discontinuities and add the contributions from these regions separately. Let's assume the surface is continuous (ie. has no discontinuities) from $r=0$ to $r < r_g$ and the solid angle for this section of the scatterer being denoted $W_{wg-}(r)$. Similarly, let's assume continuity over the ranges $r > r_g$ to $r \rightarrow \infty$, the solid angle for this section being denoted $W_{wg+}(r)$. The size of the discontinuity is thus given by,

$$D(W_w, g, 0) = D(W_w, r_g, 0) = W_{wg-}(r) - W_{wg+}(r) \quad (2.6)$$

and the integral in Eq. (2.4) becomes,

$$\begin{aligned} \int_0^{\infty} \frac{dW_w(r)}{dr} \exp(-j2kr) dr &= \lim_{\epsilon \rightarrow 0} \int_0^{r_g - \epsilon} \frac{dW_{wg-}(r)}{dr} \exp(-j2kr) dr + \\ &\lim_{\epsilon \rightarrow 0} \int_{r_g + \epsilon}^{\infty} \frac{dW_{wg+}(r)}{dr} \exp(-j2kr) dr - D(W_w, g, 0) \exp(-j2kr_g) \end{aligned} \quad (2.7)$$

Now, given that $W_w(r)$ remains constant (ie. zero) in the range $0 < r < r_1$, it follows that $\frac{dW_w(r)}{dr} = 0$ in this range also. Similarly, over the range $r_f < r < \infty$, the solid angle remains the same (ie. it's maximum obtained at r_f) and thus $\frac{dW_w(r)}{dr} = 0$ over this range as well. Thus, the limits in the integral of Eq. (2.7) are narrowed,

$$\begin{aligned} \int_0^\infty \frac{dW_w(r)}{dr} \exp(-j2kr) dr &= \lim \varepsilon \rightarrow 0 \int_{r_1}^{r_g - \varepsilon} \frac{dW_{wg-}(r)}{dr} \exp(-j2kr) dr + \\ &\lim \varepsilon \rightarrow 0 \int_{r_g + \varepsilon}^{r_f} \frac{dW_{wg+}(r)}{dr} \exp(-j2kr) dr - D(W_w, g, 0) \exp(-j2kr_g) \end{aligned} \quad (2.8)$$

For a scatterer with multiple solid angle discontinuities in the range $r_1 < r < r_f$, the contributions from each region between the discontinuities can be expressed as,

$$\lim \varepsilon \rightarrow 0 \int_{r_g + \varepsilon}^{r_{g+1} - \varepsilon} \frac{dW_{wg-}(r)}{dr} \exp(-j2kr) dr$$

and by using integration by parts, Freedman was able to express the total contribution of all regions across the scatterer as a discrete summation, where each value of n represents a separate discontinuity,

$$\int_0^\infty \frac{dW_w(r)}{dr} \exp(-j2kr) dr = -\exp(-j2kr) \sum_{n=1}^\infty \frac{dW_w^n(r)}{dr^n} (j2k)^{-n} \quad (2.9)$$

We define the n th order discontinuity in the solid angle as,

$$D(W_w, g, n) = \frac{d^n (W_{wg-}(r) - W_{wg+}(r))}{dr^n} \quad n = 0, 1, 2, 3, \text{ etc...} \quad (2.10)$$

and thus the voltage at the receiver is given by the summation of all contributions from all regions along the scatterer where discontinuities occur,

$$E = \sum_{g=1}^f \sum_{n=x}^{\infty} E(g, n) \quad (2.11)$$

where x = the lowest derivative of $W_w(r)$ for which a discontinuity exists at r_g ,

$$\text{and } E(g, n) = j \frac{VPH}{\lambda} \exp(j[\omega t - 2kr_g]) \frac{D(W_w, g, n)}{(j2k)^n} \quad (2.12)$$

If the scattering body is sufficiently far enough away from the transmitter such that the intensity of the wavefront varies negligibly over the extent of the scatterer, then $W_w(r)$ can be re-written as,

$$W_w(r) = \frac{A_w(r)}{r_m^2} \quad (2.13)$$

where r_m = *mean* range of the discontinuities on the scattering body, given by the midway point between the first and last discontinuities.

We define,

$$D(W_w, g, n) = \frac{D(A_w, g, n)}{r_m^2} \quad (2.14)$$

Thus, the voltage E_g at the receiver due to backscatter off the body from the discontinuity at range r_g is given by,

$$E_g = j \frac{VPH}{\lambda r_m^2} \exp(j\theta) \sum_{n=0}^{\infty} \frac{D(A_w, g, n)}{(j2k)^n} \quad (2.15)$$

where $\theta = \omega t - 2kr$.

This is the final equation in the derivation of Freedman's model. Although Freedman went on to derive equations for special cases, this remains the highest level *general* equation for his model.

2.3 Physical interpretation of Freedman's Model

2.3.1 Interpretation of the Components of the Equation

Providing a physical, or intuitive, interpretation of Freedman's model is best achieved by breaking Eq. (2.15) down into several modules and generalising the role of each. Firstly, at a fixed frequency, the term VPH is a constant of proportionality which represents the dependence of the voltage at the receiver on the product of (a) the voltage applied to the transmitter, (b) the transmissivity of the transmitter and (c) the sensitivity of the receiver. The λ in the denominator indicates that the amplitude of the reflected waves from the scattering body's surface will be smaller at lower frequencies and it's

presence in the equation is a product of the Kirchoff approximation. The r_m^2 in the denominator is a product of the inverse distance law for geometrical spreading loss from a point source being applied *twice*, since we have transmission from the source to the range r_m as well as reflection back to the receiver, again over a range r_m . The exponential term $\exp(j\theta)$ in Eq. (2.15) is the complex form of the solution to the wave equation, which simply models the cyclic sinusoidal variation in wave amplitude over time and distance. The terms within the summation represent, in the case where $n = 0$, the magnitude of the direct backscatter to the receiver and in the case of higher order components (ie. $n > 0$), the magnitude of the diffracted signals transmitted toward the receiver. In air, the contributions from successively higher order terms diminish by orders of magnitude however and so in practice only the first two, or possibly three, terms have any relevance to the echo produced. This is wholly due to the fact that the wave number k for an ultrasonic wave in air is very high, of the order of 10^3 . For other environments where the wave number is lower, for example water at 20°C which has $k = 212$ for a 50kHz wave⁹, the diminishment of the higher terms would be less pronounced.

The specific role that the n th order discontinuity terms $D(A_w, g, n)$ within the summation play in generating echoes in Freedman's model is best illustrated by example. The n th order discontinuity function for a discontinuity at range r_g , can be expressed as follows,

$$D(A_w, g, n) = \frac{d^n A_w}{dr^n}(r_{g-}) - \frac{d^n A_w}{dr^n}(r_{g+}) \quad (2.16)$$

where r_{g-} and r_{g+} represent the ranges infinitesimally prior to and beyond the discontinuity respectively.

At an arbitrary range r_x on a *smoothly varying* section of the scatterer's surface, the n th order derivative of the cross sectional area with respect to range at ranges infinitesimally prior to and beyond r_x will be the same. Hence, Eq. (2.16) will be zero, thus there is no discontinuity and so no echo is generated. At those ranges r_x where there *is* a discontinuity in one of the n th order derivatives though, Eq. (2.16) will have a non-zero value and hence an echo will be generated.

Discontinuities in cross sectional area or any of the higher order derivatives of area with respect to range are thus responsible for the formation of echoes. Freedman termed these echoes “image pulses”, since their structure is identical to the transmitted pulse in all but amplitude.

2.3.2 Example: The Sphere

Take the example of a sphere as shown in Fig. 2.2 below, with a radius of a , the point nearest to the transmitter located at r_1 (shown inline with $D(A,1,1)$ & $D(A,1,2)$) and its equator at located at r_2 (shown inline with $D(A,2,2)$),

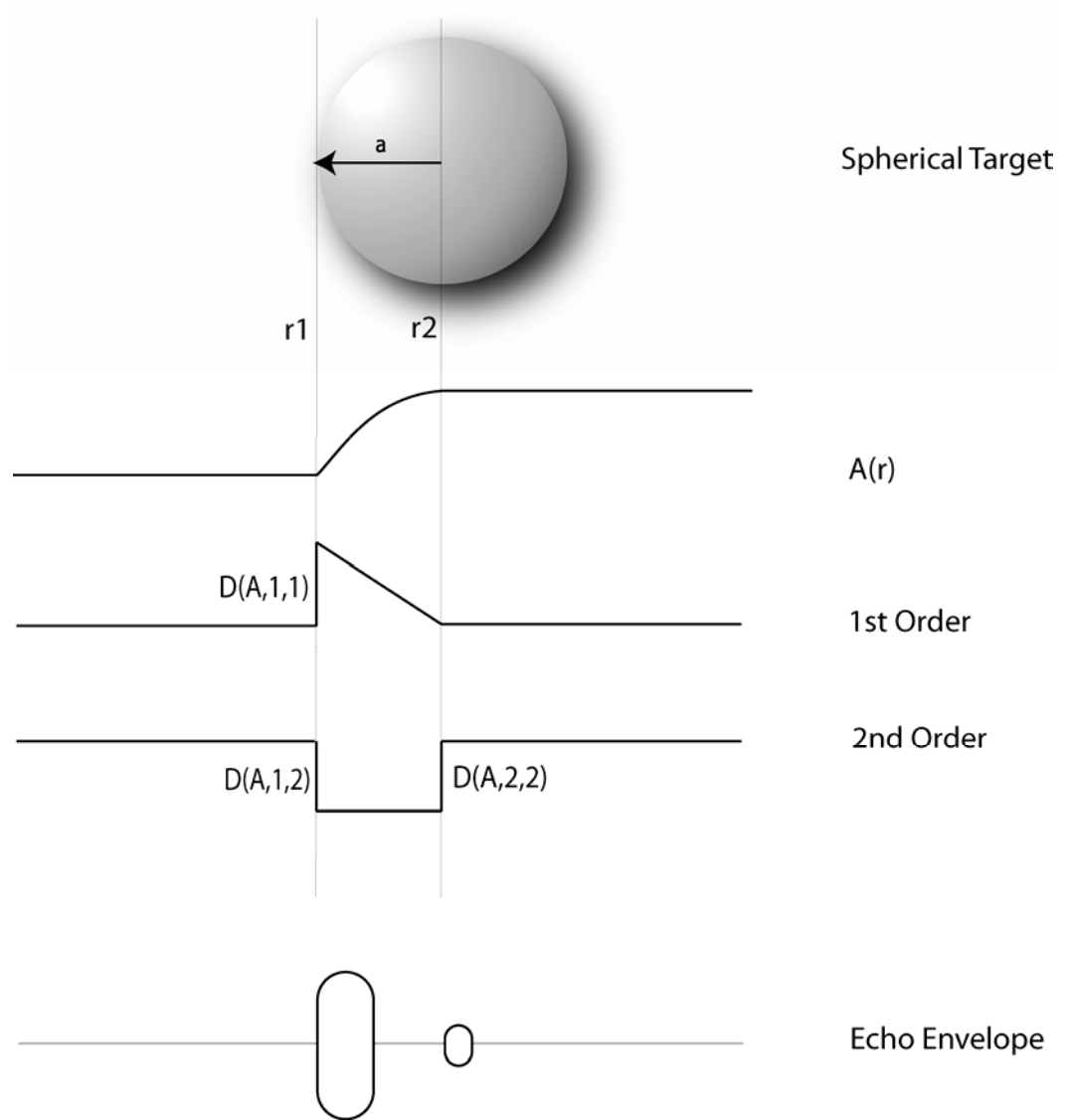


FIG. 2.2. Echoes from a sphere as predicted by Freedman's model.

Freedman showed that the n th order derivatives of area with respect to range, between r_1 and r_2 , are as follows,

$$A_w(r_g) = \pi(a^2 - (r_2 - r_g)^2) \quad (2.17a)$$

$$\frac{dA_w}{dr}(r_g) = 2\pi(r_2 - r_g) \quad (2.17b)$$

$$\frac{d^2 A_w}{dr^2}(r_g) = -2\pi \quad (2.17c)$$

$$\frac{d^3 A_w}{dr^3}(r_g) = 0 \quad (2.17d)$$

The magnitudes of the discontinuities at r_1 and r_2 are then calculated using Eq. (2.16) and are as follows,

$$D(A_w, r_1, 0) = 0 \quad (2.18a)$$

$$D(A_w, r_1, 1) = -2\pi a \quad (2.18b)$$

$$D(A_w, r_1, 2) = 2\pi \quad (2.18c)$$

$$D(A_w, r_2, 0) = 0 \quad (2.18d)$$

$$D(A_w, r_2, 1) = 0 \quad (2.18e)$$

$$D(A_w, r_2, 2) = -2\pi \quad (2.18f)$$

The cross sectional area of the sphere, as “seen” by a transducer located to the far left of the sphere, is not discontinuous at any point. However, at r_1 the first and second order derivatives *are* discontinuous and so each produces an echo. These are in phase and superimposed to form the echo from r_1 . Similarly, at r_2 , the equator of the sphere, the second order derivative is discontinuous and an echo *should* originate from there too, at least in theory. It will be shown later though, that no echo will be generated at the equator, despite the predictions of Freedman’s model.

2.4 Feasibility of Freedman's Model

Having examined the model from a theoretical standpoint, the question remains as to how feasible the model is for our purposes. Since our objective is the development of an inverse model, the fact that it's an analytical model makes it an ideal candidate, since only analytical equations can be inverted. The experimental evidence to support it is tenuous at best however. Freedman conducted a series of experiments in an underwater environment whereby large steel spheres were irradiated with acoustic pulses. The received echoes verified the model on a qualitative level, in that they came from those parts of the spheres that the model predicted, but the noise in the signals was between 20 to 30% and so conclusions couldn't be drawn as to the quantitative validity of the model. Freedman also speculated that internal penetration of the target by the pulse may have corrupted the results. Unfortunately, no follow up research on this model was published in the years following the publication of his thesis, by either Freedman himself or others in the field. Nevertheless, despite the absence of any concrete experimental verification of the model, it is a model with a solid theoretical grounding and as such deserved to be followed up with further research, as this thesis has done.

The other issue that affects the feasibility of the model is the role that the assumptions made in the derivation have played in limiting its scope. Some of the assumptions made are reasonable and are of no concern, such as the requirement that the model deals with only one object at a time, the scattering body is static, the distance to the receiver is far, etc... Others however, such as assuming the system is within a non-dissipative fluid medium and the transducer and receiver are coincident points are problematic. However, these issues can all be dealt with by extending the model to account for these deviations from ideal conditions and this is the topic of the following chapter.

3 Extensions to Freedman's Model

We now have a simple model for calculating the echo received from a scattering body produced by one or more discontinuities at a range r_g on the body. But Freedman's model, as it stands, is idealised in that it only works for objects in media with negligible energy attenuating properties, such as water, using a coincident point source transmitter and receiver. To enable the model to work in a gas, specifically air, with real transducers and receivers, which may be non-coincident, we need to compensate for several factors. These are, (a) attenuation due to air, (b) breakdown of the assumption $r_m^{-2} \approx r_g^{-2}$, (c) polar directivity of the transducer, (d) directivity of the receiver and (e) non-coincidence of the transmitter and receiver. Although (c) and (d) do not represent additions to the model, as Freedman already accounts for transmitter and receiver directivities, we will provide an alternate method for calculating them. Finally, the real component of the model needs to be extracted, since this corresponds to the physically observable signal.

3.1 Signal Attenuation Due to Air

Several mechanisms are responsible for the loss in energy of a wave travelling through air. Apart from the obvious geometrical spreading loss, which Freedman's model accounts for, atmospheric absorption causes the wave to decay exponentially with range. In the frequency range of interest to us (around 50 kHz), this absorption is due primarily to the vibrational relaxation of oxygen molecules¹⁰.

The atmospheric absorption experienced by a wave scattered at a range r_g is incorporated into the model by the addition of the term $\exp(-2r_g\alpha)$ into Eq. (2.15),

$$E_g = i \frac{VP(f)H(f)}{r_m^2 \lambda} \exp(-2r_g\alpha + i\theta) \sum_{n=0} \frac{D(A_w, g, n)}{(2ik)^n} \quad (3.1)$$

The new term is the attenuation factor and α is the absorption coefficient. The path length $2r_g$ is used because the radiation travels from the transmitter to the scattering object and then reflected back to the receiver over the same distance. Note also that from this point onward the designation for the imaginary number will be represented by scientific standard of i rather than the engineering standard of j .

The absorption coefficient α can be determined either theoretically or experimentally. Theoretical values can be determined using the series of equations specified by the American national standard method for calculating attenuation in air⁹. At the frequencies we use, these give us an absorption coefficient accurate to within 10%. Given that the amplitude of a spherical wave travelling through an attenuating medium is given by $E = \frac{E_0 \exp(-\alpha r)}{r}$, where E_0 is a constant of proportionality, the amplitudes of the wave at two distinct ranges r_1 and r_2 would be given by $E_1 = \frac{E_0 \exp(-\alpha r_1)}{r_1}$ and $E_2 = \frac{E_0 \exp(-\alpha r_2)}{r_2}$ respectively. These equations can be rearranged and equated to produce the following,

$$\alpha = \frac{\ln\left(\frac{E_1 r_1}{E_2 r_2}\right)}{r_2 - r_1} \quad (3.2)$$

Experimental values can therefore be determined by positioning the receiver at two distinct ranges r_1 and r_2 from the transmitter and inserting the amplitudes of the received waves E_1 and E_2 into Eq. (3.2),

Now, the voltage E can only be measured to within an 0.8% accuracy in 95% of cases, for reasons to be outlined later. In the worst-case scenario of E_1 being 0.8% too large and E_2 being 0.8% too small, the absorption coefficient will be in error by 10%. Consequently, both the experimental and theoretical methods can only claim accuracy to within 10% and so the method chosen is arbitrary. Since the absorption coefficient can be calculated relatively quickly with the aid of a mathematical package, provided environmental conditions are known, we chose the theoretical approach.

3.2 Breakdown of $r_m^{-2} \approx r_g^{-2}$ assumption

To simplify the derivation of the model, Freedman assumed that the object was sufficiently far from the transducer that the ranges to different points on the scatterer could reasonably be approximated with the mean range r_m , for the purposes of calculating the geometrical spreading loss. At ranges of less than two meters though, this approximation clearly does not hold when we are dealing with objects of up to 0.1m in size.

An analysis of Freedman's derivation reveals though that the approximation is only necessary if one treats the separate echoes coming from different points on the scatterer as all belonging to the same wave train. If we treat each echo as a separate

entity, we can justifiably use the exact range r_g instead of r_m . Hence we can replace r_m with r_g in Eq. (3.1) to give us,

$$E_g = i \frac{VP(f)H(f)}{r_g^2 \lambda} \exp(-2r_g \alpha + i\theta) \sum_{n=0} \frac{D(A_w, g, n)}{(2ik)^n} \quad (3.3)$$

As an example of how this changes the predictions of the model, for a typical 0.1m radius sphere at a distance of 0.8m, with an absorption coefficient of 0.2, there is a 15% increase in the amplitude of the calculated echo over that predicted by the original model.

3.3 Polar directivity of the transducer

Because the transducer is not a point source but is instead analogous to an oscillating plane piston, there will be an angular variation in the intensity of the sound pressure about the transducer. This occurs because the field at any point is a summation of waves coming from different points across the face of the transducer. Consequently, not all waves arrive in phase and we get interference, producing the characteristic series of maxima and minima. Measurements conducted at the Fraunhofer Institute in Stuttgart in an anechoic chamber confirmed that the radiating plane piston is an accurate model of a chirping transducer, the model becoming invalid only when the transducer transmits continuously, due to streaming effects¹¹.

We've used a Polaroid transducer with a radius of 1.9cm in our experiments and it's directivity field, calculated using the plane piston model¹², shown previously in Fig.

2.1. The central lobe insonifies a region of 15° around the axis of the transducer, giving it a total coverage of 30° . From Fig. 2.1 though it is clear that the field strength falls off rapidly once we deviate from the axis. Consequently, when modelling the echo generated from a point on an extended object we need to take into account the diminished field strength of the incoming radiation at that point.

Freedman's model compensates for the directivity of the transducer, as well as the receiver, by requiring that the reflecting area $A(r)$ on extended scatterers be weighted for directivity, to give us $A_w(r)$. This addresses the problem in an indirect manner by retaining an assumption of uniform directivity in transmission and reception, by virtue of the model's point source approximation, and replacing the true area with the notion of a pseudo area. Our approach is to retain the true area and instead replace the assumption of uniform directivity with a model governing the directivity of the field. Although mathematically both approaches are ultimately equivalent, the strength of the latter is that it is physically and intuitively valid also. This is because it doesn't require the introduction of the abstract notion of a pseudo area and doesn't retain an incorrect model of the directivity of the transducer.

The directivity field of a plane piston is given by the following⁸,

$$\beta(\phi) = \frac{2J_1(ka \sin \phi)}{ka \sin \phi} \quad (3.4)$$

where $k = \frac{2\pi f}{c}$ = wave number of the transmitted wave

J_1 = Bessel function of the first order.

The factor $P(f)$ in Freedman's model represents the transducer's capacity for transmission with its value denoting the pressure produced at one meter along the axis, per volt applied to the transducer, for a given frequency. To incorporate the directivity of the transducer into Freedman's model, we need to scale this factor with Eq. (3.4). The resulting model follows,

$$E_g = i \frac{VP(f)\beta_p(\phi)H(f)}{r_g^2 \lambda} \exp(-2r_g \alpha + i\theta) \sum_{n=0} \frac{D(A,g,n)}{(2ik)^n} \quad (3.5)$$

Scaling Eq. (3.4) in this manner is only valid if the scatterer is *radially symmetric* about its axis, where the directivity is constant around the perimeter of all strips from r to $r + dr$ along the length on the scatterer. In the more general case where the directivity pattern is *not* constant around the perimeter of each of these strips, for a non-radially symmetric object, the directivity term would have had to have been included within the integral for each r to $r + dr$ contribution to the total echo. However, this model will only be applied to radially symmetric objects and as such the scaling we have applied is valid.

For echoes originating from points along the axis, the directivity takes on unit value. Echoes from points off the axis are now compensated for by taking into account the angle they make with it.

3.4 Directivity of the receiver

There are two distinct transmitter/receiver configurations that we use throughout the course of our research, the so-called "coincident" case being when the transmitter

and receiver are, as the name suggests, coincident. This occurs when the transmitter and receiver are the same device and in our work this is achieved by switching the Polaroid transducer into reception mode after initial transmission. The opposing configuration, labelled the “non-coincident” case occurs when the transmitter and receiver are different devices separated by a small distance. In this case, the transmitter is still the Polaroid transducer, but the receiver is a 7mm diameter Bruel & Kjaer condenser microphone (type 4135), separated from the transducer by 44mm.

Freedman’s model assumes that the receiver is not an extended object and as such has a uniform directivity in reception. By virtue of it’s small size, this assumption holds true for the condenser microphone with it’s directivity relatively uniform over the range of angles (-40° to +100°) that it receives echoes from¹³. Consequently, the directivity of the receiver is not an issue for non-coincident set-ups.

For the coincident cases though, when we use the Polaroid transducer for reception, the directivity of the transducer must be accounted for. The angular sensitivity of the transducer in reception mode is exactly the same as it is in transmission mode and is governed by Eq. (3.4). This is because the directivity is a function of the transducer’s geometry, which remains the same in both cases and so the directivity doesn’t change.

The factor $H(f)$ in Freedman’s model represents the receiver’s sensitivity in the direction of the axis, for a given frequency. To incorporate the receiver’s directivity into the model, we need to scale this factor with Eq. (3.4). The resulting model is given in Eq. (3.6),

$$E_g = i \frac{VP(f)\beta_P(\phi)H(f)\beta_H(\phi)}{r_g^2 \lambda} \exp(-2r_g\alpha + i\theta) \sum_{n=0} \frac{D(A,g,n)}{(2ik)^n} \quad (3.6)$$

As stated earlier, when using the microphone, the directivity takes on unit value to indicate uniformity.

3.5 Non-coincident Transmitter and Receiver

Freedman's model assumes that the transmitter and receiver are coincident. The advantage of this is that when dealing with echoes originating from a ring of radially equidistant points around the axis, such as the base of a cone, the echoes from each point will all arrive at the receiver in phase. This eliminates the problem of wave interference. However, for non-coincident configurations, which constitute 50% of cases in our research, this assumption doesn't hold and needs to be compensated for.

To examine the effect of unchecked interference, we measured the maximum amplitude of echoes from the base of a cone as the microphone was shifted progressively further away from the transducer. The results are shown in Fig. 3.1. below and show a sinusoidal variation in amplitude which is characteristic of an interference pattern.

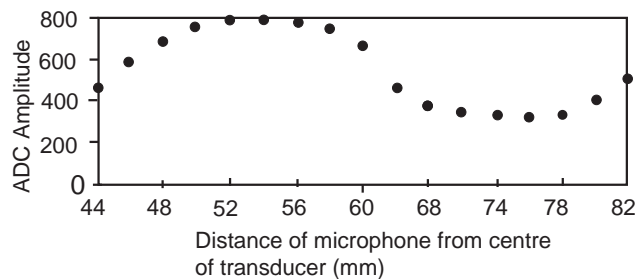


FIG. 3.1. Maximum amplitude of the echo versus separation of the microphone from the centre of the transducer.

As mentioned before, for coincident cases the transducer doubles as both a transmitter and receiver, satisfying the above assumption and so interference is not an issue in these cases. For the remainder though, the problem is minimised by aligning the axis of the scatterer with a point midway between the centre of the transducer and the microphone, as shown in Fig 3.2 below. This ensures that the path lengths L from the transducer to the scatterer and then to the microphone remain equal at all times, ensuring that the echoes arrive in phase.

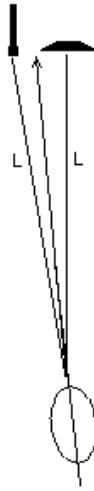


FIG. 3.2. Alignment of the scatterer to ensure equal path lengths for the transmitted and reflected waves.

Also, $A(r)$ as sensed from the vantage point of the receiver will be different in the non-coincident case to that of the coincident one since the received echo no longer propagates along the object axis. Because the model, being based upon an assumption of transmitter/receiver coincidence, does not account for this, it will manifest itself as a discrepancy in the results. By aligning the scattering body in the manner shown in Fig. 3.2, the deviation of $A(r)$ from the coincident case, as sensed at the receiver, is at least minimised due to the reduction of the angle between the object's axis and the trajectory

of the received echo of path length L . The impact, or lack thereof, of the deviation in $A(r)$ from the coincident case upon the results for non-coincident configurations will be discussed in section 5.2.

3.6 Extraction of the Real Component

Although waves are regularly represented by complex equations, the measurement process can only detect the real component. Consequently, before we can utilise Eq. (3.6), we need to extract its real part. This is given in Eq. (3.7),

$$E_g = A(f) \frac{GV\beta_P(\phi)\beta_H(\phi)}{r_g^2} \exp(-2r_g\alpha) \left(D(0)\sin\theta - \frac{D(1)}{2k} \cos\theta - \frac{D(2)}{4k^2} \sin\theta \right) \quad (3.7)$$

A factor G , signifying gain, has been added to account for any amplification that may be applied to the received signal. In Eq. (3.7) the factors $P(f)$, $H(f)$ and λ , which we use $\lambda = c/f$ to calculate, have been combined into a single function $A(f)$ which is defined:

$$A(f) = -\frac{P(f)H(f)}{\lambda} \quad (3.8)$$

The negative sign in the function above is there simply to alter the form of the terms in the parentheses of Eq. (3.7) from $(-X + Y + Z)$ to the more economical $(X - Y - Z)$ form.

We can combine terms in this manner because the individual factors need not be measured independently, for a given frequency, then combined in order to calibrate the

model. Instead, by measuring the echo from an object of known dimensions at a given range, we can insert the echo amplitude, scatterer's discontinuity values, range, frequency and calculated values of speed of sound and attenuation, from the environmental conditions, into Eq. (3.7) to determine $A(f)$. Since $A(f)$ is independent of the scattering body, the calibrated model is thus suitable for use with a range of objects at a range of distances, provided we use the same frequency that was used to calibrate the model and the speed of sound remains the same.

The extensions to the model having been made, we can now examine the procedures required to test it's validity.

4 Experimental Design

There are several components that constitute the experimental apparatus. Firstly, the 12-bit chirp (transient wave) generator card within the Macintosh PowerPC designed by Michael Milway & Assoc. Prof. Phillip McKerrow of the University of Wollongong. The output voltage of this card is controlled via a custom designed software package by Benjamin Stanley¹³, also of the University of Wollongong, that enables variation of the significant parameters, such as the maximum voltage (0 to 5 Volts in amplitude), number of wave cycles, frequency, etc., to allow production of a sine wave with the desired envelope. The software also has the ability to produce sawtooth and square waves, and impulses, but since our model is based upon the scattering of *monotonic* (single frequency) waves, we've had no need to employ non-sinusoidal waves in our research.

For non-coincident measurements (ie. the transducer and receiver are at different point in space), we produce a 10 to 20 cycle wave with an amplitude of four volts, at a frequency of 50 kHz. A wave with 10 to 20 cycles is an acceptable compromise between the need to keep the transient short enough to prevent overlapping of echoes from separate discontinuities and the need to keep it long enough for it to be considered generally monotonic. A transient wave can never be truly monotonic (only continuous waves have this distinction) because any transient is effectively a convolution between an impulse function and a continuous wave. The impulse function is responsible for high frequency components being present in the transient wave but if the impulse function is long enough, in our case the equivalent of approximately 10 – 20 cycles of the continuous wave, then the higher frequencies are negligible. An amplitude of four

volts, slightly below the maximum voltage of five, was chosen because the output was found to be non-linear when the maximum value was chosen.

The analog signal produced by the card, by virtue of the digital to analog converter at its output, is fed through to an amplifier with a gain of 30 and a 150 volt bias is then added. The amplified signal is then applied to a 44mm diameter Polaroid transducer and transmission follows. The entire experimental set-up is shown in Fig. 4.1 below,



FIG. 4.1. Experimental set-up used for chirp transmission and echo reception.

After transmission commences, the first few cycles of the transmitted wave steadily increase in amplitude, since the transducer cannot respond instantaneously to the applied voltage, and by the fifth or sixth cycle the wave has reached its maximum value. This can be seen in Fig. 4.2, the captured echo from the front face of a large truncated cone (100mm height, 197mm base diameter and 149mm truncated face

diameter) at a range of 800mm for a non-coincident transmitter and receiver. The last several cycles of the wave, not shown in Fig. 4.2 but visible in Fig. 4.3, are the result of “ring down” after the applied voltage has terminated and these decay exponentially.

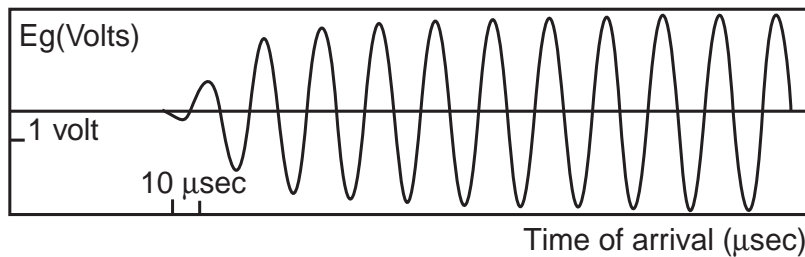


FIG. 4.2. Echo from the front face of the large truncated cone at a range of 800mm for a non-coincident transmitter and receiver.

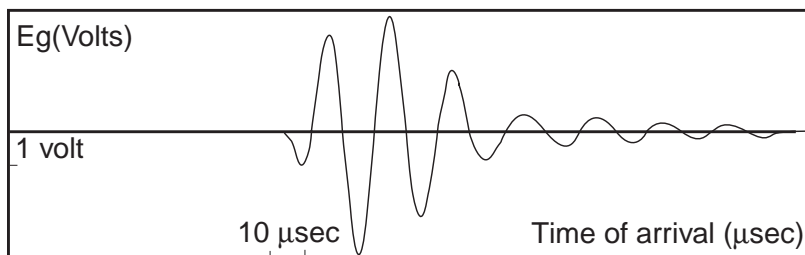


FIG. 4.3. Echo from the front face of the large truncated cone at a range of 800mm for a coincident transmitter and receiver.

For coincident measurements, where the Polaroid transducer acts as both transmitter and receiver, the process differs in that the initial output of the chirp card is a step function which drops from five volts to zero within $0.2 \mu\text{s}$. At the transducer, this causes the AC voltage applied to drop from 300 volts to zero almost instantaneously causing the transducer to exponentially ring down at it's natural frequency of approximately 55 kHz. Typically, the transmission in this case contains one or two well-defined cycles at the start of the wave and a number of trailing cycles that are

progressively buried in noise. This is shown in Fig. 4.3, the echo from the front face of the large truncated cone at a range of 800mm for a coincident transmitter and receiver. A signal such as this, with only one or two well-defined cycles, deviates from the assumption of monotonicity required by Freedman's model, but does not risk the interference issues that may arise with the non-coincident set-up. It is difficult to speculate at this stage which of these two factors will prove more important to the accuracy of the model.

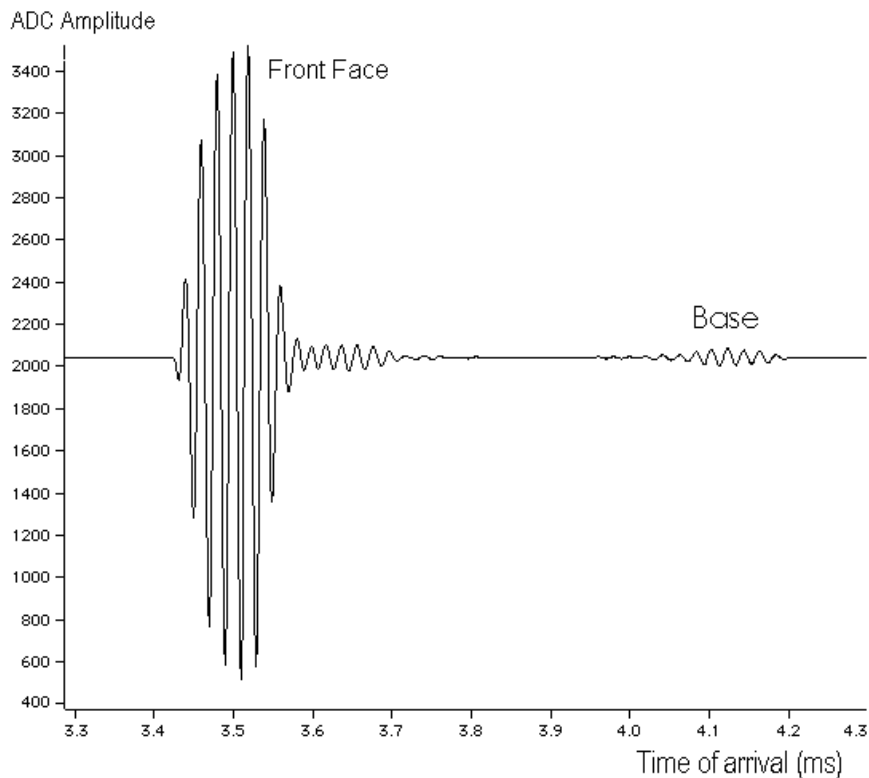


FIG. 4.4. Echoes from a medium sized truncated cone at a range of 600mm for a non-coincident transmitter and receiver.

The echo from the scattering body is received via the ultrasonic microphone, with a corresponding preamplifier, in the non-coincident case and the transducer in the coincident case, which goes into reception mode immediately after the step function is

applied. In both cases, the signal is then optionally amplified before being sampled at 1 MHz with 12-bit resolution by a chirp capture card designed by Michael Milway & Assoc. Prof. Phillip McKerrow of the University of Wollongong. This card is also within the Macintosh PowerPC and is controlled via the same custom software that was used for controlling the chirp generator card. The signal is then displayed on screen and exported to a file for later analysis with a mathematical package.

Fig. 4.4 shows a received signal that includes two echoes from the one object, in this case the echoes from a medium sized truncated cone (100mm height, 197mm base diameter and 97mm truncated face diameter) at 600mm for a non-coincident transmitter and receiver. The larger echo is from the truncated face of the cone and the second, smaller echo is from its base. The transmitted pulse was shorter than usual to ensure no overlap between the two echoes. This was done for illustrative purposes only, to clearly delineate between the two echoes. In practice though, short-duration pulses don't satisfy the requirement of monotonicity and so would not be used, the co-incident case being the exception, as already pointed out. In our experiments, described in the following chapter, we actually used pulses of longer duration, at least 10 cycles, to ensure monotonicity.

4.1 Noise Minimisation

Due to the weak echoes that we often have to deal with in this research, localisation and minimisation of noise sources is an essential prerequisite. The low intensity of the reflected echoes is not only a result of the physical limitations of our equipment, but also a symptom of Freedman's model itself. The amplitude of the $(n+1)th$ order image pulse, represented by the $(n+1)th$ order term within Eq. (3.7), is

typically at least two orders of magnitude smaller than the n th. Consequently, we need a signal with a high signal to noise ratio in order to see the higher order contributions.

The noise that we'll examine here comes from three main sources: the environment, the transducer and the chirp capture card.

A. Environment

In the lab environment under which our research was done, short-term fluctuations in air pressure from drafts, doors opening/closing, power supply fans, people walking, etc. can cause variations in amplitude of the received echo by up to 10% between any two successive measurements. Specifically, we found that the standard deviation for any sample of amplitude measurements was approximately 3%. What this figure implies is that, assuming a normal distribution, for any single amplitude measurement, there's a 68% chance that it's within 3% (one standard deviation) of the population mean and a 95% chance that it's within 6% (two standard deviations) of the mean, the "population mean" here representing the amplitude one would expect in the absence of random noise sources. It also implies that for a small number of measurements, less than 5%, the deviation of the amplitude from the mean would be greater than 6%, in some cases as high as 10% as observed.

Since we need a relatively accurate measure of amplitude to work with, it would be advantageous for us to obtain an estimate of the population mean of the amplitude, as this figure represents the amplitude devoid of the influence of random noise. To obtain this we take a sample of amplitude measurements, calculate the mean and repeat the procedure several times, producing several estimates of the population mean in the process. These estimates constitute a distribution of means with a standard deviation that varies depending on the sample size used, with larger sample sizes obviously

producing smaller standard deviations and thus a more accurate estimate of the population mean.

Using a sample size of 50, which is to say we average the amplitudes of the echoes from 50 readings, the standard deviation of the distribution of means is only 0.4%. What this implies is that when we average 50 echoes, our estimate of the population mean of the amplitude is accurate to within 0.4% in 68% of cases and accurate to within 0.8% in more than 95% of cases. Thus a sample size of 50 was deemed adequate for the task at hand and in all of our subsequent measurements we averaged over a minimum of 50 echoes before analysing the results. In each case, the measurements were completed within 30 seconds because the capture software was able to average the echoes in real time.

Over the course of several minutes, the environmental conditions in a room, such as temperature, pressure and humidity, can and do change. In a laboratory environment this is primarily due to air conditioner cycles. Also, over a period of several hours these same conditions will drift due to atmospheric changes occurring over the normal course of the daily cycle. This will affect the time of flight, via the speed of sound, and amplitude, via attenuation factor, of an echo. The model is designed to compensate for these changes provided we know what the environmental conditions are at the time of measurement. Thus, continual monitoring of these conditions is required.

B. Transducer

As we mentioned earlier, the final cycles of the transmitted wave are the result of “ring down” after the voltage applied to the transducer has terminated and these cycles decay exponentially. This decay is very long however and often the ringing will not have completely attenuated by the time the echo arrives. When the transducer is being

used as a receiver, the ring down signal will be superimposed on the incoming echo, consequently interfering with the received signal. When the microphone is used for reception, it will pick up the ring down signal via one of the outer side lobes (see Fig. 2.1), again resulting in corruption of the signal. To solve this problem, the ring down signal, which is fairly repeatable, is recorded separately in the absence of any scattering body and later on, as part of the echo analysis, subtracted from the measured echo. This also has the advantage of cancelling any extraneous echoes, from objects in the environment unaccounted for, which may be present in the signal.

A different problem, which reveals itself only after several hours, is the slow but significant reduction over time in the amplitude of the received echo from a scatterer. This was measured from a reference target and the results, given in Fig. 4.5, show a 4% reduction within one hour and 18% over seven hours, after which the amplitude no longer decreases significantly. We concluded, after isolating the source of the drift to the transducer itself, that the changes are a result of the transducer losing its ability over time to produce a given pressure for a given voltage. We believe this reduction in transmissivity may be due to the mylar film used in the transducer stretching under a constant 150V bias and losing its rigidity as a consequence.

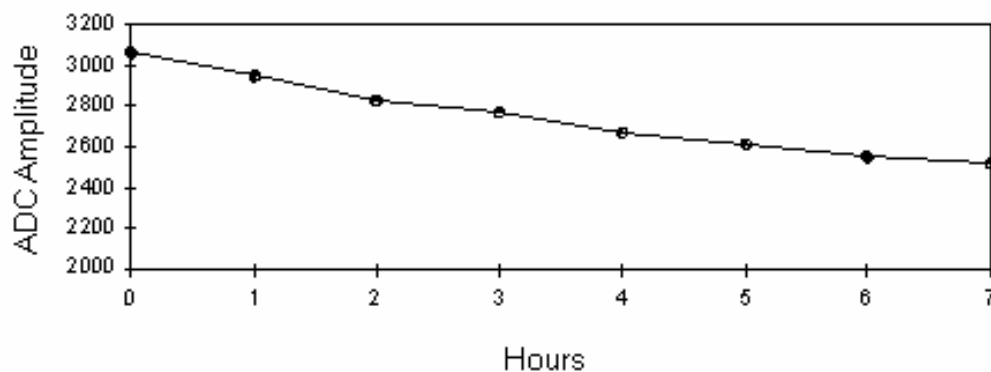


FIG. 4.5. Variation in measured amplitude with time of the echo from a target.

To compensate for this drift we switched off the bias to the transducer between measurements. This relieves the tension on the mylar film between transmissions and allows it to restore it's rigidity.

C. Chirp capture card

The capture card is a host for several potential noise sources. Because the card is in close proximity to the chirp generator card, as well as numerous electronic components within the host computer, the potential for electromagnetic interference is great. To minimise this, we used coaxial cable for the wiring between the input socket and the analogue to digital converter (ADC). The ADC itself was shielded by copper plates to prevent interference from external and on-board noise sources. Initial prototypes for these cards didn't include these enhancements and the resulting noise was appreciable.

The capture card begins sampling the incoming signal as soon as the generator card begins transmitting. Because we are superimposing the echoes in real time though, for the purpose of averaging them in order to increase the signal to noise ratio, the incoming waves must be in phase with one another, otherwise they will experience interference. As a consequence, the circuit was designed to ensure that the start of the transmit and receive cycles are synchronised to start on the same edge of the signal, to prevent phase mismatch.

Finally, the sampling rate of the ADC places a constraint on the accuracy of the captured signal. At a sampling frequency of 1 MHz, a typical 50 kHz wave will be sampled 20 times per cycle, or every 18° . Since our objective is to measure the amplitude of the peaks, for reasons to be outlined shortly, the best case scenario, in

terms of accuracy, occurs when the wave is sampled exactly at its peaks. The worst case is when the sampling occurs at a separation of 9° on either side of the peak, leading to an inaccuracy in the measured peak of 1.2%. To resolve this issue, we use interpolation¹⁵ to reconstruct the shape of the wave between the sample points. This is done with the aid of a mathematical package during the analysis stage, an example of which can be seen in Appendix A.5 (a).

4.2 Echo Analysis

The capture software allows us to export the returned signal to a file for later analysis with Mathematica. Once the file is imported into Mathematica, the first step is to cut out the unnecessary parts of the trace. Since a typical trace consists of an appreciable period of no signal followed by the echo and then no signal again, it is advantageous to remove the regions that are not part of the main echo since it will reduce processing time markedly later on. Once this is done, the trace of the signal received in the absence of any scattering body is imported and subtracted from the echo, as outlined previously. Appendix A.5 (a) contains an example of this process also. This second trace must be obtained within a very short time after the initial echo was recorded, when the temperature, pressure and humidity are still almost the same as when the initial trace was taken, otherwise changes in these environmental conditions will adversely affect the accuracy of this method.

Interpolation of the processed echo follows and we've chosen to interpolate ten points per sample, giving us a virtual sampling frequency of 10 MHz. The interpolation is more accurate when the wave is monotonic and of constant magnitude. Consequently, the highest accuracy in the interpolated echo occurs in its central region, where the

wave's magnitude has stabilised and ring-down has yet to begin. This stable central region has the added advantage of conforming more closely to Freedman's assumption of a non-varying echo envelope. Since the objective of our work is to compare the measured amplitude with the predicted amplitude of the echo at a point in time, we need to find an appropriate region within the echo from which to select our measurement point. For the reasons detailed above, the central region of the echo is the most appealing for this. The appropriate tools within the mathematical package are then used to determine the maximum value of the newly interpolated echo. This will always be a positive peak located within the central region. Now that we have the measured value of E_g , we can turn our attention to using the model to calculate a theoretical value of E_g .

By this stage, we know, or can easily calculate, almost all of the factors that are needed for calculating the theoretical value of E_g . The only unknown remaining is the phase to be used within the trigonometric functions. To determine the phase we utilise the fact that for the three trigonometric terms in Eq. (3.7), one will always dominate the others. To determine which term dominates, prior knowledge of the wave number and the n th order discontinuities of the scatterer are required, in order to calculate the coefficients for the trigonometric terms. Consequently, if the cosine term dominates, then the positive peaks of the echo correspond to phases of $2\pi n$ where $n=1,2,3$, etc. If one of the sine terms dominate, then the positive peaks correspond to phases of $2\pi n + \frac{\pi}{2}$ where $n=1,2,3$, etc. Even though we don't know the value of n corresponding to the peak that we measured, it doesn't matter because the trigonometric function takes on unit value for all integer values of n . Thus, the value that one uses is arbitrary, provided it's an integer.

The treatment given above assumes that the non-dominant terms play a negligible role in affecting the phase of the wave. Is this assumption valid though? By plotting the

echo, as predicted by the model, for several typical cases of spheres, cones and truncated cones, we find that when the non-dominant terms are included, the phases of the positive peaks deviate from those predicted above by less than 2° . This corresponds to a deviation in the amplitude of less than 0.06%, confirming the validity of our assumptions.

Once the phase has been chosen, the predicted amplitude of the peak in question can be calculated and compared with its measured counterpart. The next chapter will detail the results of such comparisons for a variety of objects at different ranges.

5 Results and Analysis

For the experimental work, we used spheres, regular cones and truncated cones of varying dimensions at ranges of 800mm, 1000mm and 1400mm, accurate to within 1mm. The range is defined as the distance from the face of the transducer to the point(s) on the scatterer from which the echo originates. For example, when discussing the echo from the base of a 100mm high cone, a range of 1000mm refers to the distance from the transducer to the base, as opposed to the distance to the vertex, which would be only 900mm.

The spheres we've used have diameters of 100mm, 150mm and 200mm. The regular cones have a height (distance from base to vertex) of 100mm and base diameters of 100mm, 150mm and 197mm. The truncated cones have a height (distance from base to truncated face) of 100mm, base diameter of 197mm and truncated face diameters of 52mm, 97mm and 149mm. Unless stated otherwise, for each class of scatterer (ie. sphere, regular cone or truncated cone), the model was calibrated with a member of that class positioned at the greatest distance.

In our experiments the smallest member was always used, but the choice is arbitrary provided that the object is at least several wavelengths wide in order to satisfy Kirchoff's approximation⁷. For example, when dealing with spheres, the model was calibrated with the 100mm diameter sphere at 1400mm. The reason for calibrating with an object at the greatest distance is that the far field approximation, which is central to the model, is most accurate when dealing with scatterers that are as far as possible from the source of the wave. Consequently, the calibration constant $A(f)$ is most accurate when obtained from an object at the greatest range.

Even though $A(f)$ is independent of the geometry of the scattering body and so once calibrated could be used for other object classes, this presumes that all measurements are to be taken within a short time span because $A(f)$ is dependent upon the speed of sound, which varies with temperature. In our experiments though, the set of measurements for each object class were taken on different days, with different temperatures, necessitating the recalibration of the model for each new set.

All objects were mounted on a precision positioner with three degrees of freedom that has a range limit of 1.5m. Data for all figures used in this section, pertaining to measured and predicted amplitudes, are provided in Appendix A.4.

5.1 Experimental Results

A. Spheres

As stated earlier, it was suspected that despite the predictions of Freedman's model, the equator of a sphere may not generate an image pulse when insonified. The reason for this is that Freedman assumes that the contributions from the geometrical shadow region, generally known as "creeping waves", are negligible at the high frequencies we've used. Rudgers¹⁶ though, claimed that for the case of a sphere, these contributions are equal in magnitude and the inverse of those generated by Freedman's mechanism, the net result being a cancellation of the equator echo.

To test Rudgers' assertion, we captured the echo from a sphere and analysed the region where the image pulse from the equator should be. Given that the equator's echo would be extremely weak, only $\frac{1}{2ka}$ that of the stronger echo from the closest point on the sphere, it was necessary to use an amplification of 10^3 in order to see it, if it

existed. Despite the noise floor being significantly lower than the predicted amplitude of the equator's echo, no echo was observed, confirming Rudgers' analysis.

Consequently, the results presented here are only for the echoes from the closest points on the spheres. The discontinuity equations for the closest point on a sphere of radius a were given previously,

$$D(A_w, r_1, 0) = 0 \quad (2.18a)$$

$$D(A_w, r_1, 1) = -2\pi a \quad (2.18b)$$

$$D(A_w, r_1, 2) = 2\pi \quad (2.18c)$$

The results of comparing the measured and predicted amplitudes of the echoes are given in Fig. 5.1 for the case of a non-coincident transmitter & receiver and in Fig. 5.2 for the coincident case.

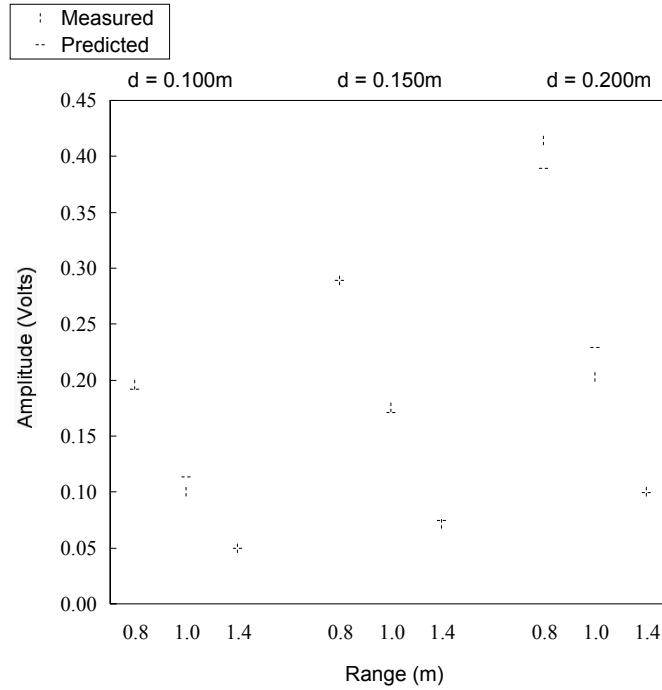


FIG. 5.1. Measured and predicted amplitudes of echoes from spheres of diameter d when the transmitter and receiver aren't coincident.

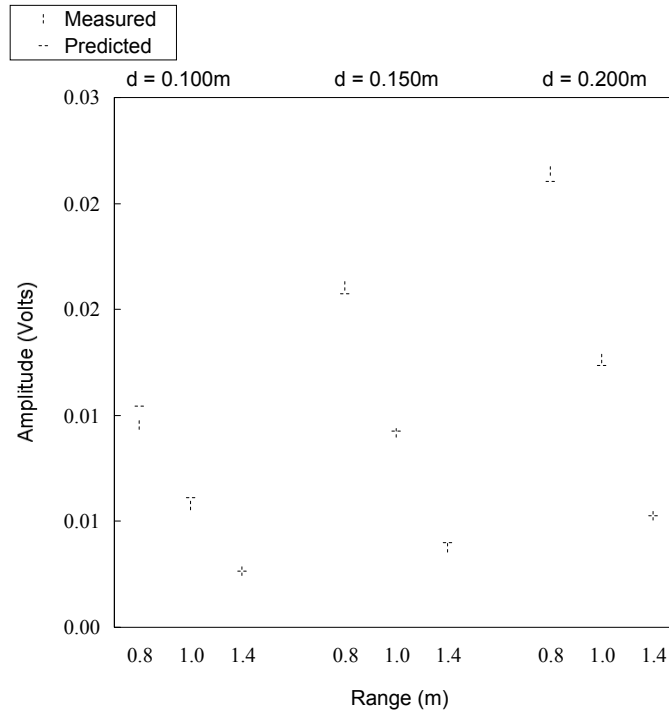


FIG. 5.2. Measured and predicted amplitudes of echoes from spheres of diameter d when the transmitter and receiver are coincident.

Note that the difference in amplitudes for Figs. 5.1 & 5.2 are a consequence of (a) different transmission mechanisms being used for the coincident & non-coincident cases and (b) differing levels of amplification applied to the captured signal. For the non-coincident case, the predictions deviated from the measured amplitudes by an average of 4.7%, the worst case being 13%. The coincident case provided better results though, with the predictions deviating from the measured amplitudes by an average of only 3.3%, the greatest error being 10%.

B. Regular Cones

Freedman's model predicts that two echoes should be generated from an insonified regular cone, one from its vertex and the other from its base. The base echo is

readily observable but the image pulse from the vertex cannot be seen. This is because it is a point and so has a negligible reflecting area, the consequence being that what little echo there is, is buried in noise despite attempts to see it with amplifications as high as 10^3 . The discontinuity equations for the vertex of a regular cone⁷ are given below,

$$D(A_w, r_1, 0) = 0 \quad (5.1a)$$

$$D(A_w, r_1, 1) = 0 \quad (5.1b)$$

$$D(A_w, r_1, 2) = -2\pi \tan^2 \gamma \quad (5.1c)$$

The only non-zero contribution to the echo is from the second order discontinuity, but as we know, its contribution is several orders of magnitude smaller than the lower order terms, resulting in a near negligible contribution to the observable echo. Thus, we can only present the results involving the echo from the base.

The discontinuity equations for the base of a regular cone⁷ are given below,

$$D(A_w, r_2, 0) = 0 \quad (5.2a)$$

$$D(A_w, r_2, 1) = \pi h \tan^2 \gamma \quad (5.2b)$$

$$D(A_w, r_2, 2) = 2\pi \tan^2 \gamma \quad (5.2c)$$

where h is the cone's height and γ is the angle between its central axis and any line connecting the vertex to the rim.

A comparison between the measured and predicted amplitudes of the echoes is given in Fig. 5.3 for the case of a non-coincident transmitter & receiver and in Fig. 5.4 for the coincident case. For the results presented in Fig. 5.3, the model was not

calibrated at 1400mm as per usual but at 800mm because the echo had been too weak, allowing noise to dominate, thus rendering it unsuitable for use as a calibrating signal. Also, high amplification was employed to compensate for the weak echo, hence the larger than usual voltages of the captured signals.

For the non-coincident case, the predictions are, on average, almost twice the size of their measured counterparts, the most extreme case being more than 3.6 times the measured value. The coincident case proved no better, with the average prediction being more than three times the measured value, the most extreme case taking it to five times. The results from the smallest cone were an exception to this, having predicted values smaller than those measured.

Later we will discuss the reasons why these predictions deviate so markedly from the measured values.

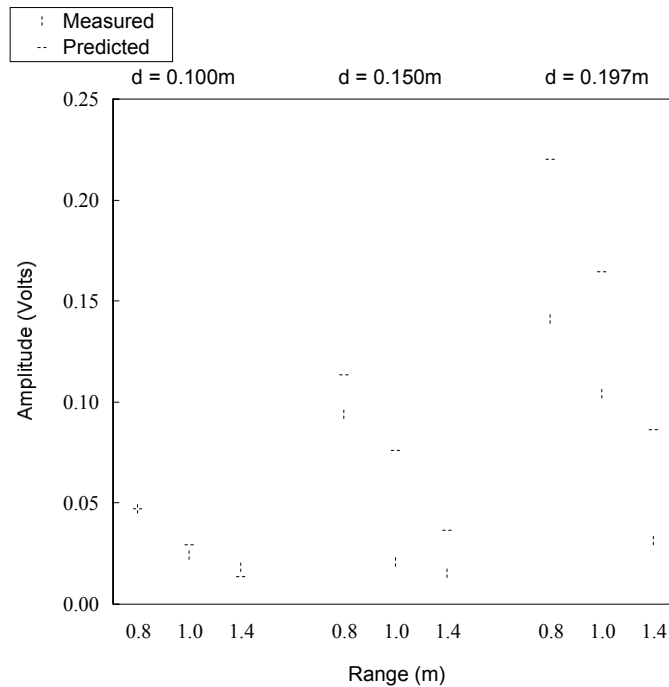


FIG. 5.3. Measured and predicted amplitudes of echoes from the bases of regular cones of base diameter d when the transmitter and receiver aren't coincident.

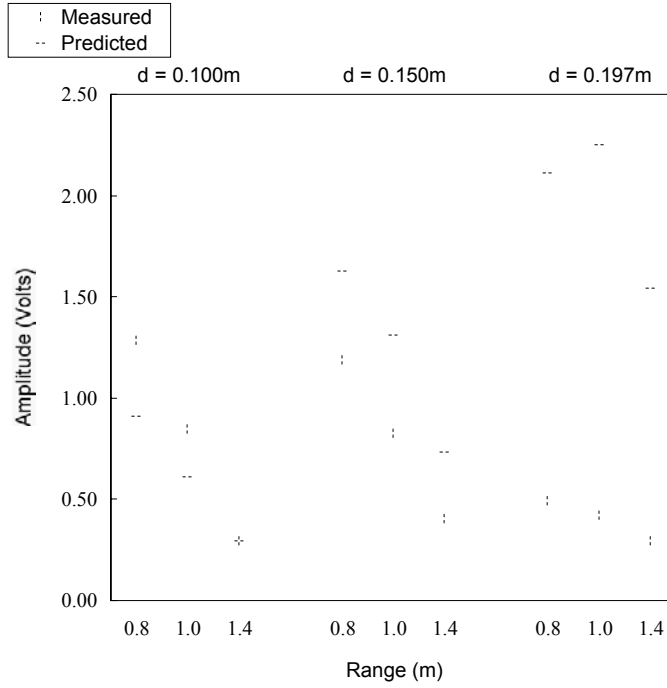


FIG. 5.4. Measured and predicted amplitudes of echoes from the bases of regular cones of base diameter d when the transmitter and receiver are coincident.

C. Truncated Cones

As with a regular cone, Freedman's model predicts that two echoes will be generated when a truncated cone is insonified. One will originate from the base and will be identical to that generated by a regular cone with the same shaped base. The other will come from the truncated face and will be significantly strong, given the large reflecting area of the face. As the mechanism of echo formation at the base of a truncated cone is identical to that at the base of a regular cone, we need not examine it again. Instead we will focus on the echo produced by the truncated face.

The discontinuity equations for the face of a truncated cone⁷ follow,

$$D(A_w, r_1, 0) = -\pi(h-b)^2 \tan^2 \gamma \quad (5.3a)$$

$$D(A_w, r_1, 1) = -2\pi(h-b) \tan^2 \gamma \quad (5.3b)$$

$$D(A_w, r_1, 2) = -2\pi \tan^2 \gamma \quad (5.3c)$$

where b is the truncated cone's height and γ is the angle between it's central axis and any line connecting the virtual vertex to the rim of the base. The virtual vertex is defined here as the vertex that would be present if the truncated cap could be reattached. The term h represents the distance from the base of the truncated cone to the virtual vertex.

The measured and predicted amplitudes of the echoes are given in Fig. 5.5 for the case of a non-coincident transmitter and receiver and in Fig. 5.6 for the coincident case.

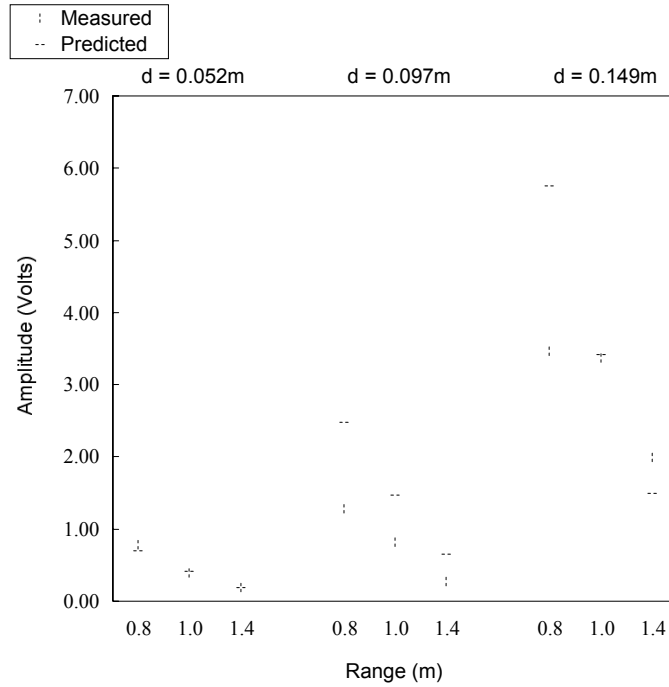


FIG. 5.5. Measured and predicted amplitudes of echoes from the faces of truncated cones of truncated face diameter d when the transmitter and receiver aren't coincident.

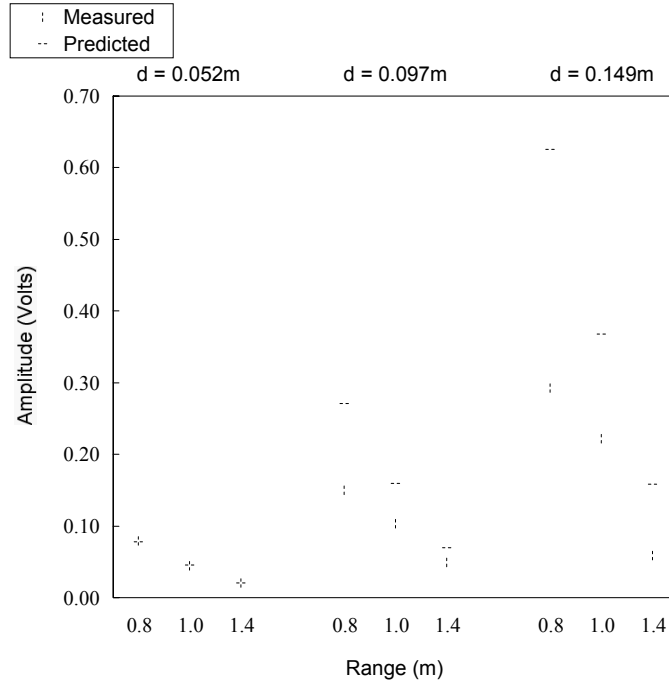


FIG. 5.6. Measured and predicted amplitudes of echoes from the faces of truncated cones of truncated face diameter d when the transmitter and receiver are coincident.

For the non-coincident case, the predicted amplitudes are, on average, 50% in error, the largest errors being predictions twice the size of the measured values. The coincident case has predicted amplitudes that are 60% too large, on average, the worst case being nearly three times larger than the measured value.

In the next section we will explore the reasons why these results, like those for the regular cones, show such a large discrepancy between theory and measurement.

5.2 Analysis

The results for the echoes from the closest points on spheres clearly show that Freedman's model works well for this class of object. Although the largest error was 13%, the average error was less than 5% for non-coincident set-ups and as low as 3.3% for coincident ones.

Sources of error that affected the results were numerous. One class of potential error sources were physical irregularities in the scattering bodies themselves. The first of these were irregularities in the radii of the spheres, which were measured and found to be 1%. Given that the amplitude of the received echo is approximately proportional to the first order discontinuity, which is itself proportional to the sphere's radius, it follows that such radial irregularities can account for errors of up to 1% in the echo's amplitude.

For regular cones, there are a couple of areas where irregularities in their shape could result in errors. The first is the slope of the cone across its surface. If discontinuities in this parameter occur, or in any of its derivatives with respect to range, which in this case could have occurred had the wood not been turned properly, they can lead to additional echoes being generated, in accordance with Freedman's model. Also, since the slope of the cone at the base affects the echo generated, if there is a deviation in the cone's slope near the base, then the generated echo will differ from that predicted. We measured the slopes of the cones and found smoothly varying and near negligible deviations in the slopes from their means thereby ruling out discontinuities as a source of error. Likewise, we found the slopes at the bases didn't deviate from their overall means either.

A second feature of cones that could have affected the results is the radii of curvature, or "sharpness" of the base rims. Since the echo from the base is generated by the process of diffraction, a curved base rim will produce an echo of lower magnitude than an ideal "sharp" rim. Because the wavelength we've used is between 6mm and 7mm and the observed radii of curvature at the rims is never greater than about 0.5mm, the radii of curvature will play a negligible part in the results obtained.

The results for the regular cones also highlighted the limitations of Freedman's model. Earlier, we discussed Rudgers¹⁶ work that showed Freedman had made an incorrect assumption about the negligibility of creeping waves generated at geometrical shadow boundaries. Because Freedman's model doesn't account for these waves, we can only speculate as to what effect they may have on echoes originating from geometrical shadow boundaries, such as the bases of cones. We believe the large deviations between the predictions of the model and the measured values for the echoes from the bases of cones can be attributed to these creeping waves from the shadow region.

The significant deviations from theory of the measured echoes from the faces of the truncated cones have a different origin than that given for the bases of regular cones. The model assumes that the separation between the scattering body and the receiver is great enough to ensure that the normal vectors at all points on the truncated cone's face are pointing directly towards the receiver. Under such conditions the amplitude of the received echo would vary linearly with the area of the truncated face, as the predicted echo amplitudes in Figs. 5.5 & 5.6 indicate. Because of the relative proximity of the transducer to the truncated cone though (1400m at most), the signal insonifying the truncated face is only *approximated* by a spherical wavefront. A more accurate description is that the area of this wavefront that is along the axis of the transducer is actually planar and equal in area to the face of the transducer, with the rest of the wavefront being spherical. Visual inspections of the results of wave propagation simulations using the Lattice Gas Model¹⁷ seem to confirm this.

As to be expected, the spherical regions of the wavefront incident upon the scattering body are reflected at angles that don't transmit them back to their source and hence are not picked up by the receiver. The central planar region of the wavefront

though does experience direct backscatter to the receiver. The upshot of this is that the only region on the truncated face which contributes to the signal captured at the receiver is that area which is irradiated with the central planar section of the wavefront. Consequently, if the truncated face is larger than the planar section of the wavefront, the amplitude of the echo received will be less than that predicted by the model. This is confirmed by the results in Figs. 5.5 & 5.6 that show the amplitudes of the measured echoes do not increase with truncated area at the same rate as the predicted amplitudes do. Another way of interpreting this is that since the central planar region will always contribute a constant component to the total energy reflected, irrespective of distance, then the law governing the propagation follows a better than inverse square model. The consequence of this is that the model can only be applied to truncated faces of very small area, generally of the order of the area of the transducer's face or smaller.

As with regular cones, irregularities in the slopes of the truncated cones could have been a source of error but as with regular cones we found the slope variations to be negligible. The radii of curvature at the rims of the truncated faces, observed to be less than 0.5mm, are not as crucial to the results as they had been for the base rims. This is because the dominant echoes result from direct backscatter, the diffracted echoes making only a minor contribution.

As well as the sources of error discussed above that are specific to a class of objects, there are general issues that could affect the results from all scatterers. One is the model's use of the far field approximation, which is valid only if the condition $kr \gg 1$ is satisfied⁷. In these cases though, with ranges over 0.8m and wave numbers typically near 10^3 , it is clear that this condition is satisfied. Even for the results of previous experiments, not given here, which showed slightly worse agreement between experiment and theory at ranges from 400mm to 800mm, the condition is still satisfied

and consequently a breakdown in the far field approximation can not be blamed for the larger discrepancies.

Small variations in the parameters of the model during the course of a set of measurements may also affect the results. The only terms that can vary during the course of a measurement session are the speed of sound and the absorption coefficient. The speed of sound has a dependence on temperature that is given by the following¹⁸:

$$c = c_0 \sqrt{T_K / 273} \quad (5.4)$$

where c_0 = the speed of sound at 273 K = 331.6 ms⁻¹

T_K = air temperature in Kelvin.

The speed of sound also has a dependence on humidity and pressure, but the variations in these that can occur over a measurement period of, at most, two hours, will cause a negligible change in the speed of sound. The greatest change in temperature during any measurement period was 2° C, the minimum and maximum temperatures being 292 K and 298 K respectively throughout the entire series of measurements. Using Eq. (5.4), this +2° C change represented a change in the speed of sound of +0.3%. Consequently, the change in the inverse of c , which the amplitude of the echo is proportional to, would have been - 0.3%. This is too small to produce any significant error in the calculated echo.

The other component of the model that can be a source of experimental error is the absorption coefficient α . Since the coefficient is rated to be accurate to within 10%, at a typical range of 1m with a typical value of α = 0.2, the error in the attenuation

factor will be 4%. The reality is though that an error in the absorption coefficient of 10% doesn't mean that it can vary from one moment to the next by up to that amount. Consequently, even if the absorption coefficient used is inaccurate by the given amount, provided the measurements are done soon after the model is calibrated, the error in the coefficient will be absorbed by the calibration process. On the other hand, if the model is calibrated one day and used on another, when the environmental conditions have changed markedly, then there is justifiable concern that the calibration is no longer valid. For the work presented here though, all the calibration data was part of the same set as the data used to test the model.

As discussed in section 3.5, $A(r)$ as sensed from the vantage point of the receiver will be different in non-coincident configurations to that of coincident ones since the received echo no longer propagates along the objects axis. Because the model, being based upon an assumption of transmitter/receiver coincidence, does not account for this, it will manifest itself as a discrepancy in the results. For spherical objects this is not an issue because $A(r)$ doesn't change for non-coincident transmitter/receiver configurations, since spherical objects have no axis as such and thus are geometrically equivalent from all vantage points. However, for echoes from the front faces of truncated cones, as well as those from the bases of cones, $A(r)$ will deviate from the coincident case. The question then arises as to whether, in non-coincident cases, these changes in $A(r)$, despite our efforts to minimise them (see Fig 3.2), are significant sources of error or not.

If it were the case that these deviations in $A(r)$ produced significant errors in the model, the results for the non-coincident cases would show a greater deviation between experiment and theory to their coincident counterparts. What we observe however is that for the truncated cones, the discrepancies are similar in magnitude for both the

coincident and non-coincident cases and for the regular cones the non-coincident results are actually better than the coincident ones. Given the rather large errors inherent in the results for both configurations however, it would be presumptive to declare that the deviations in $A(r)$ in the non-coincident cases have no impact upon the results. They may well be present, but overwhelmed by the larger sources of error. All we can conclude is that any discrepancies that result from deviations in $A(r)$ are certainly not dominant sources of error in our results.

Finally, we address one of the model's assumptions that, without clarification, may raise questions about the methodology employed here. Freedman's original model made the assumption that the range to the scatterer is very large compared to the size of the scatterer itself, which is to say that the range doesn't vary appreciably over the length of the object. However, our test objects are more aptly described as being at a *moderate* range rather than a large one, a necessary trade off to ensure that we receive an echo with a high S/N ratio. Does this less than ideal range invalidate the assumption of a large range and adversely affect Freedman's model as a result? The answer to this question depends on *which* of Freedman's models we are referring to.

There is a high likelihood that Freedman's model in its *original* form would be comprised by this choice of a moderate range because that model made the assumption of a large range to the scatterer (compared to the size of the scatterer) specifically so that the approximation $r_g \approx r_m$ could be employed (ie. range r_g is approximately the same as the scatterers mean range r_m) in order to simplify the formulation.

However the extended Freedman model, which is the model we use for all our experiments, doesn't employ the $r_g \approx r_m$ approximation. It was dispensed with in section 3.2 ("Breakdown of $\mathbf{r}_m^{-2} \approx \mathbf{r}_g^{-2}$ assumption") by virtue of the fact that we treat echoes from different parts of the scatterer as distinct echoes rather than as part of one large

wave train as Freedman had. Since we don't use the $r_g \approx r_m$ approximation, we are not held to the assumption upon which the approximation was founded, that of a large range to the scatterer compared to the scatterers size and thus our choice of a moderate range for our objects in no way compromises our results. We *are* still held to the assumption that the scatterer is in the far field in order for us to employ Kirchoff's approximation though, but that is another matter and has been addressed elsewhere in the thesis.

Although the model has only been verified for spheres to within an average error of 3.3%, with the worst case being 10%, for coincident cases, this is a significant improvement over the results obtained by Freedman in his original work. He was able to verify only some qualitative aspects of the model, the quantitative results being too noisy (20-30%) to allow conclusions to be drawn. Subsequent references^{19,20} to his work have discussed only the theoretical aspects of the model and haven't touched upon the failings in his experimental data. Neither has any follow up work to verify the model, in either air or water, been done since 1962, to the best of our knowledge.

5.3 Conclusions

Although being quite accurate in determining time of flight, Freedman's model, when translated to air, is limited in that it cannot be used for modelling the echoes from the geometrical shadow boundaries of objects, such as the base of a cone. It is reasonably accurate though in calculating the echoes from the closest points on spheres and may potentially be used for modelling the echoes from the faces of truncated cones, provided these faces have a small area. It should also be reasonably accurate for predicting the echoes from objects with smoothly varying convex surfaces.

The model is of special interest to workers in the field of mobile robotics because of its potential to be used as the basis for an inverse model of ultrasonic imaging. This could lead to the development of a real-time object recognition system that would complement current systems by specialising in the recognition of non-concave scatterers or their modelling with equivalent symmetrical objects. Major applications of such a system include map building by mobile robots and object recognition on conveyor belts.

In the next section we will expand upon the forward model, using it as the starting point for the construction of an *inverse* model of ultrasonic echolocation.

6 Development of the Inverse Model

Since the forward model has been established as having validity for a select range of objects, we can take the next step of using it to attempt the development of an inverse model for this same range of objects. As will be shown, our inversion will lead to the emergence of two candidate inverse models, one time *independent* and another time *dependent*. These models do not contradict one another, they simply represent two different ways of modelling the system. For the time *dependent* model, the variations of the wave within the wave envelope at any instant are modelled, whereas the time *independent* version simply models the overall shape, the envelope, of the wave. Both have advantages and disadvantages over one another, however ultimately one of these will prove to be flawed and the reasons for this will be discussed. Finally, we will look at how the predictions of an inverse model could theoretically be used to build an image of the scatterer in question.

6.1 Time Independent Inverse Model

As the basis for both inverse models, we'll begin with the final form of the extended forward model given in Eq. (3.7) back in Chapter 3,

$$E_g = A(f) \frac{GV\beta_p(\phi)\beta_H(\phi)}{r_g^2} \exp(-2r_g\alpha) \left(D(0)\sin\theta - \frac{D(1)}{2k} \cos\theta - \frac{D(2)}{4k^2} \sin\theta \right) \quad (3.7)$$

where $A(f)$ = transfer function of the transducer and receiver at frequency f ,

G = gain, or amplification, applied to the received signal,

V = voltage applied to the transducer,

$\beta_p(\phi)$ = frequency dependent directivity of the transducer,

$\beta_H(\phi)$ = frequency dependent directivity of the receiver,

r_g = range to the source of the echo,

α = frequency dependent atmospheric absorption coefficient,

$D(n)$ = discontinuity equations for the n th order derivatives,

k = frequency dependent wave number,

and $\theta = \omega t - 2kr$, which is also obviously frequency dependent.

For reasons that will become clear, it was prudent to redefine all of the individual elements that make up the forward model, as we've done above, with particular emphasis being placed upon the frequency dependence, or otherwise, of each component.

Now, let us simplify Eq. (3.7) above by combining several components into one function $K(f)$,

$$K(f) = \frac{A(f)GV\beta_p(\phi)\beta_H(\phi)}{r_g^2} \exp(-2r_g\alpha) \quad (6.1)$$

To claim that $K(f)$ is dependent *solely* upon frequency, as Eq. (6.1) seems to do, would be incorrect. However, let us envision a situation under which we were to insonify a stationary object with several different frequencies within the span of a couple of minutes.

Firstly, the sensitivity of the transducer is dependent upon both the tension in the Mylar film during the chirp process as well as the frequency applied. The tension in the Mylar would reduce negligibly over the course of a couple of minutes, especially since we turn off the bias between measurements as a precaution against this, thus the transducer's sensitivity is solely dependent upon frequency in this case. Given the

singular dependence of the receivers sensitivity upon frequency, it follows that $A(f)$ is dependent on frequency alone during this period.

The directivities of both the transducer and receiver are functions of the frequency of the wave, its speed c and the angular bearing ϕ of the scattering object to their axes. The speed of sound is dependent upon environmental variables, primarily temperature, pressure and humidity. Within the span of two minutes, these environment conditions do not change sufficiently enough to produce a measurable change in the speed of sound. The bearing ϕ is another constant in this scenario since the scattering object remains stationary. Thus again we have frequency dependence alone.

Given the immobility of the scatterer, it follows that the range r_g is also a constant during the measurement cycle. Also, the atmospheric absorption coefficient, which has dependence upon temperature, pressure and humidity, as well as frequency, will remain a function of frequency alone in this case, as it's been established that these three environmental variables will remain virtually unchanged in the two minute measurement period. Lastly, there is the voltage applied to the transducer and the gain applied to the signal from the receiver, both of which are deliberately held constant.

Thus from the above analysis, it's clear that during the measurement cycle, the function $K(f)$ has dependence on frequency alone. Let us reformulate Eq. (3.7) into its new form then,

$$E_g = K(f) \left(D(0) \sin \theta - \frac{D(1)}{2k} \cos \theta - \frac{D(2)}{4k^2} \sin \theta \right) \quad (6.2)$$

It is at this point that the forward model diverges into two streams, the first leading to the time *independent* inverse model and the second to the time *dependent* variant. For now though, we'll only examine the former.

Using trigonometric identities, the maximum value for a superposition of several sinusoidal waves can be deduced (see Appendix A.3). This is given in Eq. (6.3) below,

$$\left| D(0) \sin \theta - \frac{D(1)}{2k} \cos \theta - \frac{D(2)}{4k^2} \sin \theta \right|_{MAX} = \left(D(0)^2 + \frac{D(1)^2}{4k^2} - \frac{D(0).D(2)}{2k^2} + \frac{D(2)^2}{16k^4} \right)^{1/2} \quad (6.3)$$

Hence, the maximum amplitude of the received signal is given by,

$$E_g(\max) = K(f) \left(D(0)^2 + \frac{D(1)^2}{4k^2} - \frac{D(0).D(2)}{2k^2} + \frac{D(2)^2}{16k^4} \right)^{1/2} \quad (6.4)$$

The philosophy behind formulating the forward model in terms of the *maximum* value for the voltage at the receiver, rather than the voltage at the receiver at a *specific* θ *along the wave* is twofold.

Firstly, since one of the basic assumptions of Freedman's model is that the wave is monotonic (single-frequency), it follows that the greater the conformity to this assumption, the greater the accuracy of the model. As no real-world acoustic waves are truly monotonic, the best we can hope for is to select the region of the wave train that is *most* monotonic. A section of the wave with the least variation in amplitude from peak to peak is such a region and this invariably occurs in the central region of the wave. Now, as the maximum value of the wave will also invariably be in the central region, it follows that the maximum value measured is representative of the most monotonic region of the wave train and hence the most accurate. Thus by simply measuring the maximum value, we automatically hone in on the best part of the wave to measure, without having to actually analyse the echo to see where the mid-point is, thereby reducing processing time.

However, the main advantage to focussing only on the maximum value is that it results in multisampling by default. Since our capture card can only sample the wave train once every microsecond, that amounts to only 20 samples per wave cycle, or one sample every 18 degrees, using a 50kHz wave as a typical example. Consequently, the peaks represented in the sampled data may have been sampled a little before or a little after the true peaks on the wave train. However, given several adjacent peaks from the central monotonic region sampled in this way, it's clear that the sampled peak with the highest value will be the one that most closely matched it's counterpart on the wave train. Thus, scanning for the maximum value (ie. the highest peak) in the sampled set has automatically delivered us the most accurately sampled peak as a result.

Turning our attention back to Eq. (6.4), it can be reformulated once again as,

$$\begin{aligned} E_g^2{}_{MAX} &= K(f)^2 \left(D(0)^2 + \frac{D(1)^2}{4k^2} - \frac{D(0).D(2)}{2k^2} + \frac{D(2)^2}{16k^4} \right) \\ &= X_1(f)D(0)^2 + X_2(f)D(1)^2 + X_3(f)D(0).D(2) + X_4(f)D(2)^2 \quad (6.5) \end{aligned}$$

where, $X_1(f) = K(f)^2$,

$$X_2(f) = \frac{K(f)^2}{4k^2},$$

$$X_3(f) = \frac{-K(f)^2}{2k^2},$$

$$X_4(f) = \frac{K(f)^2}{16k^4}$$

Now, we've already established that were we to insonify a stationary object with several frequencies within a short time span, the only *variable* affecting the resulting

echoes would be the frequencies themselves. So let us then examine the echoes that would result if four distinct frequencies were used in this fashion, the square of the maximum voltages at the receiver for each case given below,

$$E_g^2(f_1)_{MAX} = X_1(f_1)D(0)^2 + X_2(f_1)D(1)^2 + X_3(f_1)D(0).D(2) + X_4(f_1)D(2)^2 \quad (6.6)$$

$$E_g^2(f_2)_{MAX} = X_1(f_2)D(0)^2 + X_2(f_2)D(1)^2 + X_3(f_2)D(0).D(2) + X_4(f_2)D(2)^2 \quad (6.7)$$

$$E_g^2(f_3)_{MAX} = X_1(f_3)D(0)^2 + X_2(f_3)D(1)^2 + X_3(f_3)D(0).D(2) + X_4(f_3)D(2)^2 \quad (6.8)$$

$$E_g^2(f_4)_{MAX} = X_1(f_4)D(0)^2 + X_2(f_4)D(1)^2 + X_3(f_4)D(0).D(2) + X_4(f_4)D(2)^2 \quad (6.9)$$

Put into matrix form,

$$\begin{bmatrix} E_g^2(f_1)_{MAX} \\ E_g^2(f_2)_{MAX} \\ E_g^2(f_3)_{MAX} \\ E_g^2(f_4)_{MAX} \end{bmatrix} = \begin{bmatrix} X_1(f_1) & X_2(f_1) & X_3(f_1) & X_4(f_1) \\ X_1(f_2) & X_2(f_2) & X_3(f_2) & X_4(f_2) \\ X_1(f_3) & X_2(f_3) & X_3(f_3) & X_4(f_3) \\ X_1(f_4) & X_2(f_4) & X_3(f_4) & X_4(f_4) \end{bmatrix} \begin{bmatrix} D(0)^2 \\ D(1)^2 \\ D(0).D(2) \\ D(2)^2 \end{bmatrix} \quad (6.10)$$

and taking the inverse of the matrix, we end up with the following,

$$\begin{bmatrix} D(0)^2 \\ D(1)^2 \\ D(0).D(2) \\ D(2)^2 \end{bmatrix} = \begin{bmatrix} X_1(f_1) & X_2(f_1) & X_3(f_1) & X_4(f_1) \\ X_1(f_2) & X_2(f_2) & X_3(f_2) & X_4(f_2) \\ X_1(f_3) & X_2(f_3) & X_3(f_3) & X_4(f_3) \\ X_1(f_4) & X_2(f_4) & X_3(f_4) & X_4(f_4) \end{bmatrix}^{-1} \begin{bmatrix} E_g^2(f_1)_{MAX} \\ E_g^2(f_2)_{MAX} \\ E_g^2(f_3)_{MAX} \\ E_g^2(f_4)_{MAX} \end{bmatrix} \quad (6.11)$$

As we'll see later in section 6.4, a comprehensive representation of the geometry of the scatterer in question requires a knowledge of $D(n)$ for $n=1,2$ & 3. With our current approach, we would need to solve these four simultaneous equations to obtain those. Clearly, we now have a model which, in theory, should allow us to deduce

geometric properties, specifically $D(0)$, $D(1)$ & $D(2)$, of the insonified object from an analysis of the received echo and a knowledge of $X_x(f_y)$. From the definitions of the individual components $X_x(f)$ in Eq. (6.5), we can see that these components are dependent upon the wave number k and $K(f)^2$. As the frequency f in each case is known to us and the speed of sound c is easily calculated from a knowledge of the environmental conditions, which we will have, it follows that wave number k is easily determined for each frequency. This leaves the determination of $K(f)^2$ as the last obstacle before $X_x(f)$ can be calculated for each frequency.

One way to calculate $K(f)^2$ would be to return to the definition of $K(f)$, given in Eq. (6.1), and calculate it's value at each frequency by obtaining values for each of it's constituent components. These components include the sensitivities and directivities of the transducer and receiver, the voltage applied to the transducer, the gain applied to the receiver, the range to the object and the atmospheric absorption coefficient. The main disadvantage of this approach is that the errors, the uncertainties, in each of these values will accumulate when combined into Eq. (6.1). Another approach which has the advantage of being more accurate, as well as faster, is to calibrate the model with an object of precisely known dimensions and thereby determine $K(f)^2$ directly through measurement. Typically, we would want to choose a calibration object that has all $D(n) = 0$, except for one, such as a paraboloid for instance, which has $D(1) \neq 0$, but has discontinuities at all other orders equal to zero. In this case, we would formulate Eq. (6.5) as,

$$E_g^2_{MAX} = K(f)^2 \frac{D(1)^2}{4k^2} \quad (6.12)$$

making the calculation of $K(f)^2$ at each frequency relatively trivial, given that all the other components in this equation are either easily calculated (k), easily measured ($E_{g\ MAX}$) or already known ($D(1)$). Once we have $K(f)^2$ for each frequency, $X_x(f)$ at these frequencies are easily calculated, allowing us to substitute them into Eq. (6.11) and thus determine the discontinuities in the scattering object.

Unfortunately, most of these developments in the time *independent* inverse model become unravelled once some basic assumptions are implemented, which render the model impractical for use in an air environment. Since our forward model has been established as having validity only for smoothly varying objects (ie. objects that do not have discontinuities in $D(0)$, but rather in $D(1)$ and possibly $D(2)$), it follows that our inverse model should reflect this assumption. Assuming $D(0) = 0$, we can significantly simplify Eq. (6.5),

$$E_{g\ MAX}^2 = K(f)^2 \left(\frac{D(1)^2}{4k^2} + \frac{D(2)^2}{16k^4} \right) \quad (6.13)$$

Now, if one considers that in air, the wave number k of the acoustic pulse is of the order of 10^3 , it follows that the second term in the summation in Eq. (6.13) will be 10^6 times smaller than the first term. Needless to say, the sensitivity of our instrumentation is not up to the task of seeing perturbations in the echo on such a small scale. This additional term is therefore dropped as its contribution is negligible. Unfortunately though, what this leaves us with is an inverse model that is stripped down to such an extent that it provides no more insight than one would expect from a simple derivation of the backscatter according to the wave equation,

$$E_{gMAX} = K(f) \frac{D(1)}{2k} \quad (6.14)$$

Even if we were to go out on a limb and consider the possibility that the model *may* have applicability in cases where $D(0) \neq 0$, we ultimately end up in the same predicament. Let's assume $D(0) \neq 0$ and re-examine Eq. (6.5). In air, the second and third terms in the summation will be 10^6 times smaller than the first term and the last term will be a staggering 10^{12} times smaller. Consequently, all terms except the first will have to be dropped as they contribute nothing and we are again left with a result that is comparable to a simple extension of the wave equation,

$$E_{gMAX} = K(f)D(0) \quad (6.15)$$

Finally, there is the issue that the matrix in Eq. (6.10) may be non-invertible because we do not have singular instances of $D(0)$ and $D(2)$ in the simultaneous equations, as their product is repeated in the third term of these equations as $D(0)D(2)$. For instances where the simultaneous equations in question are *non-linear* as is the case here, the correct approach would be to solve it via a *least squares* method. Delving into the methodology of this approach at this point would be redundant however, as the time independent model is clearly unusable for our purposes for the physical reasons listed above. The inevitable conclusion that is drawn from this exercise is that a time *independent* model, whilst having advantages over a time *dependent* model in theory, has possible applicability only in environments where the wave number of the acoustic pulse is much smaller than it is in air, such as water for example, and thus we must turn our attention to an alternate approach.

6.2 Time Dependent Inverse Model

Much of what has been described above with regards to the time *independent* model also applies to the time *dependent* variant. Firstly however, let us return to the point at which the two models diverged, Eq. (6.2) and reformulate it in terms of functions $Y_n(f)$,

$$\begin{aligned} E_g &= K(f) \left(D(0) \sin \theta - \frac{D(1)}{2k} \cos \theta - \frac{D(2)}{4k^2} \sin \theta \right) \\ &= Y_1(f) D(0) + Y_2(f) D(1) + Y_3(f) D(2) \end{aligned} \quad (6.16)$$

where, $Y_1(f) = K(f) \sin \theta$,

$$Y_2(f) = -\frac{K(f)}{2k} \cos \theta,$$

$$Y_3(f) = \frac{-K(f)}{4k^2} \sin \theta,$$

and, $\theta = \omega t - 2kr_g = 2\pi f t - 2kr_g$

As with the time *independent* inverse model, if we postulate a scenario whereby a stationary object is irradiated with several frequencies within a short time span, the only *variable* affecting the resulting echoes will be the frequencies themselves. The only difference between this approach and that taken earlier with the time *independent* model is that we have the added constraint of ensuring that the new variable t , the time index along the wave train where we measure the amplitude of the wave, must remain the same for all frequencies. This provides us with a constant value for t at all

frequencies allowing us to employ the simultaneous equations approach in essentially the same manner as we did earlier. The other difference is that due to the reduced number of terms in Eq. (6.16), we only require our object be insonified with three frequencies instead of four, the voltages at the receiver at time index t for each frequency being given below

$$E_g(f_1) = Y_1(f_1)D(0) + Y_2(f_1)D(1) + Y_3(f_1)D(2) \quad (6.17)$$

$$E_g(f_2) = Y_1(f_2)D(0) + Y_2(f_2)D(1) + Y_3(f_2)D(2) \quad (6.18)$$

$$E_g(f_3) = Y_1(f_3)D(0) + Y_2(f_3)D(1) + Y_3(f_3)D(2) \quad (6.19)$$

Put into matrix form,

$$\begin{bmatrix} E_g(f_1) \\ E_g(f_2) \\ E_g(f_3) \end{bmatrix} = \begin{bmatrix} Y_1(f_1) & Y_2(f_1) & Y_3(f_1) \\ Y_1(f_2) & Y_2(f_2) & Y_3(f_2) \\ Y_1(f_3) & Y_2(f_3) & Y_3(f_3) \end{bmatrix} \begin{bmatrix} D(0) \\ D(1) \\ D(2) \end{bmatrix} \quad (6.20)$$

and taking the inverse of the matrix, we get the following,

$$\begin{bmatrix} D(0) \\ D(1) \\ D(2) \end{bmatrix} = \begin{bmatrix} Y_1(f_1) & Y_2(f_1) & Y_3(f_1) \\ Y_1(f_2) & Y_2(f_2) & Y_3(f_2) \\ Y_1(f_3) & Y_2(f_3) & Y_3(f_3) \end{bmatrix}^{-1} \begin{bmatrix} E_g(f_1) \\ E_g(f_2) \\ E_g(f_3) \end{bmatrix} \quad (6.21)$$

The approach employed for determining the individual component $Y_x(f_y)$ is the same as that described previously for the time *independent* model. As for determining E_g , the only difference is that instead of obtaining the values of E_g from a search for the maximum value of the wave envelope, a point along the wave train at a time index t

is chosen and the amplitude of the wave at this point used instead. Once these values are substituted into Eq. (6.21), predicted values of $D(n)$ can be obtained.

The only disadvantage of this approach is that it lacks the inherent multisampling employed by the method used for the time *independent* model. However, to compensate for the lack of sampling resolution, we employ interpolation algorithms to fit a curve to our sampled data, giving us a greater range of values for t to choose from.

As with the time *independent* variant, the basic constraints on our forward model must be respected and applied to the inverse model as well. Thus we can assume $D(0) = 0$ and modify Eq. (6.16) respectively,

$$E_g(f) = Y_2(f)D(1) + Y_3(f)D(2) \quad (6.22)$$

$$\text{where, } Y_2(f) = -\frac{K(f)}{2k} \cos \theta \quad \& \quad Y_3(f) = \frac{-K(f)}{4k^2} \sin \theta$$

Unlike the situation we faced when we made this assumption for the time *independent* model though, this assumption does not cause us any problems as it does not require us to drop any terms. The reason for this is that, in air, the order of the second term is approximately 10^3 times smaller than the first. Although this is smaller than we'd like for accurate measurement, it is within the range of our instrumentation to measure variations in amplitude on this scale. Thus in conclusion, the time *dependent* inverse model can be represented by the following equation,

$$\begin{bmatrix} D(1) \\ D(2) \end{bmatrix} = \begin{bmatrix} Y_2(f_1) & Y_3(f_1) \\ Y_2(f_2) & Y_3(f_2) \end{bmatrix}^{-1} \begin{bmatrix} E_g(f_1) \\ E_g(f_2) \end{bmatrix} \quad (6.23)$$

on the assumption that $D(0) = 0$.

6.3 Mathematical Validity of the Inversion

To provide reassurance that the algebraic manipulations involved in the inversion were conducted correctly, we will use data gathered when experiments were conducted to test the validity of the inverse model (to be presented later) and plug inverse model predicted values for $D(1)$ and $D(2)$ into the forward model to see whether we obtain the measured echo amplitudes in return. If the model was correctly inverted, then the predictions of the forward model, using these values for $D(1)$ and $D(2)$, should match exactly the echoes measured.

An exponentially shaped scatterer had measured echo amplitudes at a range of 40cm and time index $t=0.002366s$ given by,

$$E(40kHz) = 0.00234$$

$$\text{and } E(60kHz) = 0.0159$$

Also, the calculated values for $K(f)$ were found to be,

$$K(40kHz) = 1.68$$

$$K(60kHz) = 2.85$$

With this data and a knowledge of the environmental conditions, we used the inverse model to calculate the following values for $D(n)$,

$$D(1) = 40.7$$

$$D(2) = 5.85 \times 10^4$$

Now, whether or not these predicted values for $D(1)$ and $D(2)$ agree with the measured values is not of concern to us here, at least not yet. That is an issue for a later chapter when we test the accuracy of the inverse model. What concerns us here is whether the model was correctly inverted and if we input these predicted values for $D(1)$ and $D(2)$ into the forward model it should produce predictions for $E(40kHz)$ and $E(60kHz)$ that exactly match those measured, provided the inversion was done correctly.

Using Eq. (6.22) as the forward model,

$$E_g(f) = -\frac{K(f)}{2k} D(1) \cos \theta - \frac{K(f)}{4k^2} D(2) \sin \theta \quad (6.22)$$

and substituting the above values for $K(f)$, $k = 2\pi f / c$ and the predicted values of $D(1)$ and $D(2)$ into the model at both 40kHz and 60kHz, we indeed find that, as expected, we get,

$$E(40kHz) = 0.00234$$

$$\text{and } E(60kHz) = 0.0159$$

confirming that the inversion is mathematically sound.

6.4 Visualising the Scattering Object

Knowing values for $D(1)$ and $D(2)$ can only hint at the shape of the insonified object. To truly represent the geometry we need to build up a visual representation of

the scattering body using numerical methods. For the sake of generality, we'll examine how this can be done in all cases, not just those for which $D(0) = 0$.

Once $D(0)$, $D(1)$ & $D(2)$ are obtained for each range along the scatterer for which there is an echo, we can build up a picture of the scatterer in the following way. For the front face of the scatterer at a range r_{0-} we have the following equations,

$$D(A,0,0) = A(r_{0-}) - A(r_{0+}) \quad (6.24)$$

$$D(A,0,1) = \frac{dA}{dr}(r_{0-}) - \frac{dA}{dr}(r_{0+}) \quad (6.25)$$

$$D(A,0,2) = \frac{d^2 A}{dr^2}(r_{0-}) - \frac{d^2 A}{dr^2}(r_{0+}) \quad (6.26)$$

Now, $\frac{d^n A}{dr^n}(r_{0-})$ are all zero, since r_{0-} is the range just prior to the front face

where there is no variation in cross sectional area. Hence,

$$\text{Area at } r_{0-} = -D(A,0,0) \quad (6.27)$$

$$\frac{dA}{dr} \text{ at } r_{0-} = -D(A,0,1) \quad (6.28)$$

$$\frac{d^2 A}{dr^2} \text{ at } r_{0-} = -D(A,0,2) \quad (6.29)$$

If we can assume that the second order derivatives remains constant over the range r_{0+} to r_{m-} , where r_m is the range at which the next echo originates, then we can apply the following relations at each successive point within this range,

$$A_{x+1} = A_x + \frac{dA_x}{dr}(r_{x+1} - r_x) \quad (6.30)$$

$$\frac{dA_{x+1}}{dr} = \frac{dA_x}{dr} + \frac{d^2 A_x}{dr^2}(r_{x+1} - r_x) \quad (6.31)$$

Admittedly, assuming a constant second order derivative is a big assumption to make, but without it we cannot progress. However, even if this assumption is incorrect, it allows us to build up an approximation of the object's geometry nonetheless.

Once $A(r_{m-})$ and $\frac{dA}{dr}(r_{m-})$ have been calculated via the above method and assuming $\frac{d^2 A}{dr^2}(r_{m-}) = \frac{d^2 A}{dr^2}(r_{0+})$, we can calculate the area and higher order rates of change at r_m using the following relations,

$$\text{Area at } r_m = A(r_{m-}) - D(A, m, 0) \quad (6.32)$$

$$\frac{dA}{dr} \text{ at } r_m = \frac{dA}{dr}(r_{m-}) - D(A, m, 1) \quad (6.33)$$

$$\frac{d^2 A}{dr^2} \text{ at } r_m = \frac{d^2 A}{dr^2}(r_{m-}) - D(A, m, 2) \quad (6.34)$$

This process is continued for all ranges at which echoes originate and thereby the shape of the scatterer, or at least an approximation thereof, is reconstructed.

In the next chapter we will examine how we intend to go about verifying the inverse model developed in this section.

7 Geometric Analysis of Scattering Bodies

To test the validity of the inverse model, we firstly needed to obtain a series of objects, for use as scattering bodies that have physical characteristics satisfying the assumptions of the model. Specifically, objects which have smoothly varying surfaces, no possibility of internal penetration by the ultrasonic wave and a separation between discontinuity points on the object such that no wave overlap from echoes would occur. To accomplish this, we obtained a range of solid aluminium objects with geometrically simple designs. The choice of which objects to use was rather arbitrary, the only criteria being that they represent a broad spectrum of possible objects that would fit the description of being smoothly varying and radially symmetric. Thus, despite the fact that we chose to use two paraboloids, we could just as easily have used two spheroids with the same justification. The choices were arbitrary.

These were machine turned to precise dimensions, imperfections in the final product from this process were quoted as being under 0.2mm, well under the limit required by the Raleigh criterion.

7.1 Exponentially Shaped Scatterer

The first object has a length increasing exponentially with width, which could conversely be described as a width expanding logarithmically with length. It has a length of 10 cm and a cross-sectional area which varied from zero at its vertex to 30.2 cm squared at its base. Its geometry was governed by Eq. (7.1) below,

$$x(r) = \exp\left(\frac{r^2}{4}\right) - 1 \quad (7.1)$$

where $x(r)$ = the length (cm) along the axis, measured from the vertex

and r = the radius of the cross-sectional area of the object.

As Freedman's model is focussed on the variation of cross-sectional area with range, it's more appropriate for us to express the above equation with the cross-sectional radius being a function of range, rather than the converse. Thus we have Eq. (7.2),

$$r(x) = \sqrt{4 \ln(x+1)} \quad (7.2)$$

The geometry of this object is represented in Fig. 7.1 below, where the axes are in units of cm. Despite the hollow appearance of the rendered image below, the objects used were solid throughout.

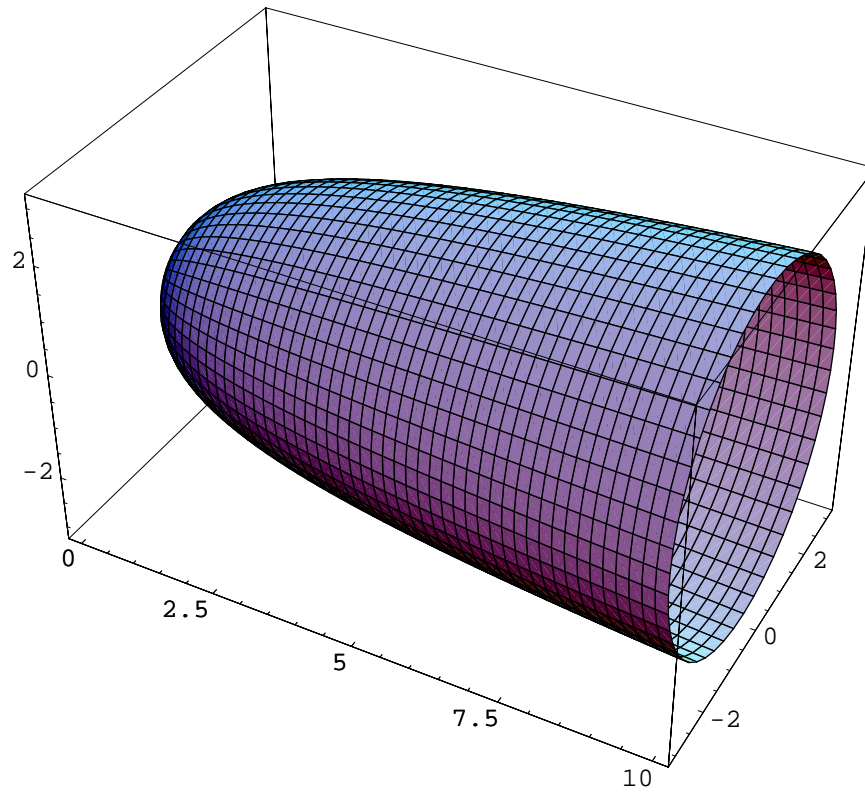


FIG. 7.1. Representation of an aluminium object with the geometry governed by Eq. (7.1).

A more useful visual representation of the structure of the object comes from a plot of the variation of the cross-sectional area with respect to range in Fig. 7.2 below,

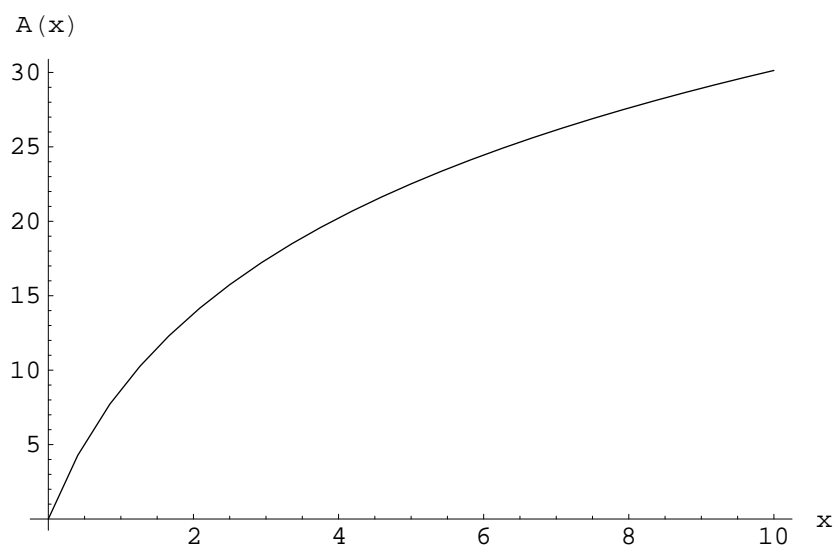


FIG. 7.2. Plot of cross-sectional area (square cm) with respect to range (cm) for the object in Fig. 7.1.

As can be seen from Fig. 7.2, the cross-sectional area varies smoothly with range. We can therefore make a qualitative judgement at this stage that we would *not* expect to see any image pulses (ie. echoes) originating from any points along the length of the object (ie. in the range $0 \text{ cm} < x < 10 \text{ cm}$).

The cross-sectional area plot shown in the figure above is governed by Eq. (7.3) below,

$$A(x) = 4\pi \ln(x+1) \quad (7.3)$$

where $A(x)$ = the cross-sectional area of the object at range x .

The derivative of the equation above with respect to range yields the following,

$$\frac{dA(x)}{dx} = \frac{4\pi}{1+x} \quad (7.4)$$

that we've plotted in Fig. 7.3 below,

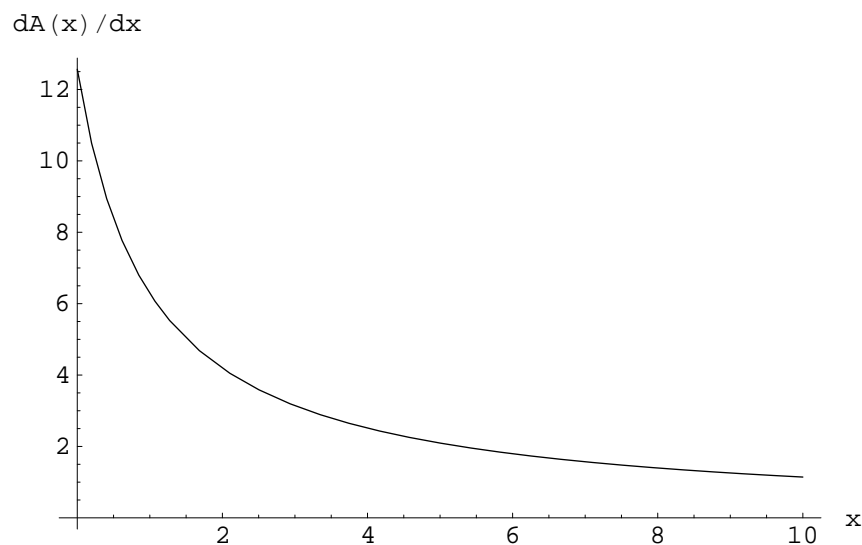


FIG. 7.3. Derivative of the cross-sectional area with respect to range (cm) of the object in Fig. 7.1.

Taking the derivative of Eq. (7.4) gives us the second order derivative in Eq. (7.5) below,

$$\frac{d^2 A(x)}{dx^2} = \frac{-4\pi}{(1+x)^2} \quad (7.5)$$

that is represented in Fig. 7.4,

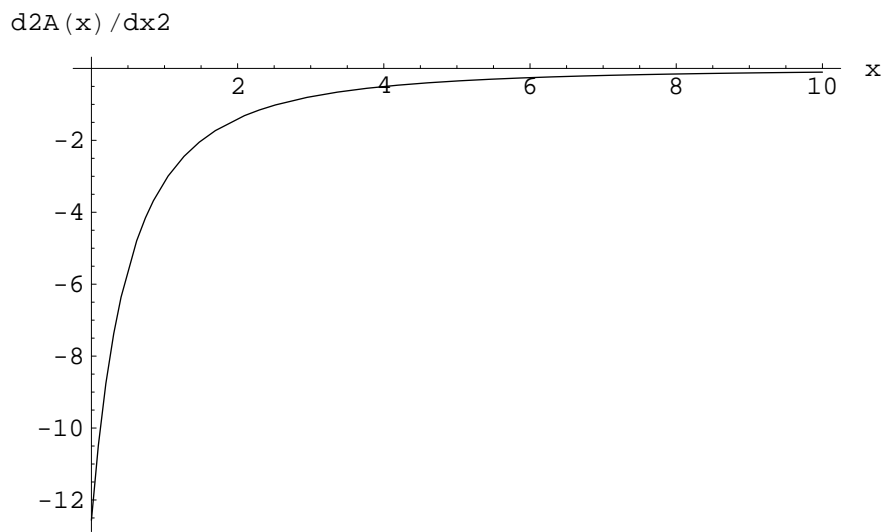


FIG. 7.4. 2nd order derivative of cross-sectional area with respect to range (cm) of object in Fig. 7.1.

Now that we have the derivatives calculated, it's quite clear from Figs. 7.2, 7.3 & 7.4 that these are all *continuous* functions, which is to say that there are no step discontinuities in Eqs. (7.3), (7.4) & (7.5) in the range $0 \text{ cm} < x < 10 \text{ cm}$ and hence no echoes from this region. At $x = 0 \text{ cm}$ however, there is a transition between the free space prior to the object, where the cross-sectional area (and it's higher order derivatives) are null, and the start of the object itself. To determine whether this transition between the two cross-sectional profiles would result in step discontinuities (and echoes) at this point, or not, we can look once again at the plots shown in Figs. 7.2, 7.3 & 7.4.

Inspection of Fig. 7.2 reveals a cross-sectional area along the object that has a value of zero at $x = 0$ cm. Because the size of the cross-sectional area at $x = 0$ cm is the same for the free space region as it is for the object itself, namely zero, there is no discontinuity in cross-sectional area at this point and hence this factor does not contribute to an echo. To express this quantitatively, let's begin with Eq. (2.16) below,

$$D(A_w, g, n) = \frac{d^n A_w}{dr^n}(r_{g-}) - \frac{d^n A_w}{dr^n}(r_{g+}) \quad (2.16)$$

where r_{g-} and r_{g+} represent the ranges infinitesimally prior to and beyond the discontinuity respectively.

In this instance, we are dealing with the case where $n = 0$ and $g = 0$ cm. Thus, we have Eq. (7.6),

$$D(A_w, 0, 0) = A_w(r_{0-}) - A_w(r_{0+}) \quad (7.6)$$

Since $A_w(r_{0-})$ represents the cross-sectional area in the free space immediately prior to the start of the object, it is necessarily equal to zero. As for $A_w(r_{0+})$, we can see from Fig. 7.2 that at a point infinitesimally beyond $x = 0$ cm, the cross-sectional area remains zero. Since these quantities are equal (zero), Eq. (7.6) has a value of zero, indicating that there is no discontinuity in the cross-sectional area profile at this point and thus this factor would not contribute to any echoes.

Turning our attention to the higher order derivatives, we examine Fig. 7.3 next. At $x = 0$ cm, the derivative of the cross-sectional area with respect to range has a value

of 4π . Given that we've already established that the free space region prior the the scatterer has a cross-sectional profile equal to zero, at all orders, it follows that the transition at $x = 0$ cm from a cross-sectional area of zero to 4π must result in a step discontinuity. Expressed in terms of the discontinuity equation.

$$\begin{aligned}
 D(A_w, 0, 1) &= \frac{dA_w}{dr}(r_{0-}) - \frac{dA_w}{dr}(r_{0+}) & (7.7) \\
 &= (0) - (4\pi). \\
 &= -4\pi
 \end{aligned}$$

Thus at $x = 0$ cm, there *is* a contribution to the echo as a result of the discontinuity in the profile of the derivative of the cross-sectional area with respect to range.

Finally, in Fig. 7.4 we can see that the second order derivative of cross-sectional area with respect to range has a value of -4π at the transition point $x = 0$ cm. For the reasons outlined above, there is therefore a step discontinuity at this point. In terms of the discontinuity equation,

$$\begin{aligned}
 D(A_w, 0, 2) &= \frac{d^2 A_w}{dr^2}(r_{0-}) - \frac{d^2 A_w}{dr^2}(r_{0+}) & (7.8) \\
 &= 0 - (-4\pi) \\
 &= 4\pi
 \end{aligned}$$

Therefore there is also a contribution to the echo originating at $x = 0$ cm from the discontinuity in the second order derivative of cross-sectional area with respect to range. Despite the magnitude of the discontinuity being the same in both cases, 4π , the size of the contribution of each component to the total echo will differ however. This is due to

Freedman's equation weighting successively higher order discontinuities several orders of magnitude lower than their predecessors.

Of course, since this object, and indeed all our objects, have a sharp edge at their base, the transition point between the insonified and shadow regions, we would also expect echoes from that region. But as was pointed out earlier, our model does not handle such discontinuities correctly and so we limit ourselves to the echoes that originate at those points on the scatterer where the surface is smoothly varying, regions which our model handles well. Since the echoes from the base are separate from the front face echoes in the time domain, there is no cross contamination and we can effectively ignore the base echoes.

Thus in summary, the exponentially shaped object has a geometry with discontinuities in the first and second order derivatives of the cross-sectional area with respect to range at the position $x = 0$ cm. These are summarised in the table below,

Location of D(n)	D(0)	D(1)	D(2)
0 cm	0	-4π	4π

Table 7.1. Discontinuities on the exponentially shaped object.

7.2 Paraboloid A

The next object has a parabolic shape governed by the following equation,

$$r(x) = \sqrt{\frac{12x}{5}} \quad (7.9)$$

where $r(x)$ = the radius of the cross-sectional area of the object at range x

It has a length of 10 cm with its cross-sectional area varying from zero at it's vertex to 75.4 cm squared at it's base. Its geometry is shown in Fig. 7.5 below,

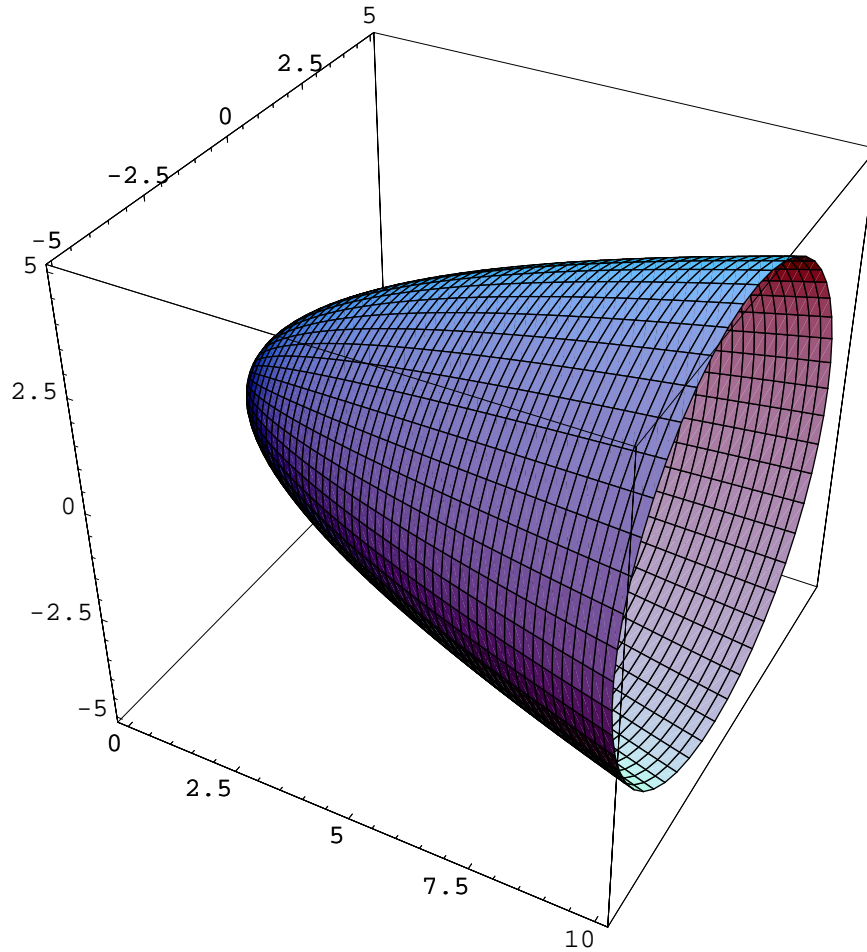


FIG. 7.5. Representation of an aluminium object with the geometry governed by Eq. (7.9).

The cross-sectional area of the figure above is given by Eq. (7.10) below,

$$A(x) = \frac{12\pi x}{5} \quad (7.10)$$

This is represented in Fig. 7.6 below,

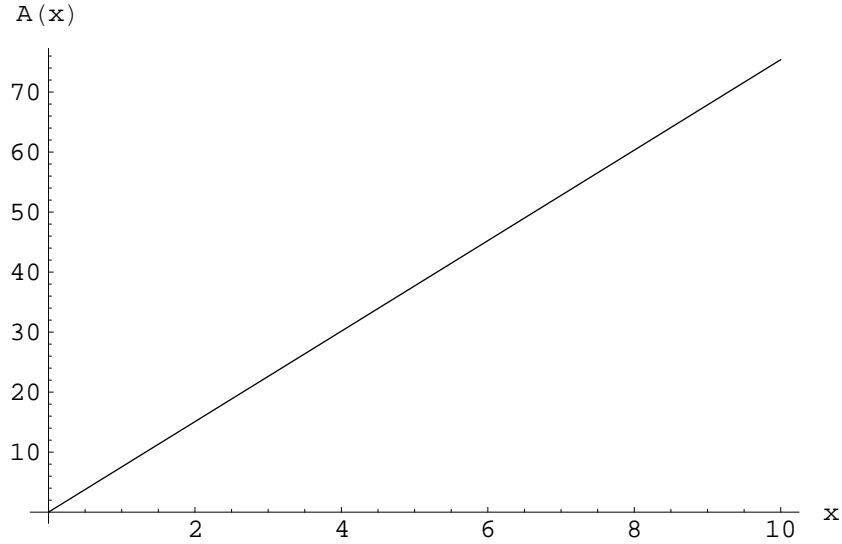


FIG. 7.6. Plot of cross-sectional area (square cm) with respect to range (cm) for the object in Fig. 7.5.

Given the continuous nature of Eq. (7.10), seen clearly in Fig. 7.6, it is expected that no step discontinuities would be present along the length of the object and hence no echoes in the range $0 < x < 10$ cm.

The derivative of the cross-sectional area with respect to range of Eq. (7.10) is given by Eq. (7.11) below,

$$\frac{dA(x)}{dx} = \frac{12\pi}{5} \quad (7.11)$$

A constant value for all in the range $0 \text{ cm} < x < 10 \text{ cm}$, which immediately implies that the second order derivative with respect to range will be zero in the same region,

$$\frac{d^2 A(x)}{dx^2} = 0 \quad (7.12)$$

As before, since the cross-sectional area and it's higher order derivatives with respect to range are continuous along the length of the scatterer, the only region where a Freedman image pulse may originate remains the transition point between the two cross sectional profiles at $x = 0$ cm.

As Eq. (7.10) and Fig 7.6 clearly demonstrate, the cross-sectional area at a point infinitesimally beyond $x = 0$ cm remains zero. As this is equivalent to the null cross-sectional area of the free space infinitesimally prior to $x = 0$ cm, it follows that there is no difference in the cross-sectional profiles, hence no discontinuity and thus no echo from this component. In terms of the discontinuity equation,

$$\begin{aligned} D(A_w, 0, 0) &= A_w(r_{0-}) - A_w(r_{0+}) \\ &= (0) - (0) \end{aligned} \tag{7.13}$$

However, as Eq. (7.11) shows, the derivative of the cross-sectional area with respect to range is $\frac{12\pi}{5}$ at all ranges including $x = 0$ cm. Given that the free space region prior to the scatter has a value of zero, it's clear that this represents a sudden change in the profile of $\frac{dA(x)}{dx}$ at $x = 0$ cm. This step discontinuity is shown in Eq. (7.14),

$$\begin{aligned} D(A_w, 0, 1) &= \frac{dA_w}{dr}(r_{0-}) - \frac{dA_w}{dr}(r_{0+}) \\ &= (0) - \left(\frac{12\pi}{5}\right). \\ &= -\frac{12\pi}{5} \end{aligned} \tag{7.14}$$

It follows that this step discontinuity will be responsible for the production of an image pulse (echo) at this point.

Finally, since the second order derivative with respect to range has been established as being zero at $x = 0$ cm, there is no change in the profile of $\frac{d^2 A(x)}{dx^2}$ at this point and thus there is no discontinuity to concern us.

$$D(A_w, 0, 2) = \frac{d^2 A_w}{dr^2}(r_{0-}) - \frac{d^2 A_w}{dr^2}(r_{0+}) \quad (7.15)$$

$$= (0) - (0)$$

In summary, the first parabolic object has a discontinuity in the first order derivative of the cross-sectional area with respect to range at $x = 0$ cm. These are summarised in the table below,

Location of D(n)	D(0)	D(1)	D(2)
0 cm	0	- 2.4 π	0

Table 7.2. Discontinuities on the first parabolic object.

7.3 Spheroid-Paraboloid

The next object is a merger between a half-sphere and a paraboloid. It's geometry is dictated by the following equation,

$$r(x) = \sqrt{20x - x^2} \quad , 0 \leq x \leq 5 \text{ cm} \quad (7.16)$$

$$= \sqrt{7.05(x + 5.64)} \quad , 5 < x \leq 10 \text{ cm}$$

where $r(x)$ = the radius of the cross-sectional area of the object at range x

It's length is 10 cm with it's cross-sectional area varying from zero at it's vertex to 346.4 cm squared at it's base. Its geometry is shown in Fig. 7.7 below,

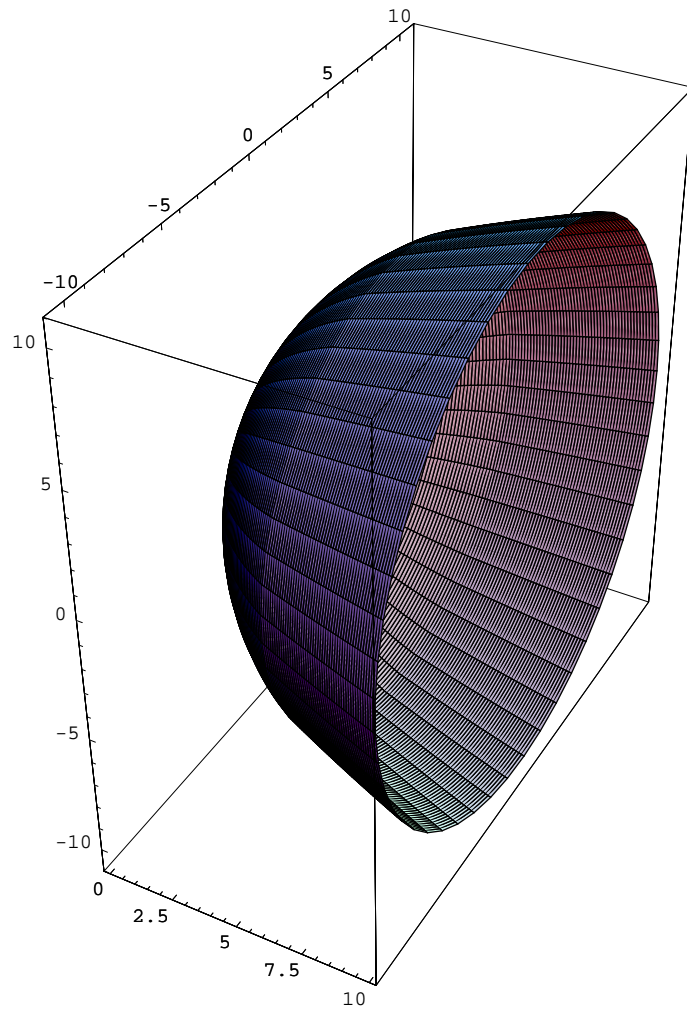


FIG. 7.7. Representation of an aluminium object with the geometry governed by Eq. (7.16)

The cross-sectional area of Fig. 7.7 above is given by Eq. (7.17) below,

$$\begin{aligned}
 A(x) &= 20\pi x - \pi x^2 & , 0 \leq x \leq 5 \text{ cm} \\
 &= 7.05\pi(x + 5.64) & , 5 < x \leq 10 \text{ cm}
 \end{aligned}
 \tag{7.17}$$

This is represented in Fig. 7.8 below,

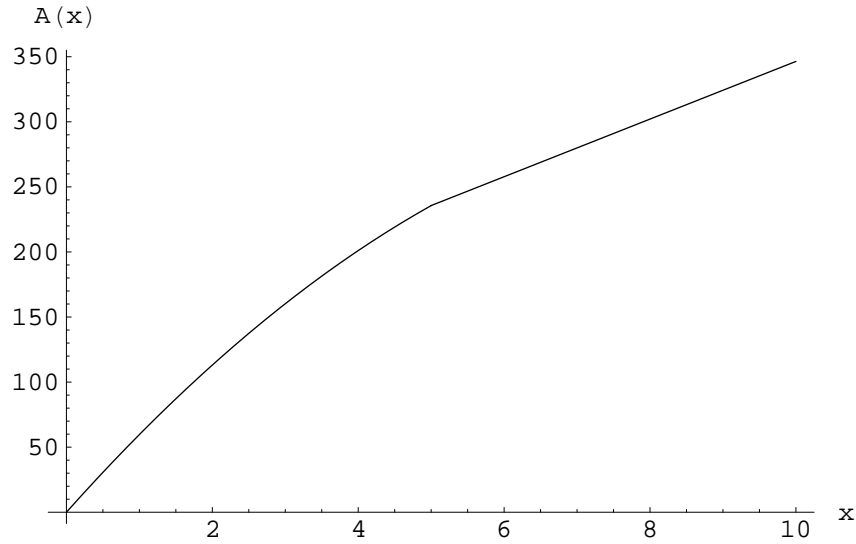


FIG. 7.8. Plot of cross-sectional area (square cm) with respect to range (cm) for the object in Fig. 7.7.

This object's cross-sectional area profile differs from the others encountered thus far in that there is a 'kink' in the cross-sectional area at $x = 5$ cm. This is of course due to the fact that the object is constructed from differently shaped objects, the half-sphere and the paraboloid, and this 'kink' in the profile occurs at the point of intersection of these two disparate shapes. Although the cross-sectional area profile clearly remains continuous, the change in the slope of the curve shown above indicates that we'd expect the higher order derivatives of cross-sectional area with respect to range to possibly exhibit discontinuities and thus result in image pulses from this range ($x = 5$ cm). This is by design of course, as we'd like to see whether it's feasible, via inverse analysis, to resolve the shapes of objects with geometries that exhibit sudden changes in curvature along their length.

The derivative of the cross-sectional area with respect to range of Eq. (7.17) is given by Eq. (7.18) below,

$$\begin{aligned}\frac{dA(x)}{dx} &= 20\pi - 2\pi x & , 0 \leq x \leq 5 \text{ cm} & \quad (7.18) \\ &= 7.05\pi & , 5 < x \leq 10 \text{ cm}\end{aligned}$$

The plot of Eq. (7.18) is shown in Fig. 7.9 below,

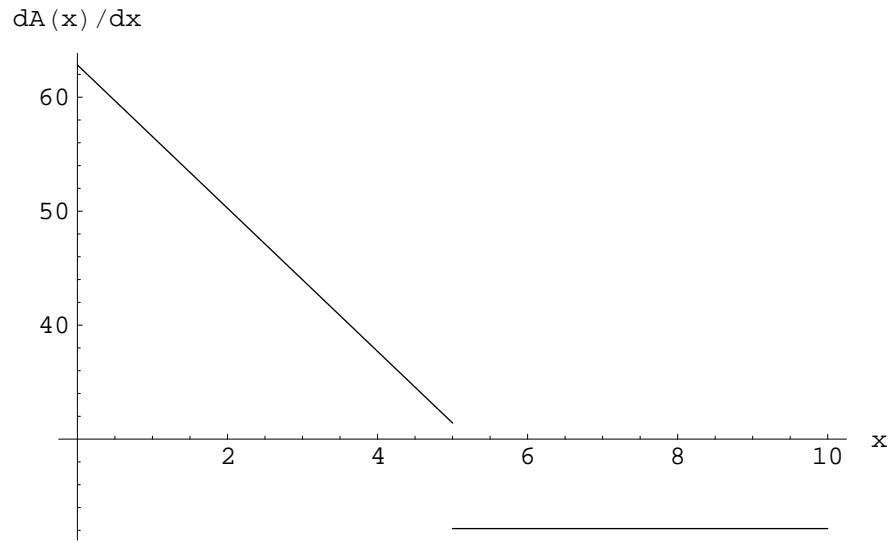


FIG. 7.9. Derivative of the cross-sectional area with respect to range (cm) of the object in Fig. 7.7.

As we suspected earlier, the change in surface curvature at $x = 5$ cm has resulted in a distinct discontinuity in the derivative of the cross-sectional area at this range, thus this component will result in an image pulse at that point. We'll calculate the exact size of this discontinuity shortly.

Lastly, the second order derivative of the cross-sectional area with respect to range is given below in Eq. (7.19),

$$\begin{aligned}\frac{d^2 A(x)}{dx^2} &= -2\pi & , 0 \leq x \leq 5 \text{ cm} & \quad (7.19) \\ &= 0 & , 5 < x \leq 10 \text{ cm}\end{aligned}$$

One does not need a plot of Eq. (7.19) to see that at $x = 5$ cm there is a discontinuity of magnitude 2π , which will add a second contribution to the already established image pulse from this range.

We'll turn our attention now to calculating the values for these discontinuities for both those at $x = 5$ cm as well as those that are inevitably to be expected from $x = 0$ cm as per usual. For the cross-sectional area, the discontinuity equations for both ranges, $x = 0$ cm and $x = 5$ cm respectively, can be expressed by the following equations,

$$\begin{aligned} D(A_w, 0, 0) &= A_w(r_{0-}) - A_w(r_{0+}) \\ &= (0) - (0) \end{aligned} \tag{7.20}$$

$$\begin{aligned} D(A_w, 5, 0) &= A_w(r_{5-}) - A_w(r_{5+}) \\ &= (75\pi) - (75\pi) \\ &= 0 \end{aligned} \tag{7.21}$$

Eq. (7.20) verifies what we've already established via observation of Fig.7.8, that there are no discontinuities in the cross-sectional area profile at $x = 5$ cm. It also reveals that at the transition point $x = 0$ cm, there are no discontinuities either.

For the derivative of the cross-sectional area with respect to range, the discontinuity equations for both ranges are given below,

$$\begin{aligned} D(A_w, 0, 1) &= \frac{dA_w}{dr}(r_{0-}) - \frac{dA_w}{dr}(r_{0+}) \\ &= (0) - (20\pi) \\ &= -20\pi \end{aligned} \tag{7.22}$$

$$\begin{aligned}
D(A_w, 5, 1) &= \frac{dA_w}{dr}(r_{5-}) - \frac{dA_w}{dr}(r_{5+}) \\
&= (10\pi) - (7.05\pi). \\
&= 2.95\pi
\end{aligned} \tag{7.23}$$

Clearly then, at both ranges there are discontinuities in the derivative of the cross-sectional area profile with respect to range and hence we'll expect image pulses to originate from these ranges after insonification.

Finally, for the second order derivative of the cross-sectional area with respect to range, the discontinuity equations are,

$$\begin{aligned}
D(A_w, 0, 2) &= \frac{d^2 A_w}{dr^2}(r_{0-}) - \frac{d^2 A_w}{dr^2}(r_{0+}) \\
&= (0) - (-2\pi). \\
&= 2\pi
\end{aligned} \tag{7.24}$$

$$\begin{aligned}
D(A_w, 5, 2) &= \frac{d^2 A_w}{dr^2}(r_{5-}) - \frac{d^2 A_w}{dr^2}(r_{5+}) \\
&= (-2\pi) - (0). \\
&= -2\pi
\end{aligned} \tag{7.25}$$

Again, at both ranges there are discontinuities. However, given that we've already established that there will be echoes from the ranges $x = 0$ cm and $x = 5$ cm as a result of discontinuities in the first order derivative of the cross-sectional area profile with respect to range, the echoes that result from discontinuities in the second order will be several orders of magnitude smaller.

To summarise our observations, the spheroid-paraboloid has discontinuities in both the first and second order derivatives of the cross-sectional area with respect to range at ranges of $x = 0$ cm and $x = 5$ cm. These are summarised in the table below,

Location of D(n)	D(0)	D(1)	D(2)
0 cm	0	-20π	2π
5 cm	0	2.95π	-2π

Table 7.3. Discontinuities on the spheroid-paraboloid.

7.4 Paraboloid B

The next object in the series is another paraboloid, though this time with a broader base. It's geometry is governed by the following equation,

$$r(x) = \sqrt{4.9x} \quad (7.26)$$

where $r(x)$ = the radius of the cross-sectional area of the object at range x

It has a length of 10 cm with it's cross-sectional area varying from zero at it's vertex to 153.9 cm squared at it's base. It's geometry is shown in Fig. 7.10 below,

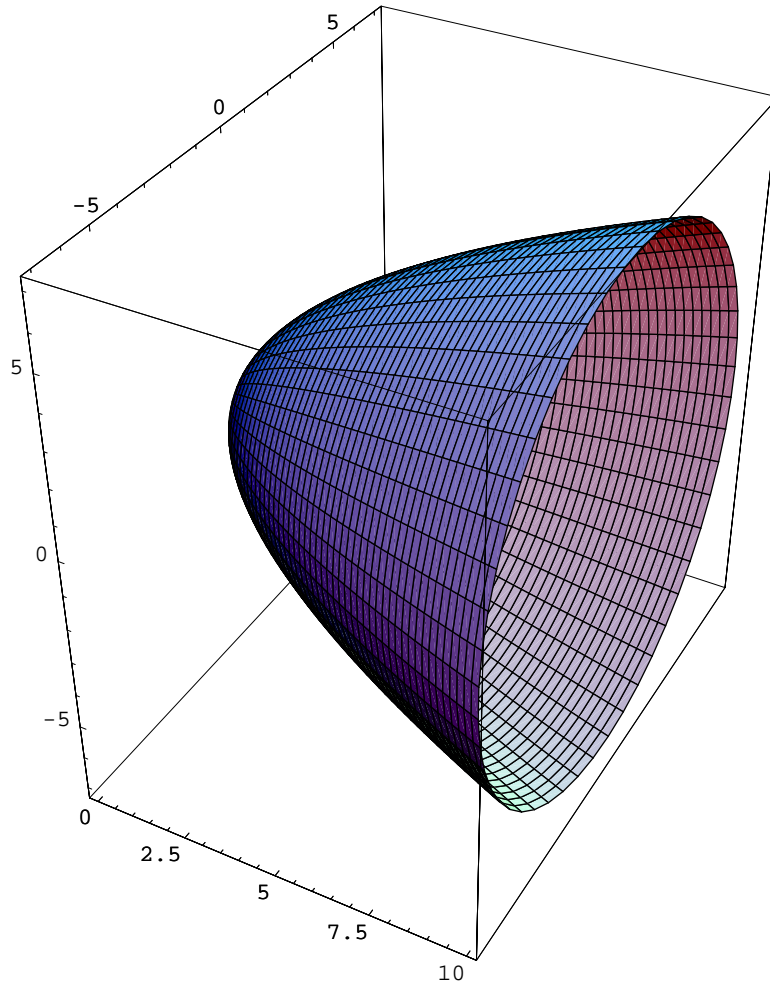


FIG. 7.10. Representation of an aluminium object with the geometry governed by Eq. (7.26).

The cross-sectional area of the figure above is given by Eq. (7.10) below,

$$A(x) = 4.9\pi x \quad (7.27)$$

This is represented in Fig. 7.11 below,

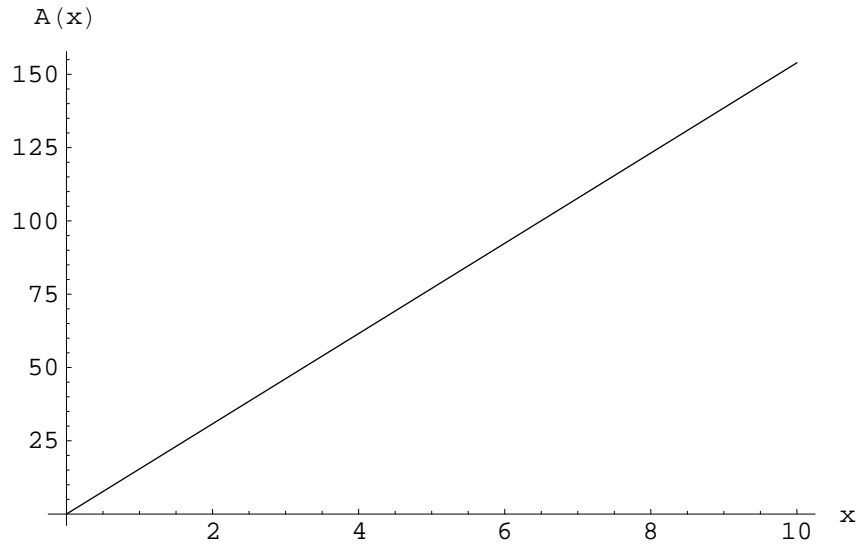


FIG. 7.11. Plot of cross-sectional area (square cm) with respect to range (cm) for object in Fig. 7.10.

As with the first paraboloid, the continuous nature of Eq. (7.27) leads us to believe that no step discontinuities would be present along the object's length and thus no echoes in the range $0 < x < 10$ cm.

The derivative of the cross-sectional area with respect to range of Eq. (7.27) is given by Eq. (7.28) below,

$$\frac{dA(x)}{dx} = 4.9\pi \quad (7.28)$$

A constant value for all in the range $0 \text{ cm} < x < 10 \text{ cm}$, which again immediately implies that the second order derivative with respect to range will be zero in the same region,

$$\frac{d^2 A(x)}{dx^2} = 0 \quad (7.29)$$

As with the previous paraboloid, since the cross-sectional area and its higher order derivatives with respect to range are continuous along the length of the scatterer,

the only region where a Freedman image pulse may originate remains the transition point between the two cross sectional profiles at $x = 0$ cm.

For the cross-sectional area, the discontinuity equation is,

$$\begin{aligned} D(A_w, 0, 0) &= A_w(r_{0-}) - A_w(r_{0+}) \\ &= (0) - (0) \end{aligned} \tag{7.30}$$

Indicating no discontinuity in the cross-sectional area profile at this point.

As for the derivative of the cross-sectional area with respect to range, the discontinuity equation is thus,

$$\begin{aligned} D(A_w, 0, 1) &= \frac{dA_w}{dr}(r_{0-}) - \frac{dA_w}{dr}(r_{0+}) \\ &= (0) - (4.9\pi) \\ &= -4.9\pi \end{aligned} \tag{7.31}$$

It follows that this step discontinuity will be responsible for the production of an image pulse (echo) at this point, should the object become insonified.

Lastly, since the second order derivative with respect to range has been established as being zero at $x = 0$ cm, then as with the first parabola before it, there is no change in the profile of $\frac{d^2 A(x)}{dx^2}$ at this point and thus there is no discontinuity to concern us.

$$\begin{aligned} D(A_w, 0, 2) &= \frac{d^2 A_w}{dr^2}(r_{0-}) - \frac{d^2 A_w}{dr^2}(r_{0+}) \\ &= (0) - (0) \end{aligned} \tag{7.32}$$

Thus in summary, the second parabolic object has only one discontinuity, this being in the first order derivative of the cross-sectional area with respect to range at $x = 0$ cm.

These are summarised in the table below,

Location of D(n)	D(0)	D(1)	D(2)
0 cm	0	- 4.9π	0

Table 7.4. Discontinuities on the second parabolic object.

7.5 Ellipsoid

The fifth object has an elliptical shape governed by the following,

$$r(x) = \sqrt{4x(10 - x)} \quad (7.33)$$

where $r(x)$ = the radius of the cross-sectional area of the ellipsoid at range x

Its length is only 5 cm and its cross-sectional area varies from zero at it's vertex to 314.2 cm squared at it's base. Its geometry is shown in Fig. 7.12 below,

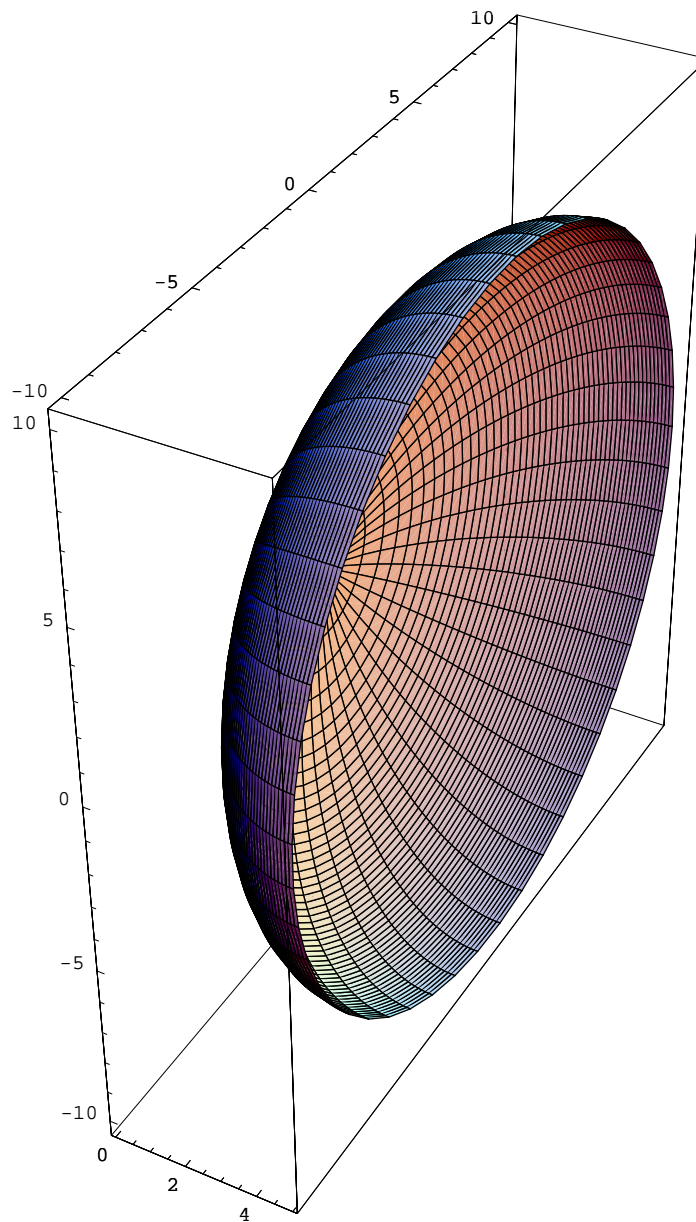


FIG. 7.12. Representation of the aluminium object with the geometry governed by Eq. (7.33).

The cross-sectional area of the figure above is given by Eq. (7.34) below,

$$A(x) = 4\pi x(10 - x) \quad (7.34)$$

This is represented in Fig. 7.13 below,

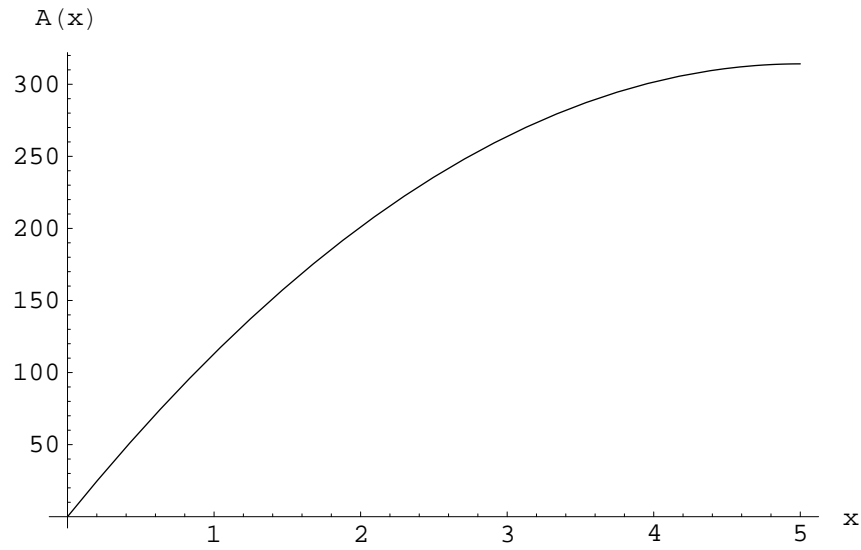


FIG. 7.13. Plot of cross-sectional area (square cm) with respect to range (cm) for object in Fig. 7.12.

Given the continuous nature of Eq. (7.34), seen clearly in Fig. 7.13, it is expected that no step discontinuities would be present along the length of the object and hence no echoes in the range $0 < x < 10$ cm.

The derivative of the cross-sectional area with respect to range of Eq. (7.34) is given by Eq. (7.35) below,

$$\frac{dA(x)}{dx} = 4\pi(10 - 2x) \quad (7.35)$$

This is plotted in Fig. 7.14 below,



FIG. 7.14. Derivative of cross-sectional area (square cm) with respect to range for object in Fig. 7.12.

Clearly, the linearity of the above plot bears out our prediction of continuity in the derivative of the cross-sectional area with respect to range. The linearity also indicates that the second order derivative will be constant. Indeed, this is shown to be true in Eq. (7.36) below,

$$\frac{d^2 A(x)}{dx^2} = -8\pi \quad (7.36)$$

Thus, as before, since the cross-sectional area and its higher order derivatives with respect to range are continuous along the length of the scatterer, the only region where a Freedman image pulse may originate remains the transition point between the two cross sectional profiles at $x = 0$ cm. For the cross-sectional area, where there is no change in the cross-sectional profile at $x = 0$ cm, since both the object at this point and the free space region have cross-sectional areas of zero, the discontinuity equation is given below,

$$\begin{aligned} D(A_w, 0, 0) &= A_w(r_{0-}) - A_w(r_{0+}) \\ &= (0) - (0) \end{aligned} \quad (7.37)$$

Hence this component will not produce an image pulse when insonified.

The derivative of the cross-sectional area with respect to range does not begin with a value of zero at $x = 0$ cm though. Thus, we'll expect a discontinuity at this point as can be seen by the discontinuity equation below,

$$\begin{aligned}
 D(A_w, 0, 1) &= \frac{dA_w}{dr}(r_{0-}) - \frac{dA_w}{dr}(r_{0+}) \\
 &= (0) - (40\pi) \\
 &= -40\pi
 \end{aligned} \tag{7.38}$$

It follows that this step discontinuity will be responsible for the production of an echo at this point when irradiated with an acoustic wave.

Finally, since the second order derivative with respect to range has been established as being non-zero at $x = 0$ cm, there will be a sudden change in the profile of

$\frac{d^2 A(x)}{dx^2}$ at this point and thus a discontinuity will result, as shown below,

$$\begin{aligned}
 D(A_w, 0, 2) &= \frac{d^2 A_w}{dr^2}(r_{0-}) - \frac{d^2 A_w}{dr^2}(r_{0+}) \\
 &= (0) - (-8\pi) \\
 &= 8\pi
 \end{aligned} \tag{7.39}$$

In summary then, the ellipsoid object has discontinuities in the first and second order derivatives of the cross-sectional area with respect to range at the range $x = 0$ cm. These are summarised in the table below,

Location of D(n)	D(0)	D(1)	D(2)
0 cm	0	- 40 π	8 π

Table 7.5. Discontinuities on the ellipsoid.

7.6 Fourth Order Shaped Object

The last object in our series has what can only be described as a “4th order” geometry, so called because it’s shape is governed by the following equation,

$$x(r) = \frac{r^4}{98.3} \quad (7.40)$$

where $x(r)$ = the length (cm) along the axis, measured from the vertex.

In keeping with our decision to express the cross-sectional parameters of our objects in terms of range, we can reformulate this as,

$$r(x) = 3.15x^{1/4} \quad (7.41)$$

This object has a length of 10 cm with its cross-sectional area varying from zero at its vertex to 98.5 cm squared at it’s base. Its geometry is shown in Fig. 7.15,

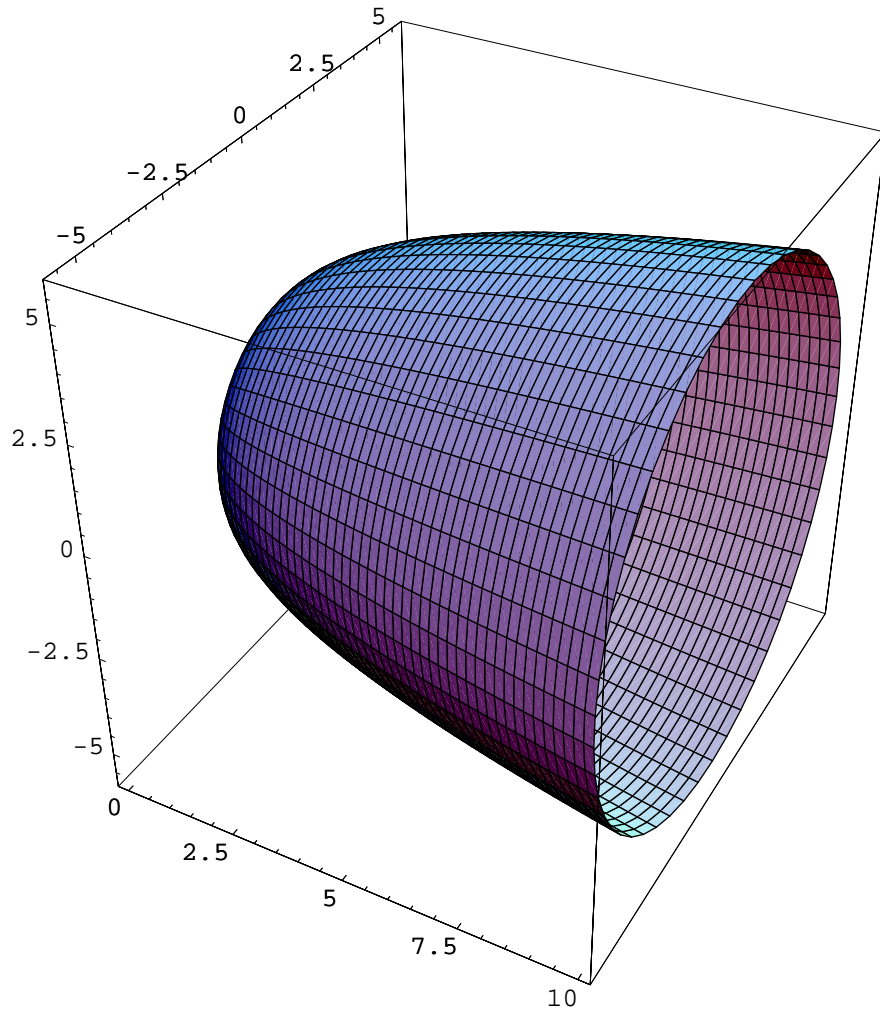


FIG. 7.15. Representation of an aluminium object with the geometry governed by Eq. (7.41).

The cross-sectional area of the figure above is given by Eq. (7.42) below,

$$A(x) = 9.92\pi x^{1/2} \quad (7.42)$$

This is represented in Fig. 7.16 below,

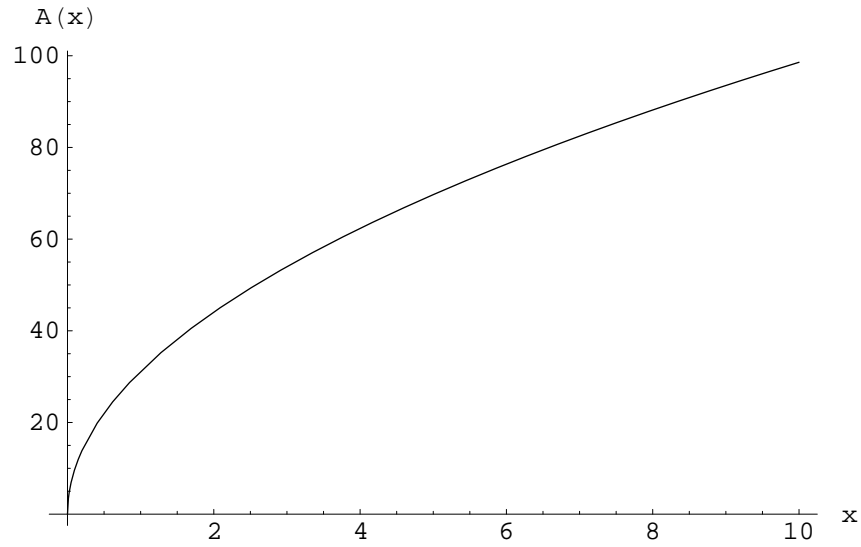


FIG. 7.16. Plot of cross-sectional area (square cm) with respect to range (cm) for object in Fig. 7.15.

This is another example of an object with a continuous cross-sectional area, leading us to expect that no step discontinuities would be present along the length of the object.

The derivative of the cross-sectional area with respect to range, is given by Eq. (7.43) below,

$$\frac{dA(x)}{dx} = 4.96\pi x^{-1/2} \quad (7.43)$$

This is shown in Fig. 7.17,

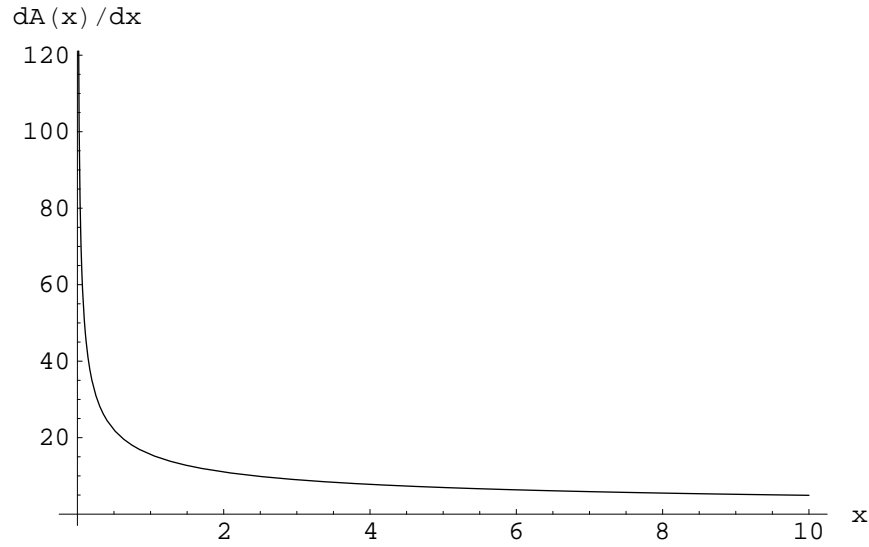


FIG. 7.17. Derivative of cross-sectional area (square cm) with respect to range for object in Fig. 7.15.

As with the cross-sectional area profile, the plot is continuous, indicating no discontinuities along the length of the object (ie. $x > 0$ cm). Of note however is the nature of the curve to approach infinity as it nears zero, which should have interesting implications for the expected discontinuity at $x = 0$ cm.

As for the second order derivative of the cross-sectional area with respect to range, it's governed by,

$$\frac{d^2 A(x)}{dx^2} = -2.48\pi x^{-3/2} \quad (7.44)$$

shown in Fig. 7.18 below,

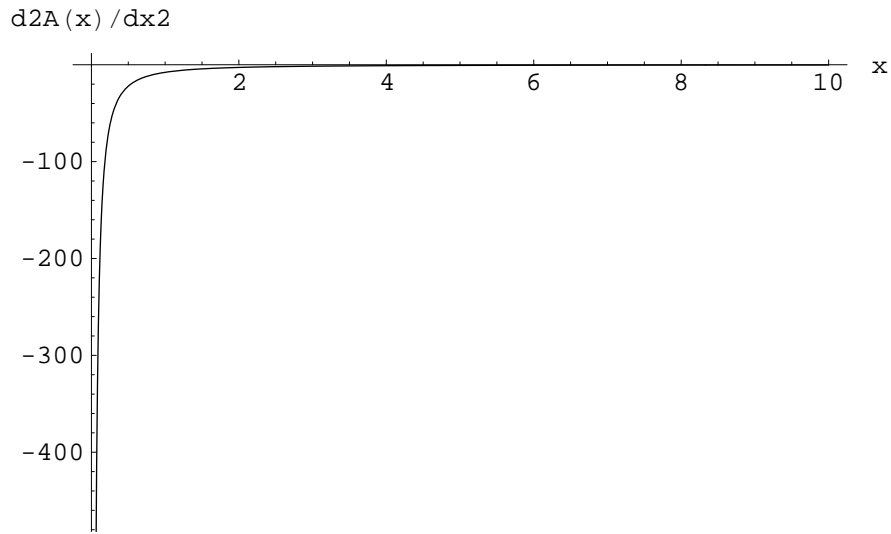


FIG. 7.18. 2nd order derivative of cross-sectional area with respect to range (cm) for object in Fig. 7.15.

Again, a continuous profile, indicating no discontinuities along the length of the object but the same characteristic as the first order derivative to approach infinity, albeit negative infinity in this case, as it nears zero.

Given that there are no discontinuities along the length of the object, let's examine the expected discontinuities at $x = 0$ cm. For the cross-sectional area, the discontinuity equation is,

$$\begin{aligned} D(A_w, 0, 0) &= A_w(r_{0-}) - A_w(r_{0+}) \\ &= (0) - (0) \end{aligned} \tag{7.45}$$

As expected, since the cross-sectional area of the object at $x = 0$ cm is the same as the the free space region, namely zero.

For the derivative of the cross-sectional area with respect to range however, the discontinuity equation has an infinity at $x = 0$ cm, shown in Eq. (7.46) below,

$$\begin{aligned}
D(A_w,0,1) &= \frac{dA_w}{dr}(r_{0-}) - \frac{dA_w}{dr}(r_{0+}) \\
&= (0) - \left(\frac{4.96\pi}{0^{1/2}}\right). \\
&= (0) - (\infty) \\
&= -\infty
\end{aligned} \tag{7.46}$$

It follows that this step discontinuity will be responsible for the production of an image pulse at this point. However, despite the first order discontinuity being of infinite magnitude, in practice we would, of course, observe a finite echo, albeit of large magnitude. The fact that an infinite first order discontinuity would be processed by the forward model as (incorrectly) resulting in an echo of infinite magnitude, with the converse holding true for the inverse model, highlights one of the limitations of the model.

The same principle holds true for the discontinuity of the second order derivative with respect to range, shown below,

$$\begin{aligned}
D(A_w,0,2) &= \frac{d^2 A_w}{dr^2}(r_{0-}) - \frac{d^2 A_w}{dr^2}(r_{0+}) \\
&= (0) - \left(-\frac{2.48\pi}{0^{3/2}}\right) \\
&= \infty
\end{aligned} \tag{7.47}$$

Again, a large contribution to the echo at $x = 0$ cm would be expected due to this discontinuity, but not an infinite one.

In summary, the fourth order object has discontinuities of infinite magnitude in both the first and second order derivatives of cross-sectional area with respect to range at $x = 0$ cm. These are summarised in the table below,

Location of D(n)	D(0)	D(1)	D(2)
0 cm	0	$-\infty$	$+\infty$

Table 7.6. Discontinuities on the 4th order object.

In the following chapter, we will examine experiments that were conducted with the objects listed above to test the validity of the inverse models we developed in the previous chapter and see how well they were able to predict the geometries of the objects examined in this chapter.

8 Experimental Design, Results and Analysis

Our task was now to use the selected objects listed in the last chapter to test the time dependent inverse model we developed earlier. But before we could begin some decisions had to be made. Specifically, what two frequencies would be used and what range would the objects be placed at. Given that the Polaroid transducer we have been using has a maximum output at 50 kHz, with a gradual fall off in sensitivity above and below this frequency, it was decided that our chosen frequencies should fall on either side of this peak output. Thus we selected 40 kHz and 60 kHz as the frequencies of choice as they are each close enough to 50 kHz to provide a signal which is not too weak whilst at the same time being sufficiently separated along the spectral band in order that they should produce echoes that are noticeably unique from one another.

As for the range, we selected 40cm. Even though this range is borderline for the validity of the Kirchhoff approximation, preliminary tests showed us that the echoes at ranges beyond this were too weak for us to reasonably expect to see any contribution from any of the higher order discontinuities. As the detectable presence of these higher order contributions is necessary for the inverse model to work, we had to limit our range accordingly. This differs from our experience testing the forward model, where we were able to set our scattering objects at 80cm and beyond. But in that instance, we were dealing with a model in which the sizes of the higher order discontinuities had little impact upon the validity of the model being tested, given their very small magnitude. With the inverse model however, the situation is exactly the reverse, as one would expect. Plus we had the advantage of using a strong 50 kHz peak signal, unlike the current situation where the output at 40 kHz and 60 kHz is only approximately half as strong as that at 50 kHz. Thus 40cm is a reasonable compromise between ensuring that

the Kirchoff approximation is held true and making sure our echo is strong enough to analyse in detail.

However, the general procedure for obtaining the echoes was not dissimilar to that employed earlier when we tested the validity of the extended forward model, save the differing frequencies and ranges already mentioned. Before we began taking readings, the region around the apparatus was checked to ensure it was clear of any drafts from nearby windows, doors or air conditioner vents, as these cause air turbulence and changes in environmental conditions. The air conditioner in the laboratory was switched off 15 minutes prior to the start of the experiment to give the temperature time to settle. A sample echo reading was taken with no scattering object present to ensure that there were no extraneous objects within the field of insonification, as these clearly show up in the echo trace when present. Other checks were also conducted such as ensuring that the bias on the transducer was correct (150V) and the amplification setting in the capture software was high enough to produce the largest echo without clipping. Other software settings on the chirp/capture software mimicked those used during the forward model tests, specifically a 10 cycle wave is emitted, the echo sampled at a rate of 1Mhz and the procedure repeated 100 times. This multi-sampling is necessary for the same reasons that it was employed for the forward model experiments, to minimise random, short-term fluctuations in the environment.

At this stage, the apparatus was ready and the first object was mounted at 40cm ready for insonification, At the conclusion of the measurement cycle for an object, the frequency was changed from 40kHz to 60kHz and the entire measurement cycle was repeated. Once the readings from the object at both frequencies had been obtained, the environmental conditions were recorded as we would need this information later in order to calculate the matrix elements used in the inverse model. The object was then

demounted, the next object in the series put in its place and the process repeated until all six objects had been examined.

8.1 Experimental Results

A. Determining $K(f)$

Before we can test the predictions of the inverse model, we must firstly calculate the matrix elements of the model for each case in order for it to become workable. As stated back in Chapter 6, in order for us to calculate the matrix elements $Y_x(f)$ of the model for each frequency, we firstly need to calculate or measure $K(f)$. We also determined that the best approach, both in terms of speediness and accuracy, was to calibrate the model with an object of precisely known dimensions and thereby determine $K(f)$ directly through measurement, the best candidate for this being an object that has all $D(n) = 0$, except for one, such as a paraboloid for instance. We have two paraboloids within our set, each suitable candidates, however we'll use the second of these as it has a larger discontinuity which should produce a stronger echo and thus a more accurate result. We could also have used any of the spheres that we employed previously to test the forward model, but we opted to go with the paraboloids because they are more finely machined and thus their geometry is known to a higher degree of accuracy than the spheres.

Eq. (6.16) reduces to a simpler form in the instance where we are using a scatterer with all $D(n) = 0$ except for $n = 1$,

$$E_g = -K(f) \frac{D(1)}{2k} \cos \theta \quad (8.1)$$

For Paraboloid B, examined in section 7.4, the first order discontinuity has a value of -4.9π . This reduces Eq. (8.1) further to,

$$E_g = K(f) \frac{2.45\pi}{k} \cos \theta \quad (8.2)$$

At it's peak, when $\cos \theta = 1$, the voltage has a maximum value given by,

$$E_{g_{MAX}} = K(f) \frac{2.45\pi}{k} \quad (8.3)$$

and given that $k = \frac{2\pi f}{c}$ it follows that,

$$E_{g_{MAX}} = K(f) \frac{1.225c}{f} \quad (8.4)$$

allowing $K(f)$ to be determined by,

$$K(f) = \frac{E_{g_{MAX}} f}{1.225c} \quad (8.5)$$

This can be readily calculated as the frequency f is known in each case, the maximum voltage $E_{g_{MAX}}$ can be measured from the data, or more accurately it's interpolated counterpart, and the speed of sound c is easily calculated from a knowledge of the environmental conditions at the time of measurement, which we recorded.

For the echo from Paraboloid B we had a recorded temperature of 22.9 °C, a humidity of 36.85% and a pressure of 1037.5mB. This results in a speed of sound c of 345.0 m/s. In the 40 kHz case, the maximum voltage measured off the paraboloid was found to be 0.01778V, thus our value of $K(f)$ at this frequency is deduced thus,

$$K(40kHz) = \frac{(0.01778)(40000)}{1.225(345.0)} = 1.68 \quad (8.6)$$

For the 60 kHz case, the maximum was found to be 0.02009V and therefore the value of $K(f)$ is given by,

$$K(60kHz) = \frac{(0.02009)(60000)}{1.225(345.0)} = 2.85 \quad (8.7)$$

These calibration constants, $K(40kHz)$ and $K(60kHz)$, will be used in the later sections to aid in the determination of the matrix elements that go up to make the inverse model, because for each object these matrix elements will differ. Although strictly it would be preferable to calibrate the model before each and every new scatterer is tested, we decided that this would be unnecessary. This is because the impact upon the value of $K(f)$ from the small environmental changes that occur over the entire run of measurements is minimal, given the rather short time span, 10 – 15 mins, during which the measurements are conducted.

B. Selecting an appropriate time index t

The general equation of the inverse model has the following form,

$$\begin{bmatrix} D(1) \\ D(2) \end{bmatrix} = \begin{bmatrix} Y_2(f_1) & Y_3(f_1) \\ Y_2(f_2) & Y_3(f_2) \end{bmatrix}^{-1} \begin{bmatrix} E_g(f_1) \\ E_g(f_2) \end{bmatrix} \quad (6.23)$$

$$\text{where, } Y_2(f) = -\frac{K(f)}{2k} \cos \theta \quad \& \quad Y_3(f) = \frac{-K(f)}{4k^2} \sin \theta$$

$$\text{and } \theta = \omega t - 2kr_g = 2\pi f \left(t - \frac{2r_g}{c}\right)$$

If we invert the matrix and expand it out to its full form, we get the following,

$$\begin{bmatrix} D(1) \\ D(2) \end{bmatrix} = \begin{bmatrix} A & B \\ C & D \end{bmatrix} \begin{bmatrix} E_g(f_1) \\ E_g(f_2) \end{bmatrix} \quad (8.8)$$

where,

$$A = \frac{-2k_1^2 \sin[2\pi f_2(t - \frac{2r_g}{c})]}{K(f_1) \left(k_1 \cos[2\pi f_1(t - \frac{2r_g}{c})] \sin[2\pi f_2(t - \frac{2r_g}{c})] - k_2 \cos[2\pi f_2(t - \frac{2r_g}{c})] \sin[2\pi f_1(t - \frac{2r_g}{c})] \right)}$$

$$B = \frac{2k_2^2 \sin[2\pi f_1(t - \frac{2r_g}{c})]}{K(f_2) \left(k_1 \cos[2\pi f_1(t - \frac{2r_g}{c})] \sin[2\pi f_2(t - \frac{2r_g}{c})] - k_2 \cos[2\pi f_2(t - \frac{2r_g}{c})] \sin[2\pi f_1(t - \frac{2r_g}{c})] \right)}$$

$$C = \frac{4k_2 k_1^2 \cos[2\pi f_2(t - \frac{2r_g}{c})]}{K(f_1) \left(k_1 \cos[2\pi f_1(t - \frac{2r_g}{c})] \sin[2\pi f_2(t - \frac{2r_g}{c})] - k_2 \cos[2\pi f_2(t - \frac{2r_g}{c})] \sin[2\pi f_1(t - \frac{2r_g}{c})] \right)}$$

$$D = \frac{-4k_2^2 k_1 \text{Cos}[2\pi f_1(t - \frac{2r_g}{c})]}{K(f_2) \left(k_1 \text{Cos}[2\pi f_1(t - \frac{2r_g}{c})] \text{Sin}[2\pi f_2(t - \frac{2r_g}{c})] - k_2 \text{Cos}[2\pi f_2(t - \frac{2r_g}{c})] \text{Sin}[2\pi f_1(t - \frac{2r_g}{c})] \right)}$$

The presence of trigonometric terms in the denominators of the matrix elements have the consequence that an ill-chosen value of the time index t could cause all the matrix elements to become singularities (ie. infinite). Further, if any trigonometric terms in the numerators become zero, then the contribution of the associated $E_g(f_1)$ or $E_g(f_2)$ coefficient would vanish. This would mean that the data obtained for the amplitude measurement at one of the frequencies would not contribute to the calculation, which would diminish the accuracy of the result as a consequence and is thus to be avoided.

The value of t should thus be chosen to strike a balance between all the terms such that no term is in danger of becoming either a singularity or zero. To determine which value(s) of t satisfy this condition optimally, we'll examine a ratio which is the product of the first and second terms divided by the product of the third and fourth, shown in reduced form in Eq. (8.9) below,

$$R(\theta) = \frac{K(f_1)^2 k_2^3 \text{Cos}[2\pi f_1(t - \frac{2r_g}{c})] \text{Sin}[2\pi f_1(t - \frac{2r_g}{c})]}{K(f_2)^2 k_1^3 \text{Cos}[2\pi f_2(t - \frac{2r_g}{c})] \text{Sin}[2\pi f_2(t - \frac{2r_g}{c})]} \quad (8.9)$$

The optimal choice for t , which occurs when the four matrix terms are closest to one another and therefore have values which are neither zero or infinite, will manifest itself in the ratio function as that point where the ratio is closest to one.

After substituting into Eq. (8.9) the values for $K(f)$, f , k , r_g & c , for both 40kHz and 60kHz, we can plot the variation of this ratio function over the course of approximately 10 wavelengths, the typical length of a received echo. The *extreme* sensitivity of the ratio function to the choice of t at certain points is revealed in Fig 8.1 below,

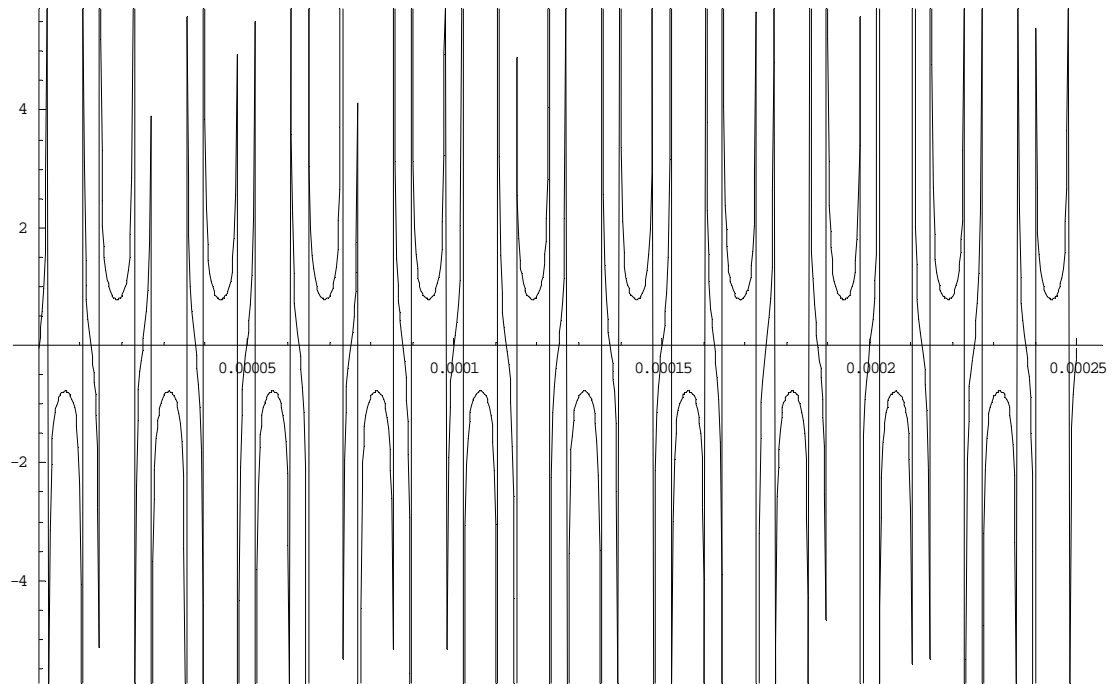


FIG. 8.1. Variation of the ratio function $R(\theta)$ with angle across 10 wavelengths.

Given the obvious cyclic repetition of the variation, as seen above, we can focus on the detail within a single wavelength as representative of the greater structure of the wave train. This is shown in Fig. 8.2 below,

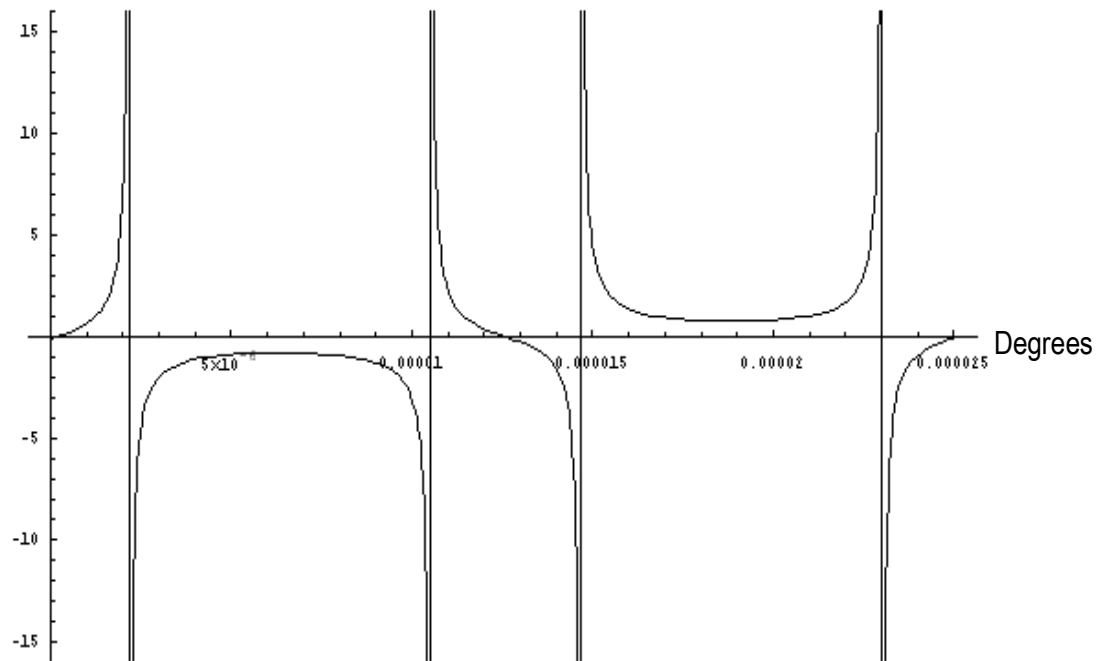


FIG. 8.2. Variation of the ratio function $R(\theta)$ with angle across a single wavelength.

The plot above has a length equivalent to one wavelength, 0 to 360 degrees, of a 40kHz echo. We can see that the first ‘danger spot’ occurs at approximately 30 degrees along the wave where the ratio approaches a singularity. There follows a stable region from about 60 to 120 degrees where the ratio has a magnitude of approximately one, albeit negative one, followed by another singularity around 150 degrees. Another danger spot is at 180 degrees where the ratio becomes zero. From 180 to 360 degrees these patterns are repeated, but inversely. As can be seen from Fig 8.1, these variations are then repeated throughout the rest of the wave train.

It follows then that we should be safe, in the sense that our matrix elements are not in danger of veering towards infinity or zero, provided our choice for the time index t lies between 60 to 120 degrees (or 240 to 300 degrees, etc...) along the 40kHz wave train. But what range of angles does this choice for t correspond to along the secondary 60kHz wave? Well, since the 60kHz wave has a frequency that is exactly 50% higher

than the 40kHz wave, clearly then the corresponding angles will be 50% higher. Thus the region between 60 to 120 degrees on the 40kHz wave will correspond to 90 to 180 degrees on the 60kHz wave. Given this, the most efficient choice for the time index t is the location of the first peak on the 60kHz wave, since the first peak will always be at 90 degrees, which satisfies our requirement to be within the ‘safety zone’ for 60kHz waves, and is quite easy to localise on the wave train. Also, this time index at 90 degrees on the 60kHz wave will correspond to that at 60 degrees on the 40kHz wave, which is within the ‘safety zone’ for that wave frequency. Hence, by choosing the first peak on the 60kHz wave train we’ve chosen a time index t that is within *both* ‘safety zones’.

Of course, given the cyclic repeating nature of the ratio equation, there is no need for the peak chosen to be the first one. Provided that the next point chosen is exactly 180 degrees removed from the previous, it will also fall within one of the ‘safety zones’ of Fig. 8.2 and as all peaks are removed from each other by 180 degrees anyway, it follows that any peak is a suitable candidate. It is best however to choose a peak that is at least 2 to 3 wavelengths into the wave train though, as this ensures that we avoid sampling the “ramp up” period on the wave train.

C. Results

After the value of t is chosen, the echo amplitudes at that time index are recorded for both the 40 kHz and 60 kHz echoes. These values, along with the pre-calculated and/or recorded values for $K(f)$, f , k , r_g & c , for both 40 kHz and 60 kHz, are substituted in Eq. (8.8) to produce estimates of $D(1)$ & $D(2)$. An example of this process, using the exponentially shaped scatterer, is shown in Appendix A.5 (b).

Data for figures used in this section, pertaining to measured and predicted discontinuities, are provided in Appendix A.4. The predicted first order discontinuities are plotted alongside the measured values calculated back in Chapter 7 and are shown below,

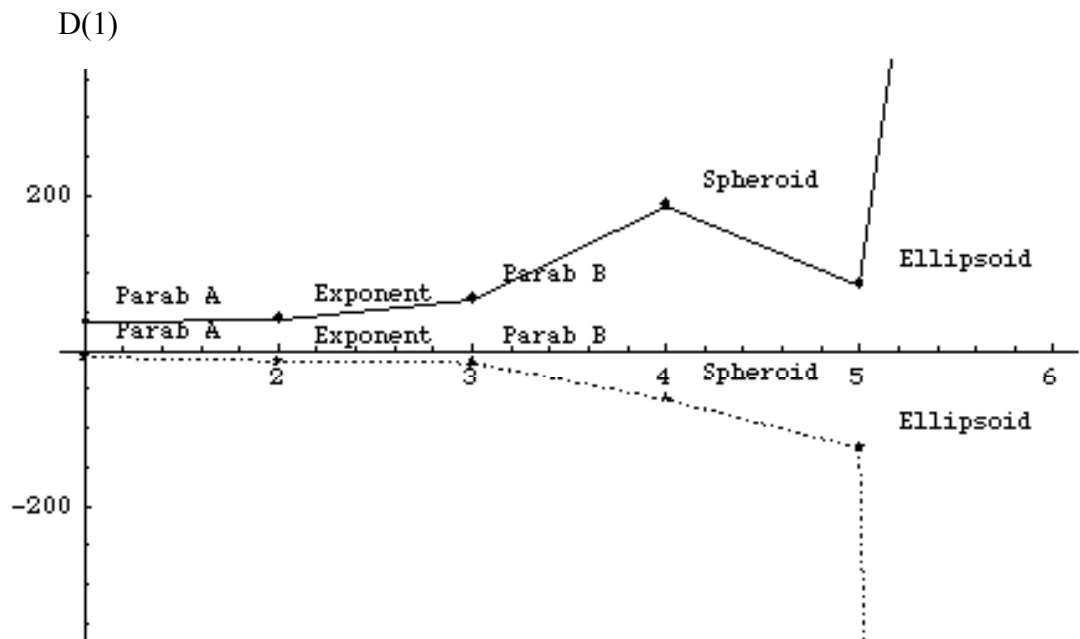


FIG. 8.3. Comparison of Calculated (broken line) with Predicted (solid line) values for D(1)

The data points for the sixth (and last) object (the 4th order scatterer) are unseen and unlabeled simply because they are far beyond the scale of the plot. Clearly, from observation alone, the calculated and predicted results do not match. Interestingly enough however, if we simply switch the sign on the predicted results, there is far greater correlation, as seen in Fig. 8.4 below,

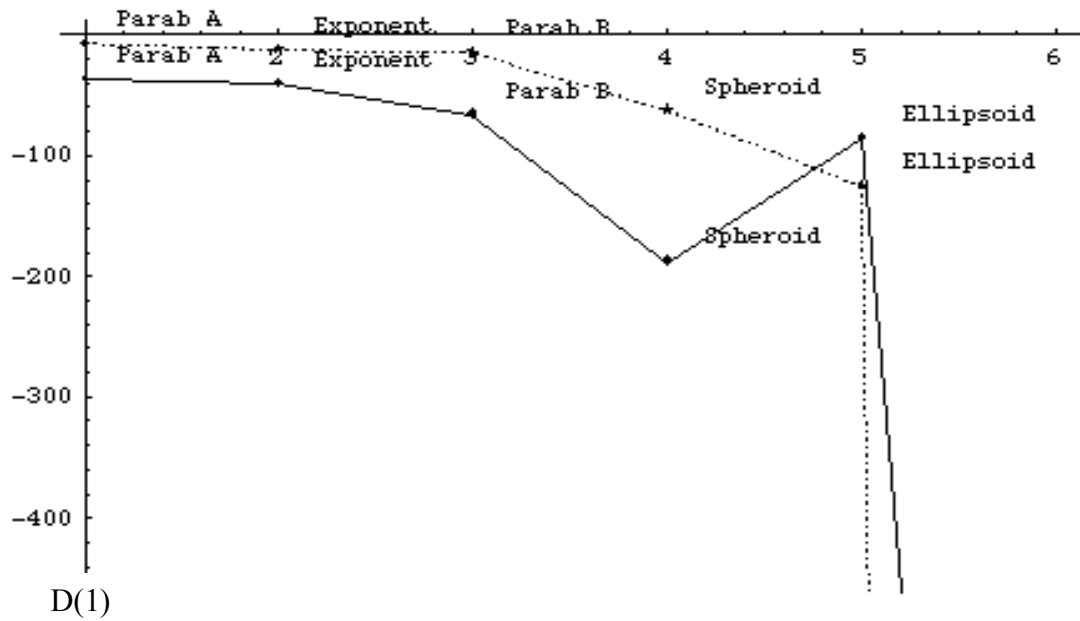


FIG. 8.4. Comparison of Calculated (broken line) with $-1 \times$ Predicted (solid line) values for $D(1)$

Further, if we scale the predicted results by dividing them by 3, the correlation is even more compelling, as shown in Fig. 8.5 below,

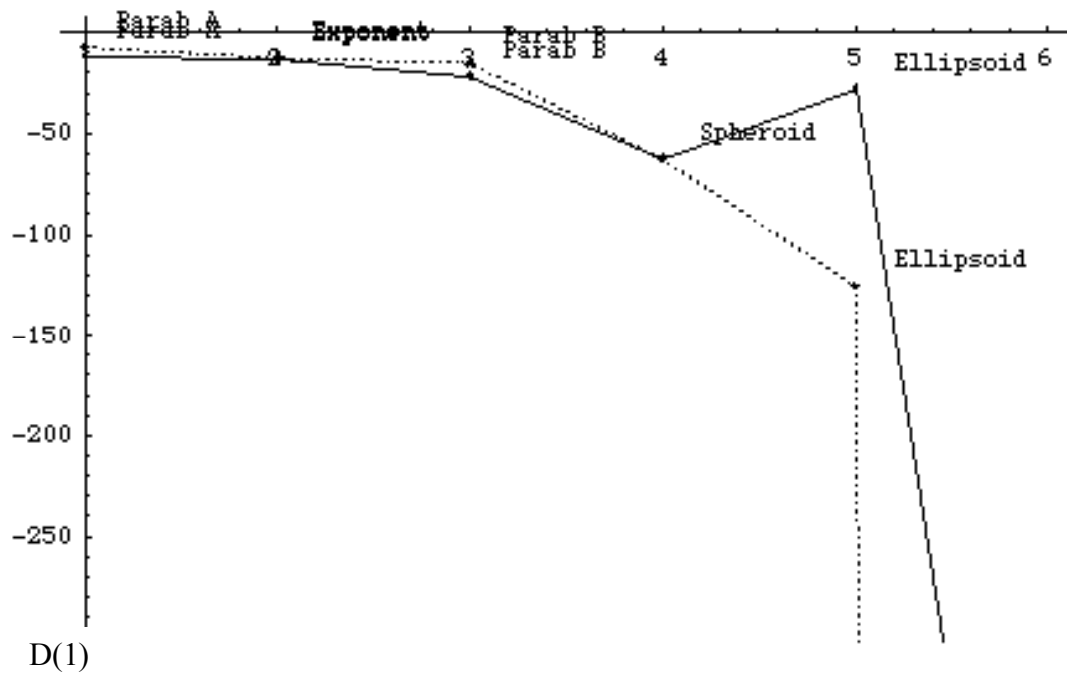


FIG. 8.5. Comparison of Calculated (broken line) with $-(1/3) \times$ Predicted (solid line) values for $D(1)$

Thus by introducing this “calibration factor” into the model, we have significantly improved its accuracy. Random noise in the data used is the actual reason why this factor serves to improve the correlation between measurement and theory, but at this stage it will not be clear to the reader why this indeed the case. The details of why data errors can impact upon the predicted values for $D(n)$ (and by extension the calibration factor) are discussed in section 8.1 (d), as well as discovering why the sign of the predicated values is the opposite of those calculated.

Even though it’s not directly visible on the figure above, due to the limitations of scale, the 4th order scatterer has a poor correlation between the calculated and predicted values. The calculated value was negative infinity, but the model predicted value veers off to the large *but not infinite* value of –632. However, this poor correlation was to be expected because real-world objects can never have an infinite discontinuity any more than say, the tip of a pin can have a radius of curvature exactly equal to zero. Thus our predicted value is what we would have expected, a value much larger than the other objects, but not infinite. The only major anomaly therefore is the ellipsoid, though we will show later that individual anomalies hold little significance as matrix instability accounts for the gross characteristics of Fig. 8.5.

Let’s also take a look at the plot of calculated versus predicted values for the second order discontinuities $D(2)$. This is shown in Fig. 8.6 below,

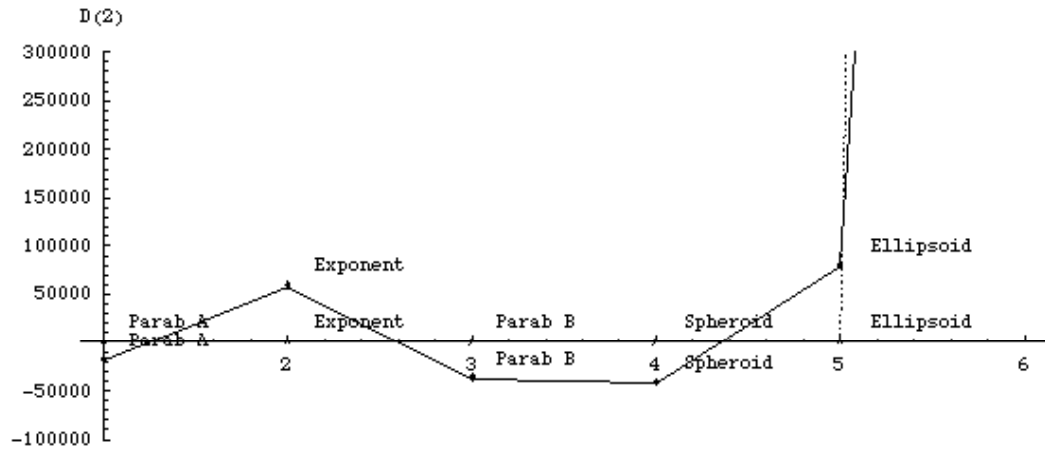


FIG. 8.6. Comparison of Calculated (broken line, which is too close to zero to be visible) with the Predicted (solid line) values for $D(2)$

The broken line indicating the calculated, or true, values for $D(2)$ is not visible because they're limited to values under 30 (with the exception of the last object, the fourth order object which, as before, has a value of infinity) and the much larger values on the predicted line have drowned them out. If we scale the results by dividing the predicted values by, say, 10000, we can compare them more easily. This is shown in Fig. 8.7 below,

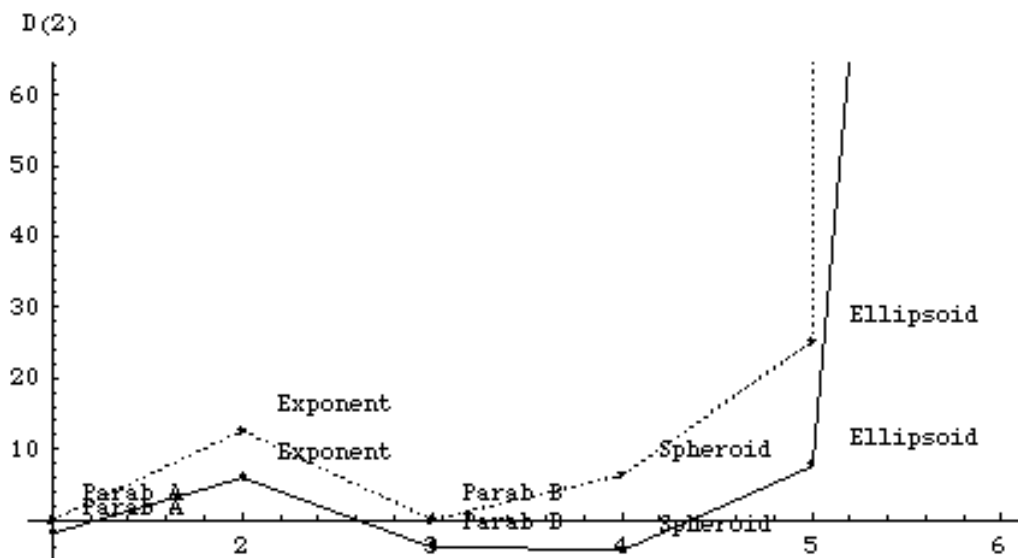


FIG. 8.7. Comparison of Calculated (broken line) with the $(1/10^4) \times \text{Predicted}$ (solid) values for $D(2)$

Despite the obvious disparity between the calculated and predicted values for $D(2)$ it is of note that the trend in the predicted values mirrors that of the calculated values, despite the obviously large difference in magnitude. Despite this small consolation, it's clear that unlike the results obtained for $D(1)$ we cannot use the model to make meaningful predictions for $D(2)$, even when imposing a 1/10000 scaling factor. It would appear that the model *can* however be used to at least make qualitative estimates of general trends in the values of $D(2)$.

As a final test for the model, let's compare the calculated and predicted values for the discontinuities of the spheroid-paraboloid at its "crossover" region, the region where the object's spheroidal surface changes to a parabolic one, 5cm from its vertex. This is the first test of a discontinuity that is actually *on* the surface of the scatterer rather than one that exists at the transition point from free space to a solid object. Our previously calculated values for the discontinuities at this point were determined in Chapter 7 and are given below,

$$D(A_w, 5, 1) = 9.27 \quad (7.23)$$

$$D(A_w, 5, 2) = -6.28 \quad (7.25)$$

The predicted discontinuities (*unscaled*) are given below,

$$D(A_w, 5, 1) = 3.21 \quad (8.10)$$

$$D(A_w, 5, 2) = 282 \quad (8.11)$$

Very poor correlation is observed with these figures. Even when applying the scaling factors we determined earlier, the predictions remain erroneous and in fact show even worse correlation,

$$D(A_w, 5, 1) = -1.07 \quad (8.12)$$

$$D(A_w, 5, 2) = 0.0282 \quad (8.13)$$

The poor results in this case are almost certainly a result, at least in part, of the very weak signal received from this crossover region, the signal therefore being heavily impacted upon by the noise floor of our system. To illustrate this problem, we present below the sampled wave trains for the spheroid-paraboloid at both 40 kHz and 60 kHz,

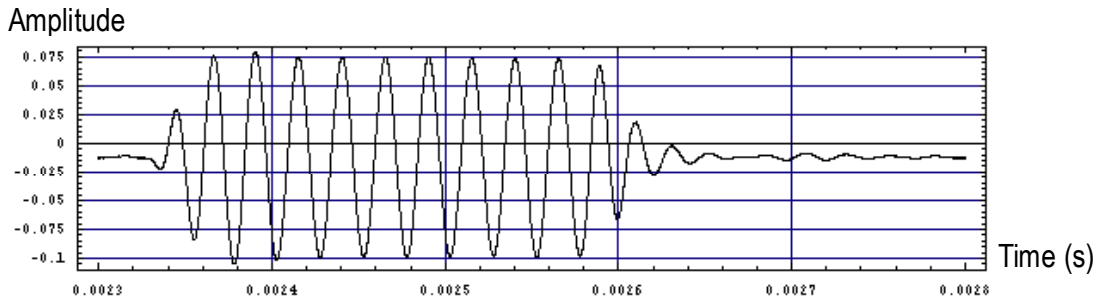


FIG. 8.8. 40kHz echo from the spheroid-paraboloid

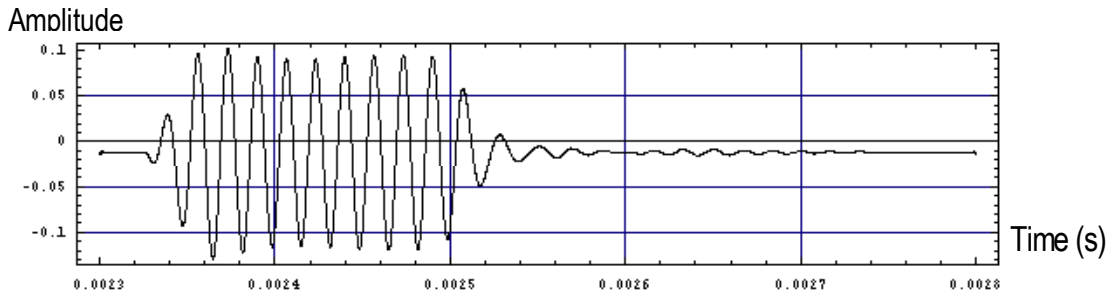


FIG. 8.9. 60kHz echo from the spheroid-paraboloid

The echo from the crossover region is visible as a weak secondary trace trailing the main echo from 0.00261s to 0.00273s. Now, we are required by the constraints of the model to ensure that the time index t chosen to sample the echo amplitude must be the same for both frequencies, so we need to choose a time index for which the echo is clear enough on both echoes for sampling. It's clear that the only point on Fig. 8.8 where the secondary echo is clear enough to sample is at $t = 0.00270\text{ms}$ and beyond. Unfortunately, this region is very weak in the 60 kHz wave trace. However, as stated above, we have no other choice but to use this time index.

The degree to which the inverse model is only partially successful, specifically the partial success of the model at predicting $D(1)$, after scaling, but complete inability to determine $D(2)$ accurately, discounting its limited qualitative success, is not unexpected. As we pointed out earlier, the contributions to the echo of the second order discontinuities are of the order of 10^3 times smaller than those of the first order. Given that the noise in the system is on a similar scale, it follows that it will be very difficult for these contributions to add to the signal in such a manner that they are *distinct* enough for the model to use them in a meaningful manner.

However, the problem of trying to explain the difference in sign between the calculated and predicated results hints at a more fundamental problem. With this in mind, we adopted a couple of changes in the methods used to manipulate the raw data and select the sample time t . Specifically, we decided to try fitting a sinusoidal function to the data rather than interpolating it, since we know that the echo will be sinusoidal in form. Also, we adopted the condition number of the inverse matrix as the determining factor for the sample time t , since this number is indicative of the sensitivity of the matrix, and by extension the inverse model, to inaccuracies in the data. The results of these changes follow.

D. Fitting a sinusoidal function to the echo data

Because the echo received is generally sinusoidal in form, it's reasonable to assume that it can be approximated by a sinusoidal function. As before, our interest lies solely on the central region of this echo where the wave is essentially monotonic. The monotonicity of this region also aids us in our attempt to fit a sinusoidal function, since such a function will by necessity be single frequency. The process used to fit a function to our data follows.

Using Mathematica, we create a subset of the echo data that contains only the central monotonic region. The echo data and its corresponding subset, for the exponentially shaped scatterer, are shown in Fig. 8.10 below.

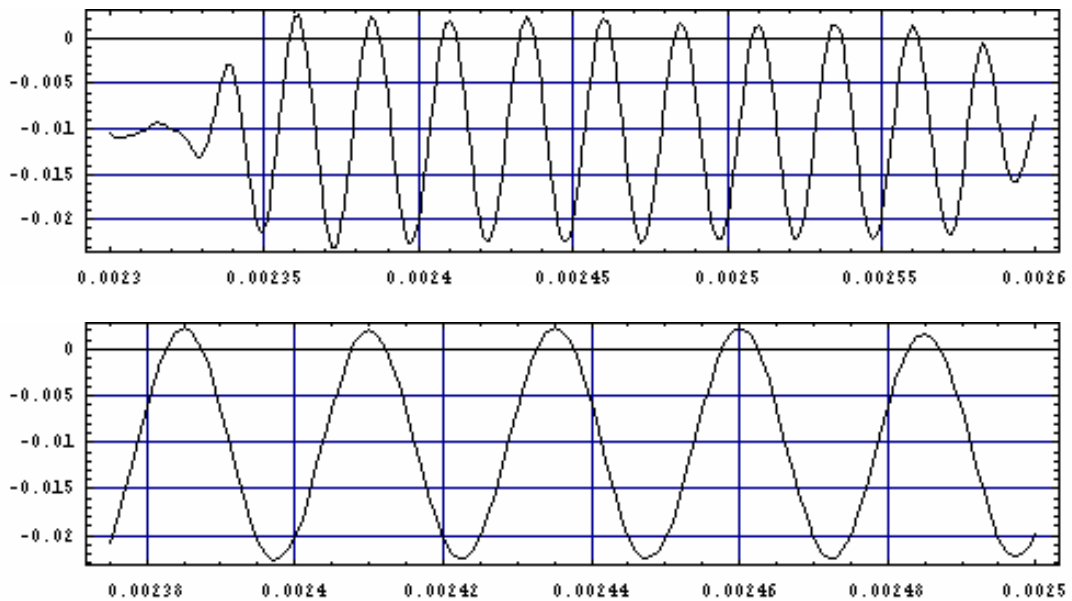


FIG. 8.10. Original echo data (top) and it's subset taken from the monotonic region (below).

We then need to transform the structure of our data to one suitable for Mathematica's equation fitting function(s). Our data is stored as a one dimensional array, a series that contains the instantaneous amplitude of the echo at discrete time intervals along the full

length of the wave train. Mathematica's equation fitting function, *NonLinearFit*, requires a two dimensional array as one of it's arguments. To create this array, we simply use successive elements of the one dimensional array and their associated time indexes as the co-ordinates for successive points within the two dimensional array. The general form of the equation to be fit to the data is then declared, which in this case is,

$$E(t) = A \sin(\omega t + \phi) + C \quad (8.14)$$

where $\omega = 2\pi f$

and f = frequency

Parameters such as A representing wave amplitude, C representing bias and ϕ the phase are all determined by *NonLinearFit*. Frequency is a known quantity in each instance. Once these parameters are determined by *NonLinearFit*, a plot of Eq. (8.14) is superimposed over a plot of the subset data to ensure it's a valid fit. An example of such a superposition, for the exponentially shaped body, is shown in Fig. 8.11 below.

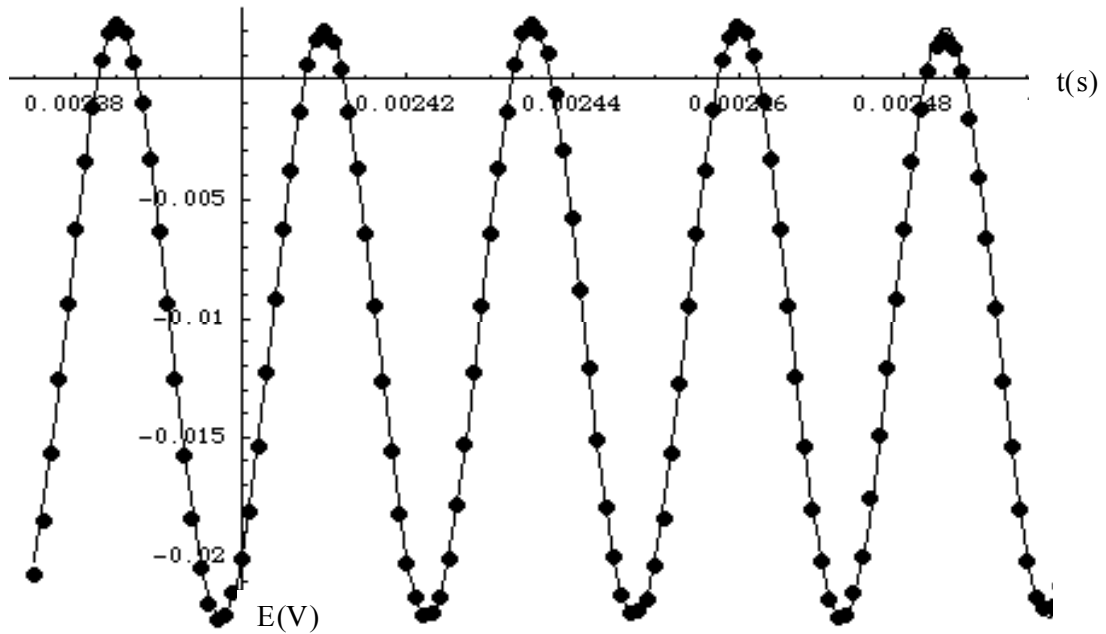


FIG. 8.11. Superposition of Eq. (8.14) over the sampled data (solid points) to verify correlation.

In all cases Mathematica was able to provide an equation with a high correlation to the data. A full example of this curve-fitting process, using the exponentially shaped scatterer, is given in Appendix A.5 (c).

The second alternation to our data analysis procedure relates to the use of the condition number to measure matrix stability. This is a more rigorous approach than the one employed previously. The condition number of a matrix with respect to inversion is a measure of how sensitive the matrix is to perturbations. The lower the condition number, the more stable, or well-conditioned, the matrix is. Conversely, matrices with large condition numbers are regarded as ill-conditioned. In the context of our inverse model, the order of the condition number provides a rough estimate of how many digits of precision are lost from our estimates of $D(n)$ as a result of the matrix inversion. For example, a condition number of 3×10^2 , having an order of two, indicates that two digits of precision are lost from the estimates of $D(n)$. So, if the data used only had a precision of say three significant figures, then after subtracting two digits of precision we're left with an estimate of $D(n)$ precise to only one significant figure, which would be a poor estimate. Clearly, to avoid an outcome with low precision estimates of $D(n)$ we require either a low order condition number, high precision data or preferably both. Although sufficient data precision will provide the necessary stability to our model, systematic error in the model will be evident unless the data is also *accurate* to the same resolution. For this reason, we speak of the requirements of data accuracy rather than just precision from this point on. The condition number of the matrix is determined by the Mathematica function *LUdecomposition*. This function accepts the matrix as an argument and returns three values, the third being an estimate of the condition number.

The principal task then is to determine the time indices at which the condition number is minimised. Plotting the condition number of the matrix as a function of time

we see that there are minima at several points along the wave train, approximately coincident upon echo minima and maxima. See Fig. 8.12 for an example of this for the exponentially shaped scatterer.

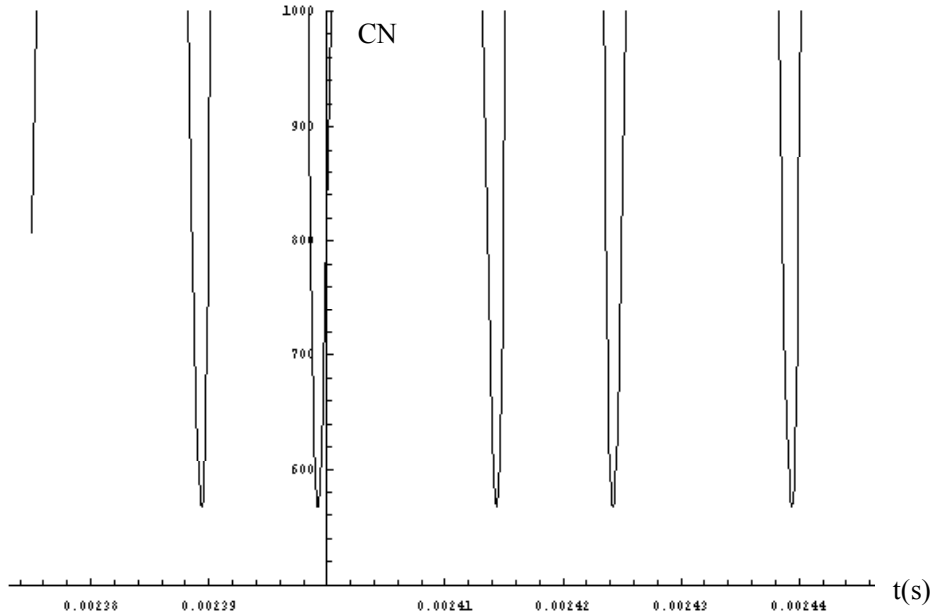


FIG. 8.12. Condition number of the inverse matrix as a function of time.

The condition number at all minima never falls far below 6×10^2 , indicating that the matrix is never well conditioned and will lead to a loss in precision of two digits from any estimates of $D(n)$. The significance of this is high as it severely limits the accuracy of our model, with the major implication of this to be discussed later.

Given the lack of variation in condition number across the various minima, we could *apparently* select any of the minima in the plot above as our chosen time index, as each will produce a matrix with minimised instability from which we can then attempt to predict $D(I)$. However, the choice of minima is important. Not apparent to us previously was that the sign of the predicted value of $D(I)$ varies with the choice of minima. Whereas a time index at one minima may produce a negative prediction for $D(I)$, the time index at the next minima will predict one roughly equal in magnitude but

opposite in sign to that predicted previously. For each successive minima, the sign of the predicted $D(l)$ continuously flip-flops between positive and negative in this manner. This accounts for previous predictions of $D(l)$ using the inverse model which resulted in values with a sign at odds with the measured result.

Given our awareness of the issue with the sign, it was a simple matter of collating the predictions for $D(l)$ at each minima and then rejecting the positive valued solutions. This was justifiable on the grounds that $D(l)$ can never be positive valued since it is a function of the cross-sectional area in air (ie. zero) *minus* the cross-sectional area of the scattering body (which can only be zero or positive valued). Hence the result can only be either zero or negative valued. The remaining solutions, three usually, are then averaged and the resulting value used as our model prediction of $D(l)$. A full example of this process, using the exponentially shaped scatterer, is given in Appendix A.5 (c). The results for all scattering objects are given in Fig. 8.13.

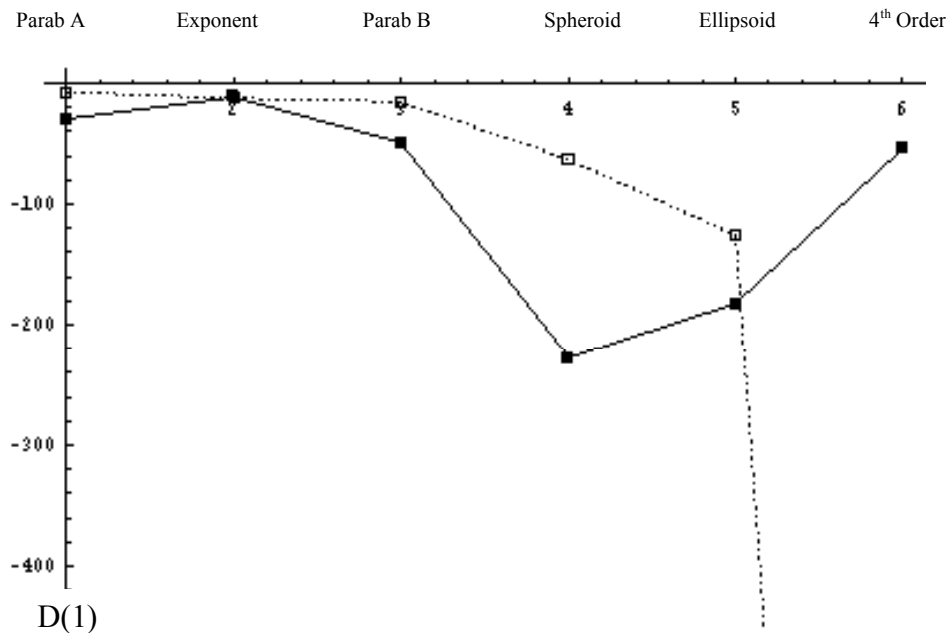


FIG. 8.13. Comparison of Calculated (broken line) with Predicted (solid line) values for $D(1)$

Given our new found awareness of the fundamental cause of the lack of correlation between theory and experiment, namely the sensitivity of the matrix to data inaccuracies as measured by the condition number, it is redundant to repeat our earlier attempt to correct the model by multiplying the inverse model predictions by a factor to provide better correlation. This would only work, possibly, if the inverse model suffered from a *systematic* error, but clearly this is not the case. Similarly, there was no improvement in the predictions for $D(2)$ using these techniques, for the same reasons as discussed previously.

In summary then, fitting a curve to the data produced no tangible increase in model accuracy over the previously employed method of interpolation. The use of the condition number proved helpful in explaining the conundrum of the flipped sign and was illustrative of the lack of stability of the matrix. However, as with the curve fitting it provided no tangible increase in model accuracy. The reasons that these two techniques offered little improvement over those methods employed earlier are simply because their improvements to the model, if any, were far too subtle to be observed given the vast discrepancies between measured and predicted values. Under more ideal circumstances, namely when dealing with a stable matrix or with data of much higher accuracy, we believe that the latter techniques employed would provide more tangible improvements in model accuracy than those observed here.

8.2 Error Analysis

As outlined in section 4.1 (a), the data used was accurate to within 0.8% in 95% of cases. Therefore we can report data to a maximum of only three significant figures (three digits of precision). The condition number of just under 6×10^2 , having an order of

two, results in a loss of precision of two digits from any estimates of $D(n)$. The net effect of these two factors is that predictions of $D(I)$ have a precision and accuracy of only one significant figure, although we need to remember that the condition number is only a *rough* estimate of the loss of precision – inspection of Fig. 8.5 indicates that the accuracy of the predictions for $D(I)$ may be even lower. This alone is enough to account for the large discrepancy between theory and measurement we have observed and of all the sources of error contributing to these discrepancies, clearly it is the most significant. However, it is instructive to analyse the other possible sources of error that could also contribute, albeit on a less significant scale.

Discounting the impact of the unstable matrix for now, could the large errors in the inverse model also arise from smaller deviations in the original forward model, upon which it's based, and thus be compensated for? As the terms that constitute the forward and inverse models are the same, just rearranged, both questions are thus two sides of the same coin, as they relate to how small changes in these terms impact upon the predictions.

Specifically, the terms in the models for which there is an associated uncertainty due to their capacity for variation during the course of a measurement, are listed below, along with their errors,

Temperature T :	2 K error
Humidity H :	2% error
Pressure P :	1 mB error

The remaining terms within the models, such as frequency, range and speed of sound have either negligible error, such as the former, or are functions of the environmental

conditions listed above, such as the latter. In either case, the only terms that are sources of error in the models are the environmental terms above.

The questions that we need to address are firstly, what impact do these environmental fluctuations have upon the predictions of the inverse model and secondly, are any of these terms sensitive enough to produce deviations of the order seen in the inverse model's predictions? If the answer to the second question is yes, then it would be possible to apply either a scaling factor or an offset to the offending term in the forward model and then propagate that term through the inverse model. The end result would be a forward mode that is still relatively valid, assuming the modification to the offending term in the forward model is small, and an inverse model with higher correlation between theory and measurement. This would be the ideal case.

The most efficient way to measure the errors on the predictions of the inverse model is to examine the worst case scenarios for each case. Thus we plug in values for temperature, pressure and humidity that will produce the greatest deviations from the predicted values in both directions, thereby obtaining the error limits for the each case. For example, the exponentially shaped object has a predicted value of $D(I) = -11.0$. The worst case scenario for *each term's* impact upon this prediction is as follows:

$$\begin{aligned} \text{Humidity} &= 49\% + 2\% = 51\%, & D(I) &= -11.0 \\ \text{Humidity} &= 49\% - 2\% = 47\%, & D(I) &= -10.9 \end{aligned}$$

It's thus clear the humidity plays an almost negligible role in the final prediction for $D(I)$. For pressure,

$$\begin{aligned} \text{Pressure} &= 1038 \text{ mB} + 1 \text{ mB} = 1039, & D(I) &= -11.0 \\ \text{Pressure} &= 1038 \text{ mB} - 1 \text{ mB} = 1037, & D(I) &= -11.0 \end{aligned}$$

Again, a negligible impact upon the final prediction for $D(I)$. However, when we examine temperature the sensitivity is quite stunning,

$$\text{Temp.} = 295.95 \text{ K} + 2 \text{ K} = 297.95 \text{ K}, \quad D(I) = -18.1$$

$$\text{Temp.} = 295.95 \text{ K} - 2 \text{ K} = 293.95 \text{ K}, \quad D(I) = -8.5$$

Given that the highest values of $D(I)$ for the exponentially shaped object occur when both humidity and temperature are at their highest possible values, as allowed by their error limits, it follows that the worst case *maximum* for the prediction of $D(I)$ occurs when Humidity = 51% and Temperature = 297.95 K (the impact of pressure being negligible in this case). In this instance, $D(I) = -18.2$. Likewise, the worst case *minimum* occurs when both of these environmental variables are at their lower limits, ie. Humidity = 49% and Temperature = 293.95 K, for which $D(I) = -8.5$.

This process was repeated for all objects and the comparison between the predicted values for $D(I)$ and the measured/calculated values has been replotted in Fig. 8.14 below, but this time with error bars inclusive.

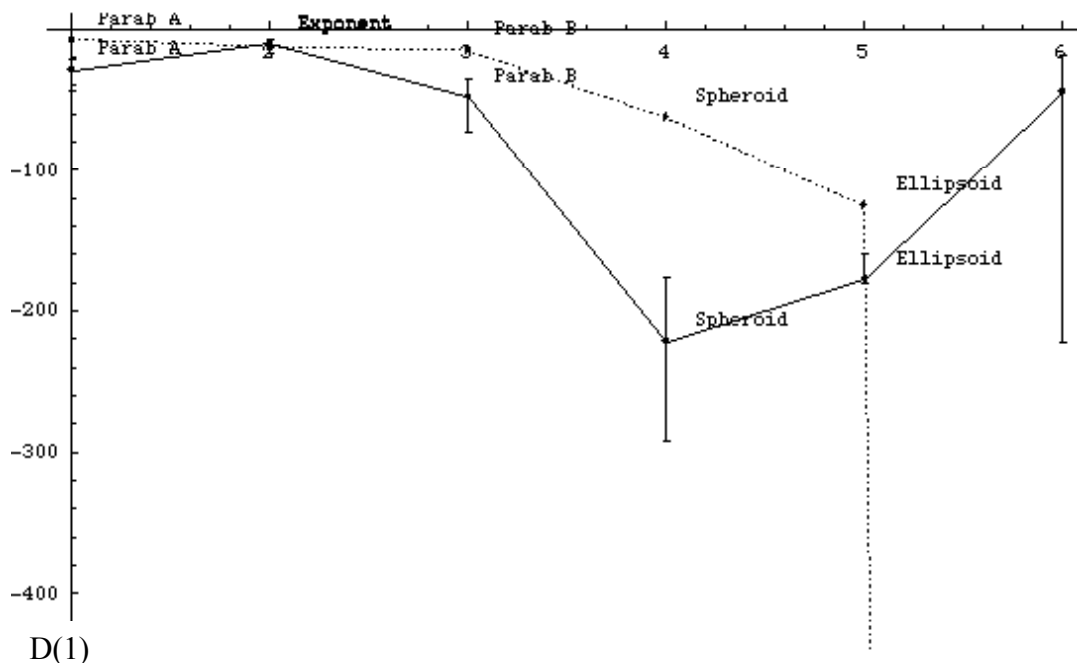


FIG. 8.14. Comparison of Calculated (broken line) with Predicted (solid line) values for $D(1)$ with associated error bars.

The process was also repeated for the predictions of $D(2)$ and these results are plotted below,

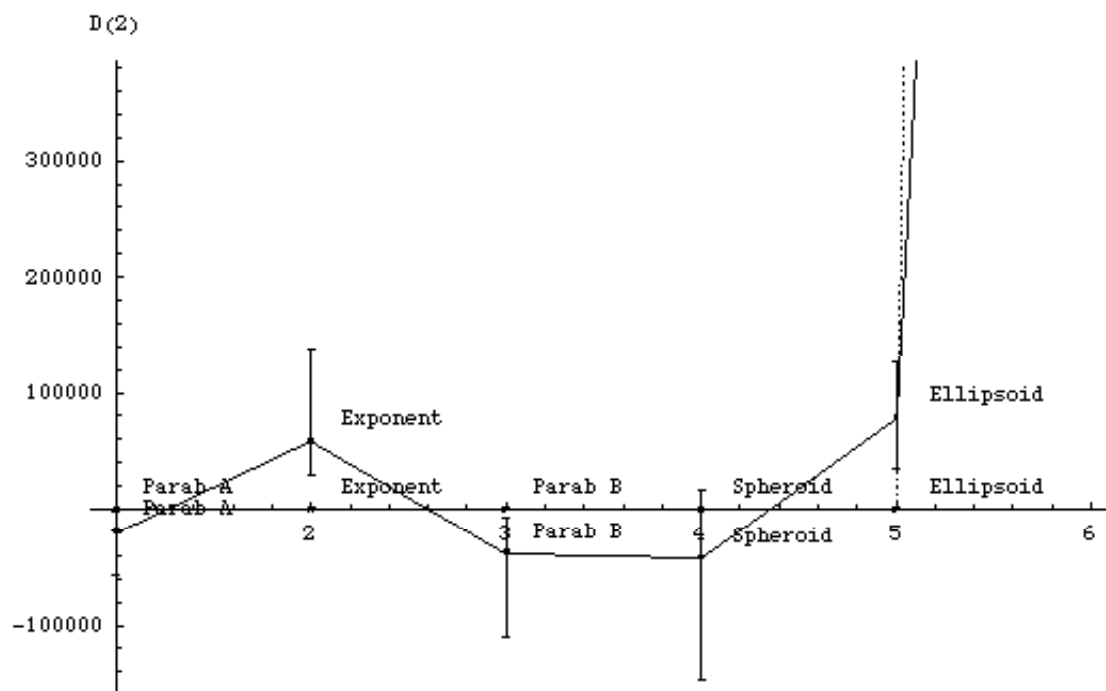


FIG. 8.15. Comparison of Calculated (broken line, which is too close to zero to be visible) with Predicted (solid line) values for $D(2)$ with associated error bars.

In both cases, it's clear that the error limits on the predicted values do *not* encompass all values for $D(1)$ and $D(2)$ calculated by direct measurement. Thus the discrepancy between theory and measurement can not be explained away as simple experimental error.

Further to the question of whether a small scaling or offset on one of the terms in the forward model could propagate through the inverse model to produce a greater correlation between experiment and theory, it's clear from our above analysis that the only term which has *any* real impact upon the inverse model's predictions is the temperature. So could applying an offset on the temperature in the forward model produce greater correlation? Unfortunately, the answer is no. It's possible to apply a several degree offset to the temperature to cause *one* data point to correlate, but the other data points would not correlate and in general the correlation becomes worse than before.

Thus, we concede that the lack of correlation between theory and measurement of the inverse model cannot be attributed to either (a) experimental error or (b) a *slight* flaw in the forward model. We have no doubt that there are flaws in the inverse model which hark back to those in the forward model that made it difficult for us to obtain reasonable predictions for the echoes from cones, namely the failure of the model to account for creeping waves. However, without a detailed analysis of the theory of creeping waves and its integration into Freedman's model, which is beyond the scope of this thesis, this impact of this missing element of the model remains conjecture.

However, we believe that the primary flaw in the model is the impact of the ill-conditioned matrix (coupled with insufficient data accuracy) upon our predictions of $D(1)$. Is this problem resolvable? The stability of the matrix can only be increased if we reduce the condition number by at least an order of magnitude and the only way to do

this would be to reduce the wave number by a similar degree. Transferring the model to a medium like water, for which the speed of sound is more than four times that in air, as well as lowering the frequency of the pulses down to the acoustic range would be enough to reduce the condition number by an order of magnitude. A medium such as steel (for non-destructive testing) with a speed of sound about 17 times that in air, would reduce the condition number by an even greater degree. However, the model would have to be further modified to compensate for the various idiosyncrasies of these mediums and in any event, such medium changes would defeat the purpose of our research, which was to construct the model as an aid for autonomous mobile robotic sensing.

If we choose to restrict the model for use in an air environment only, the condition number cannot be altered to any appreciable degree. Consequently, the only way to counteract the impact of the ill-conditioned matrix would be to use data of exceptional accuracy. Given that our data, with its three significant figures of accuracy, is insufficient for the task, the question posed is then, how accurate would our data have to be in order for the model to be workable? Ideally, we would like our predictions of $D(I)$ to be accurate to within 1%, implying an accuracy of three significant figures. Given that the large condition number will cause the loss of two significant figures from our prediction of $D(I)$ irrespective of how accurate our data is, we would need to ensure that our data is accurate to at least *five* significant figures to result in a final prediction for $D(I)$ accurate to three figures. An accuracy of five significant figures can only be achieved if we can ensure errors in our data of *under* 1/10000.

To do this we would have to increase the accuracy of our estimate of the population mean of the amplitude (see section 4.1 (a)) using a higher sample size to

reduce the standard deviation of the distribution of sample means to within 1/10000. The equation governing this is given below²¹,

$$\sigma_{\bar{x}} = \frac{\sigma}{\sqrt{n}} \quad (8.15)$$

where $\sigma_{\bar{x}}$ = standard deviation of the distribution of sample means

σ = standard deviation of the population (ie. the distribution of measured echo amplitudes)

n = sample size (ie. how many echoes are averaged to obtain the estimate)

In practice, to reduce the standard deviation of the distribution of sample means to 1/10000 would still not be enough, since this would ensure that our estimate of the population mean of the amplitude was accurate to within 1/10000 in *only* 68% of cases. We would actually need to reduce the standard deviation to 1/20000 before we could safely state that the amplitude estimate is accurate to within 1/10000 in 95% of cases (ie. two standard deviations), which is acceptable.

Using Eq. (8.15) above with the standard deviation of the population of 3%, as determined in section 4.1 (a), and a standard deviation of the distribution of sample means set to our target of 1/20000, we calculate that the required sample size is 36000. Thus, we would need to average over almost 36000 echo samples before we could obtain the necessary accuracy to satisfy the matrix stability requirements of the inverse model. Given that 50 samples take approximately 30 seconds, 36000 samples would take six hours. Clearly this would not be practical. If we lowered the accuracy standard of our model, so that we would be satisfied with an inverse model able to make

predictions for $D(I)$ accurate to only 10% (two significant figures), we would still need to average over 3600 echo samples, which would take 36 minutes. We need to point out again that because the condition number is only a *rough* estimate of the loss of precision, our calculation of the number of required samples is at best only a ball park figure.

In practice, to sample the echoes for this length of time, whether it's 36 minutes, or even just 15 minutes, is not feasible for a couple of reasons. Firstly, as discussed earlier, the Mylar film within the transducer loses its tension if the bias is applied for too long a period. We have measured this effect over several hours (see Fig. 4.5) but it begins to manifest itself within just a few minutes of continuous use. This problem is currently solved by using the transducer for no more than a minute at a time and then removing the bias for about 60 seconds. To use the transducer for 36 minutes continuously (let alone six hours) would inevitably cause the generated echo to reduce in amplitude over the course of the sampling period, as the tension in the film reduces, which would produce a skewed result in the mean. Another reason this is not practical is because environmental changes in temperature, pressure and humidity over the course of several minutes are non-negligible. Their impact on both time of flight, via their effect on the speed of sound, as well as the absorption coefficient would skew the mean also. It could be argued that the drift in the absorption coefficient could be accounted for by modelling it with the standard method for the calculation of the absorption of sound⁷. However, even with accurate measurements of the environmental conditions, the calculated value would only be accurate to within 10%.

These problems are not insurmountable though. It's possible that under more rigorous laboratory conditions, with far stricter environmental controls, as well as a different make or model of transducer, samples could be averaged for a full 36 minutes

without any drift in the mean. Also, if one is willing to transfer the model to either water, for sonar sensing, or steel, for non-destructive testing, where the condition number doesn't place such high demands on the required accuracy of the data, there may be an application for this model. However, such prospects will have to be left to future workers.

8.3 Practical Application of the Inverse Model

In it's current state, the inverse model is not without possible application though. Making allowances for the fact that the predictions of $D(I)$ are accurate to, at most, only one significant figure, Fig. 8.5 indicates a general, albeit rather broad, qualitative correlation between theory and measurement (in most instances). So, let's see if this can be applied.

Let us put forth the hypothetical example of a factory that manufactures light bulbs. An obvious requirement of such a manufacturing process would be quality control. Specifically, the inspection and elimination of those bulbs that were damaged during production. The flaws may not be as obvious as a bulb that imploded due to a crack in the vacuum seal, but may be more subtle, such as a bulb that is slightly irregular in shape or has a bulge in it's surface. Whilst visual inspection *may* identify these flawed bulbs, the process would benefit from a faster more reliable inspection system, one which the inverse model may provide.

We took three standard 100W clear bayonet cap light bulbs as our test items. These were 10.4cm long with a maximum width of 6.2cm at the equator of the globe. In their untouched condition, they represented the standard shape(s) that would pass the quality control process. In other words, they are all identical upon visual inspection and

any minor faults they may have are within the specified parameters of the quality control process. We measured the echoes from these three bulbs in exactly the same manner as we tested the inverse model with the various geometric scattering bodies. Thus they were all located at a 40cm range, 40kHz and 60kHz waves were used, 100 samples were taken, etc... We then repeated the process, but this time we attached small mounds of Blu-Tak™ onto the glass bulbs. These mounds had a height no greater than approximately 1mm and were spread out over a 1cm area, the height tapering near the circumference of the mound. An example of one of these is shown in Fig. 8.16 below,

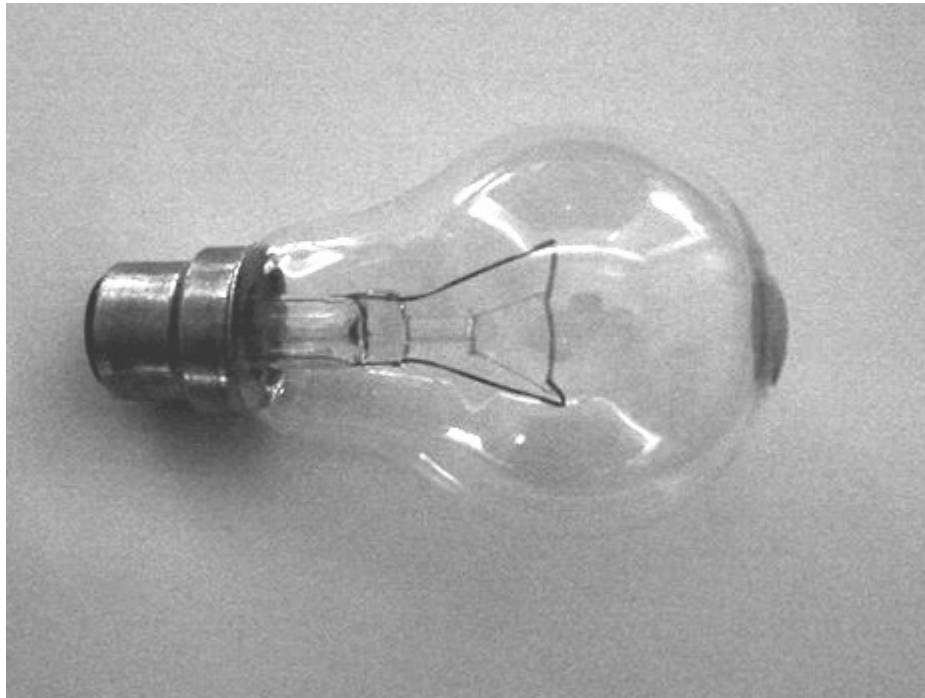


FIG. 8.16. 100W Clear Bayonet Cap Light Bulb with a 1cm square area mound of Blu-Tak™ attached to the glass.

The purpose of adding this mound of Blu-Tak™ is of course to simulate a defect in the shape of the bulb. The mound may look larger than 1mm in height from the photo above, but that is illusory due to us seeing the aft edge of the mound through the glass.

The measurement cycle was repeated once more with these modified bulbs. The echoes obtained were run through the inverse model in the same manner as previously. The *only* difference was that in this case there was no need to calibrate the model by determining values for $K(f)$. This was because in this instance we are only interested in the *relative* values of $D(l)$, not absolutes, as the relative values are all that are needed to differentiate between perfect bulbs and “faulty” ones. The results of these calculations are tabulated in Table A.4.10 in Appendix A.4 and plotted in Fig. 8.17 below,

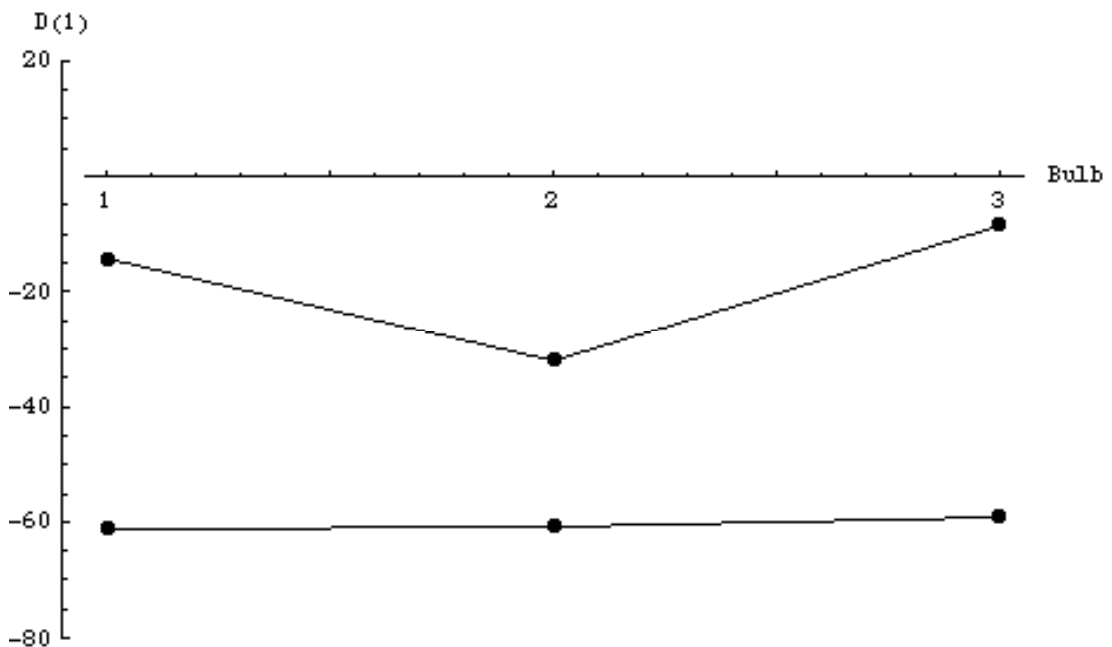


FIG. 8.17. Comparison of the predicted relative values of $D(l)$ for both the modified bulbs (top) and the untouched bulbs (bottom).

The results are quite distinct. Whilst the unmodified (good) bulbs all hover very close to a relative magnitude of -60, the modified (bad) bulbs deviate markedly from these. In a real world environment, numerous measurements would be made upon the bulbs that pass visual inspections and from these a standard deviation for the top curve would be determined. Faulty bulbs would then be defined as any that fall outside this error limit.

Given that it would have been possible to distinguish between the normal and defective bulbs just as easily with amplitude alone as with the predictions for $D(I)$, why would we apply the inverse model to this task at all? In *this* particular instance it's true that we could have distinguished the defective bulbs from the normal ones using amplitude alone. However, there is nothing to indicate that this should be the case for all objects tested in this manner. Moreover, amplitude alone offers only a blind discrimination between the objects and does not provide any information as to *why* the objects are distinguishable. The inverse model, in calibrated form, at least provides an estimate, by virtue of $D(I)$, of the physical structure of the object being insonified. As $D(I)$ is a function of the front face of the scatter, it will vary in amplitude if the front face is varied to any degree, allowing discrimination of different bodies or possibly detecting defects. Of course, whether this information is of use to the parties performing the tests depends on the nature of their investigation.

From the results given above, it would appear that the inverse model seems capable of detecting physical anomalies on smoothly varying objects, at least in this example, and as such it offers the *possibility* of application to industry, specifically in the area of quality control where, in many industries, this involves distinguishing between those items that are physically damaged from those that are not. However, we need to be aware that given the instability of the inverse model, the results presented cannot be interpreted as proof of a practical applicability of the model, but rather a one-off case that apparently works but for which we cannot provide a solid basis to generalise to other cases.

9 Conclusion

9.1 Contributions of this thesis

We summarised the limitations of current acoustic sensing technologies and postulated that in order to make further progress in this area, we would need to develop a more sophisticated model of the wave mechanics of acoustic backscatter. We took Freedman's forward model as our basis, provided an abridged derivation of this model that highlighted its inherent basic assumptions and gave a physical interpretation of the model's mechanisms, with examples. We then made extensions to the model in order to expand its applicability to air environments and to systems with non-ideal transducer/receiver configurations. Before putting the extended model to the test, we made extensive progress in minimising the noise inherent to our proposed experimental apparatus. We also developed methodologies for both minimising external noise sources and data analysis.

We then tested this extended model with a variety of distinct acoustic scatterers, including spheres, cones and truncated cones at ranges of 80cm, 100cm and 140cm and found that the model's greatest correlation between experiment and theory occurred when dealing with spheres. We postulated that the model's inability to account for creeping waves was the major cause for its lack of capacity to deal with objects that were not smoothly shaped. However, with an average error of less than 5% for spheres, we determined that the model should be reasonably accurate at calculating the echoes from convex objects with smoothly varying surfaces, spheres being but one example.

We then examined the possibility of inverting the extended forward model and theorised two possible alternatives for inversion. The first was a model that was

independent of time t . Despite some advantages, we ultimately rejected it on practical grounds and adopted the second alternative, a time dependent model. We fully developed this model and devised the analysis methodology that would be applied to test it. We also provided an algorithm for reconstructing the shape of the scatterer using the predictions of the inverse model. Following this, we analysed the geometric properties of six finely turned geometric objects that would be our test subjects for verifying the inverse model. We examined the range variance, area variance, physical parameters and various orders of the surface curvature in each case and the locations and magnitudes of surface discontinuities on the scatterers were determined for each.

We then tested the inverse model with these six scatterers at a range of 40cm using 40kHz and 60kHz chirps. Using two different approaches to analysing the data, we found that the model had little quantitative correlation between the predicted discontinuities and their measured values. We analysed the inverse model, found the primary source of the errors to be the coupling of an ill conditioned matrix with data of insufficient accuracy and determined the conditions under which the model should generate accurate results. We concluded that the inverse model could not be verified quantitatively with our data, but that future workers may be able to do so under more rigorous laboratory conditions or a switch to a different medium.

Despite the quantitative limitations of the inverse model, we tested whether it's general qualitative agreement between measurement and theory could be put to practical use. We conducted an experiment to simulate the type of flaws that one may expect to see in manufactured items emerging from a conveyor belt on a production line, in this case glass light bulbs. In all cases, we were able to use the model to clearly distinguish between the faulty and non-faulty bulbs.

In summary, the following are the contributions of this thesis:

- Extended Freedman's model to expand its applicability to air environments and to systems with non-ideal transducer/receiver configurations and verified it via experimental testing.
- Developed the theory for an inverse model of ultrasonic echolocation based on the extended forward model as well as an algorithm for visualising the scattering target using its predictions and tested the model experimentally.
- Experimentally verified that the inverse model could successfully discriminate between simulated small defects in industrially produced items.

9.2 Future Directions

The automation of an increasing number of processes in industrial environments has many advantages. Firstly there is the cost factor. After the initial purchase of the system, the only costs are maintenance and, on occasion, the cost involved in reprogramming the system, should the need arise. There is also the issue of speed. Almost without exception, automated systems conduct their operation at either the same speed or faster than a human operator. Accuracy is another benefit, since human fallibility will almost always result in a small, but constant percentage of mistakes on the part of the operator during any given period. Finally, safety is another benefit of automation. In many cases, industrial environments can be hazardous work environments and on both ethical and financial grounds, it would be more desirable for a machine to undertake the associated risks rather than a person.

Industrial inspection and quality control is one example of such a process that is currently dominated by human operators but would benefit from automation. The

inverse model developed in this research should be of interest to those working in the field of industrial quality control, specifically those involved in the deployment of inspection technologies because of its potential to lead to the development of real-time quality testing systems for production lines that could perform with a higher degree of accuracy and speed than the visual inspection procedures currently being employed. With the added benefit of being a relatively low cost solution, and the reduction in industrial accidents that may occur were such a system to be implemented, we feel that implementing the inverse model would be a step forward for industrial sensing.

Finally, this research has raised the possibility for further research into four areas. Firstly, even though the development of the inverse model is mathematically sound, it is based on a forward model that is, to an extent, flawed. Further research into the extended forward model from a more theoretical approach could help shed some light onto what could be done to improve the model, the inclusion of creeping wave theory into the model being a starting point. Secondly, the limitations imposed upon the accuracy of the model in air, by virtue of the ill conditioned matrix, could be circumvented by modifying the model to work in a different medium, water for sonar-sensing or steel for non-destructive testing. Thirdly, laboratory environments with exceptional control of environmental conditions could be employed to test the model's validity in air. Lastly, experiments on the inverse model indicate that it may well be robust enough, even in its current state, to be applied to the task of industrial sensing, as outlined above. Further research into this area could include the development and implementation of an industrial sensing system that is able to separate defective items on a conveyor belt from those that are undamaged.

A Appendix

A.1 Bibliography

¹ K. Komoriya, S. Tachi and K. Tanie, “A Method of Autonomous Locomotion for Mobile Robots”, *Advanced Robotics*, **1** (1), pp. 3 – 19 (1986).

² P. J. McKerrow, *Introduction to Robotics*, (Addison-Wesley, 1991), p. 589.

³ L. Kleeman and R. Kuc, “Mobile robot sonar for target localization and classification”, *International Journal of Robotics Research*, **14** (4), pp. 295 – 318 (1995).

⁴ P. J. McKerrow, “Echolocation – From range to outline segments,” *Robotics and Autonomous Systems*, **11** (4), (Elsevier, 1993), pp. 205-211.

⁵ A. Lhemery, “Impulse-response method to predict echo-responses from targets of complex geometry. Part 1: Theory,” *J. Acoust. Soc. Am.*, **90** (5), pp. 2799-2807 (1991).

⁶ J. J. do Rego Silva, *Acoustic and Elastic Wave Scattering using Boundary Elements*, (Computational Mechanics Publications, 1994), p. 9 – 24, 49 – 67, 87 – 123

⁷ A. Freedman, *The formation of acoustic echoes in fluids*. (Doctoral Thesis, University of London, 1961), pp. 5-8, 34-58, 95-108.

⁸ L. L. Beranek, *Acoustics*, (McGraw-Hill, 1954), p. 100.

⁹ S. Kocis and Z. Figura, *Ultrasonic Measurements and Technologies*, (Chapman & Hall, 1996), p. 11.

¹⁰ *American National Standard: Method for the calculation of the absorption of sound by the atmosphere* (American Institute of Physics, New York, 1978).

¹¹ A. Langen of Fraunhofer-Institut in a verbal communication with P. J. McKerrow of the University of Wollongong, August 1989.

¹² E. Skudrzyk, *The Foundations of Acoustics*, (Springer-Verlag, 1972), pp. 603 & 631.

- ¹³ *Condenser Microphones and Microphone Preamplifiers for Acoustic Measurements*, (Bruel and Kjaer, 1982), p. 62.
- ¹⁴ B. D. Stanley, *A Comparison of binaural ultrasonic sensing systems*, (Doctoral Thesis, School of Information Technology and Computer Science, University of Wollongong, 2003), p. 80.
- ¹⁵ A. V. Oppenheim and R. W. Schaffer, *Discrete-time signal processing*, (Prentice Hall, 1989), p. 87.
- ¹⁶ A. J. Rudgers, "Separation and analysis of the acoustic field scattered by a rigid sphere," *J. Acoust. Soc. Am.* **52**, 234-246 (1972).
- ¹⁷ P. J. McKerrow, S. Zhu and S. New, "Simulating Ultrasonic Sensing with the Lattice Gas Model," *IEEE Transactions On Robotics And Automation.* **17** (2), pp. 202-208 (April 2001).
- ¹⁸ P. J. McKerrow, D. Crook and J. Tsakiris, "Modelling Ultrasonic Sensing for Mobile Robots," in *Proceedings of the Sixth International Symposium on Robotics and Manufacturing* (1997), pp. 497-502.
- ¹⁹ K. Sasaki, et. al., "Classification of Objects' Surface by Acoustic Transfer Function," in *Proceedings of the 1992 IEEE/RSJ Int. Conf. on Intelligent Robots and Systems* (1992), pp. 821-828.
- ²⁰ R. J. Wyber, *The recognition of targets from their echo signals*, (Doctoral Thesis, Department of Electrical Engineering, University of Sydney, 1973).
- ²¹ J. A. Twaite and J. A. Monroe, *Introductory Statistics*, (Scott, Foresman and Company, 1979). P. 288.

A.2 Glossary of Terms

λ = Wavelength of the transmitted wave

$$\theta = \omega t - 2kr$$

ϕ = Angle of incidence of the incoming radiation

α = Atmospheric absorption coefficient

$A(f)$ = Frequency-dependent sensitivity of the transducer and receiver

$A(x)$ = Cross-sectional area of the scatterer at range x

$\beta_H(\phi)$ = Directivity of the receiver

$\beta_P(\phi)$ = Directivity of the transducer

c = Speed of sound in air

$D(A_w, r_g, n)$ = n th order discontinuity at range r_g

$D(n)$ = n th order discontinuity (*shorthand version of $D(A_w, r_g, n)$*)

E = Voltage at the receiver

G = Gain applied to the received signal

H = Voltage produced per unit pressure at unit distance in direction $\theta = \phi = 0$

J_1 = Bessel function of the first order

k = Wave number of the transmitted wave

P = Pressure produced per unit volt at unit distance in direction $\theta = \phi = 0$

r_g = Range to the source of the echo

r_{g-} = Range infinitesimally prior to the discontinuity

r_{g+} = Range infinitesimally beyond the discontinuity

$r(x)$ = Radius of the cross-sectional area of the object at range x

t = Instant of echo reception

t_i = Instant of incidence upon the target

V = Voltage applied to the transducer

ω = Angular frequency of the wave

$W_w(r)$ = *Directivity-weighted* solid angle subtended at the receiver by all parts of
the scattering body within the range r

A.3 Derivation of Equation 6.3

The following is the derivation of the maximum value equation (Eq. 6.3) used in Chapter 6 in the development of the time independent variant of the inverse model. Eq. (6.3) is shown below,

$$\left| D(0)\sin\theta - \frac{D(1)}{2k}\cos\theta - \frac{D(2)}{4k^2}\sin\theta \right|_{MAX} = \left(D(0)^2 + \frac{D(1)^2}{4k^2} - \frac{D(0)D(2)}{2k^2} + \frac{D(2)^2}{16k^4} \right)^{1/2} \quad (6.3)$$

$$\text{Firstly, let } X = \sqrt{A^2 + B^2} \quad \text{where } A, B \in \Re \quad (A.1)$$

$$\text{and } \gamma = \tan^{-1}\left(\frac{B}{A}\right) \quad (A.2)$$

$$\text{The square of Eq. (A.1), } X^2 = A^2 + B^2 \quad (A.3)$$

$$\begin{aligned} \text{Eq. (A.2) rearranged, } B &= A \tan \gamma \\ &= A \frac{\sin \gamma}{\cos \gamma} \end{aligned} \quad (A.4)$$

Substituting Eq. (A.4) into (A.3),

$$\begin{aligned} X^2 &= A^2 + A^2 \frac{\sin^2 \gamma}{\cos^2 \gamma} \\ X^2 \cos^2 \gamma &= A^2 (\cos^2 \gamma + \sin^2 \gamma) \\ &= A^2 \end{aligned}$$

$$\text{Therefore, } A^2 = X^2 \cos^2 \gamma \quad (A.5)$$

$$\text{and, } A = \pm X \cos \gamma \quad (A.6)$$

Substituting Eq. (A.5) into (A.3),

$$X^2 = X^2 \cos^2 \gamma + B^2$$

$$X^2(1 - \cos^2 \gamma) = B^2$$

$$X^2(\sin^2 \gamma) = B^2$$

$$\text{Therefore,} \quad B^2 = X^2 \sin^2 \gamma \quad (\text{A.7})$$

$$B = \pm X \sin \gamma \quad (\text{A.8})$$

Because of the \pm term in Eq. (A.6) and (A.8), there are four possibilities for the maximum value of $|A \cos \theta + B \sin \theta|_{MAX}$. These are,

$$\begin{aligned} (1) \quad |A \cos \theta + B \sin \theta|_{MAX} &= |X \cos \gamma \cos \theta + X \sin \gamma \sin \theta|_{MAX} \\ &= |X \cos(\gamma - \theta)|_{MAX} \\ &= X |\cos(\gamma - \theta)|_{MAX} && \text{since } X \geq 0 \quad \forall A, B \\ &= X && \text{since } |\cos(\gamma - \theta)|_{MAX} = 1 \\ &= \sqrt{A^2 + B^2} \end{aligned}$$

Similarly for the others,

$$\begin{aligned} (2) \quad |A \cos \theta + B \sin \theta|_{MAX} &= |-X \cos \gamma \cos \theta + X \sin \gamma \sin \theta|_{MAX} \\ &= |-X \cos(\gamma + \theta)|_{MAX} \\ &= X |-\cos(\gamma + \theta)|_{MAX} \\ &= X \\ &= \sqrt{A^2 + B^2} \end{aligned}$$

$$\begin{aligned} (3) \quad |A \cos \theta + B \sin \theta|_{MAX} &= |X \cos \gamma \cos \theta - X \sin \gamma \sin \theta|_{MAX} \\ &= |X \cos(\gamma + \theta)|_{MAX} \\ &= X |\cos(\gamma + \theta)|_{MAX} \\ &= X \\ &= \sqrt{A^2 + B^2} \end{aligned}$$

$$\begin{aligned}
(4) \quad |A \cos \theta + B \sin \theta|_{MAX} &= |-X \cos \gamma \cos \theta - X \sin \gamma \sin \theta|_{MAX} \\
&= |-X \cos(\gamma - \theta)|_{MAX} \\
&= X |- \cos(\gamma - \theta)|_{MAX} \\
&= X \\
&= \sqrt{A^2 + B^2}
\end{aligned}$$

Thus, in all cases,

$$|A \cos \theta + B \sin \theta|_{MAX} = \sqrt{A^2 + B^2} \quad (\text{A.9})$$

Now, let $A = -\frac{D(1)}{2k}$ and $B = D(0) - \frac{D(2)}{4k^2}$ and substitute these into Eq. (A.9),

$$\begin{aligned}
\text{Thus,} \quad \left| \left(-\frac{D(1)}{2k} \right) \cos \theta + \left(D(0) - \frac{D(2)}{4k^2} \right) \sin \theta \right|_{MAX} &= \sqrt{\left(-\frac{D(1)}{2k} \right)^2 + \left(D(0) - \frac{D(2)}{4k^2} \right)^2} \\
&= \left(D(0)^2 + \frac{D(1)^2}{4k^2} - \frac{D(0).D(2)}{2k^2} + \frac{D(2)^2}{16k^4} \right)^{1/2}
\end{aligned}$$

Therefore,

$$\left| D(0) \sin \theta - \frac{D(1)}{2k} \cos \theta - \frac{D(2)}{4k^2} \sin \theta \right|_{MAX} = \left(D(0)^2 + \frac{D(1)^2}{4k^2} - \frac{D(0).D(2)}{2k^2} + \frac{D(2)^2}{16k^4} \right)^{1/2}$$

Q.E.D.

A.4 Data for Selected Figures.

Diameter (m)	Range (m)	Measured (V)	Predicted (V)	Pred./Meas.
0.100	0.800	1.95E-01	1.91E-01	0.98
	1.000	9.96E-02	1.13E-01	1.13
	1.400	4.90E-02	4.90E-02	1.00
0.150	0.800	2.89E-01	2.88E-01	1.00
	1.000	1.75E-01	1.70E-01	0.97
	1.400	7.10E-02	7.39E-02	1.04
0.200	0.800	4.14E-01	3.89E-01	0.94
	1.000	2.02E-01	2.29E-01	1.13
	1.400	9.98E-02	9.88E-02	0.99

Table A.4.1. Data for Fig. 5.1.

Diameter (m)	Range (m)	Measured (V)	Predicted (V)	Pred./Meas.
0.100	0.800	9.49E-03	1.04E-02	1.10
	1.000	5.70E-03	6.07E-03	1.06
	1.400	2.60E-03	2.60E-03	1.00
0.150	0.800	1.61E-02	1.57E-02	0.98
	1.000	9.14E-03	9.23E-03	1.01
	1.400	3.71E-03	3.94E-03	1.06
0.200	0.800	2.15E-02	2.10E-02	0.98
	1.000	1.27E-02	1.23E-02	0.97
	1.400	5.24E-03	5.24E-03	1.00

Table A.4.2. Data for Fig. 5.2.

Base Diam. (m)	Range (m)	Measured (V)	Predicted (V)	Pred./Meas.
0.100	0.800	4.69E-02	4.69E-02	1.00
	1.000	2.37E-02	2.90E-02	1.22
	1.400	1.77E-02	1.30E-02	0.74
0.150	0.800	9.34E-02	1.13E-01	1.21
	1.000	2.05E-02	7.55E-02	3.69
	1.400	1.48E-02	3.61E-02	2.43
0.197	0.800	1.41E-01	2.20E-01	1.56
	1.000	1.04E-01	1.64E-01	1.58
	1.400	3.10E-02	8.59E-02	2.77

Table A.4.3. Data for Fig. 5.3.

Base Diam. (m)	Range (m)	Measured (V)	Predicted (V)	Pred./Meas.
0.100	0.800	1.28E+00	9.08E-01	0.71
	1.000	8.42E-01	6.08E-01	0.72
	1.400	2.91E-01	2.91E-01	1.00
0.150	0.800	1.19E+00	1.62E+00	1.37
	1.000	8.20E-01	1.31E+00	1.60
	1.400	4.02E-01	7.29E-01	1.81
0.197	0.800	4.89E-01	2.11E+00	4.32
	1.000	4.19E-01	2.25E+00	5.36
	1.400	2.93E-01	1.54E+00	5.25

Table A.4.4. Data for Fig. 5.4.

Trunc. Diam. (m)	Range (m)	Measured (V)	Predicted (V)	Pred./Meas.
0.052	0.800	7.73E-01	6.85E-01	0.89
	1.000	3.81E-01	4.02E-01	1.06
	1.400	1.74E-01	1.74E-01	1.00
0.097	0.800	1.27E+00	2.47E+00	1.94
	1.000	8.10E-01	1.47E+00	1.81
	1.400	2.64E-01	6.38E-01	2.41
0.149	0.800	3.45E+00	5.75E+00	1.66
	1.000	3.36E+00	3.41E+00	1.02
	1.400	1.98E+00	1.49E+00	0.75

Table A.4.5. Data for Fig. 5.5.

Trunc. Diam. (m)	Range (m)	Measured (V)	Predicted (V)	Pred./Meas.
0.052	0.800	7.82E-02	7.62E-02	0.98
	1.000	4.32E-02	4.47E-02	1.04
	1.400	1.92E-02	1.92E-02	1.00
0.097	0.800	1.48E-01	2.70E-01	1.82
	1.000	1.02E-01	1.58E-01	1.55
	1.400	4.80E-02	6.78E-02	1.41
0.149	0.800	2.91E-01	6.24E-01	2.14
	1.000	2.20E-01	3.67E-01	1.67
	1.400	5.78E-02	1.57E-01	2.71

Table A.4.6. Data for Fig. 5.6.

Object	Measured $D(1)$	Predicted $D(1)$
Paraboloid A	-2.4π	37.4
Exponential	-4π	40.7
Paraboloid B	-4.9π	66.5
Spheroid-Paraboloid	-20π	188
Ellipsoid	-40π	86.0
4 th Order	$-\infty$	1900

Table A.4.7. Data for Fig. 8.3.

Object	Measured $D(2)$	Predicted $D(2)$
Paraboloid A	0	-1.94 E+04
Exponential	4π	5.85 E+04
Paraboloid B	0	-3.82 E+04
Spheroid-Paraboloid	2π	-4.24 E+04
Ellipsoid	8π	7.84 E+04
4 th Order	$+\infty$	7.25 E+07

Table A.4.8. Data for Fig. 8.6.

Object	Measured $D(1)$	Predicted $D(1)$
Paraboloid A	-2.4π	-29.9
Exponential	-4π	-11.0
Paraboloid B	-4.9π	-49.2
Spheroid-Paraboloid	-20π	-228
Ellipsoid	-40π	-183
4 th Order	$-\infty$	-54.3

Table A.4.9. Data for Fig. 8.13.

Bulb	Predicted $D(1)$
1A (Modified)	-14.4
1B (Unmodified)	-61.1
2A (Modified)	-32.0
2B (Unmodified)	-60.9
3A (Modified)	-8.5
3B (Unmodified)	-59.2

Table A.4.10. Data for Fig. 8.17.

**Please see print copy for Appendices A.5a, A.5b
and A.5c**

Please see print copy for Appendix A.6